UNIVERSITY OF CALIFORNIA,
IRVINE

Multi-Wavelength High Order Harmonic Generation from Intense Laser Plasma Interactions

DISSERTATION

submitted in partial satisfaction of the requirements
for the degree of

DOCTOR OF PHILOSOPHY

in Physics

by

Hunter Allison

Dissertation Committee:
Professor Franklin Dollar, Chair
Professor Roger McWilliams
Professor Chris Barty

2023

DEDICATION

This work is dedicated to my grandparents, Marilyn and Walter Dietiker. You watered the trampled and withered plant. You stood for me even when I could not stand for myself and showed me everything that I could be. In you, I see the very essence of love and the heart of the divine itself. If the work published in this thesis and any future work is worthy of any esteem or honor, let your names be elevated above my own. It is my promise to you to strive every day for a beautiful future tomorrow for all people. May Schrodinger's cat be found alive and that heartless dragon toppled[1]. May it be that the songs and melodies of my life only echo your excellence.

Your daughter in spirit for better or for worse in whatever comes next,

Allison Dietiker

TABLE OF CONTENTS

List of Acronyms vi

List of Figures ix

ACKNOWLEDGEMENTS xxi

VITA xxii

ABSTRACT OF THE DISSERTATION xxvi

Chapter 1 Introduction 1

1.1 Optical Metrology 1

1.2 Early History of Optics 5

1.3 Modern Application of Optics 8

1.4 Statement of Purpose 22

Chapter 2 Background and Theory 24

2.1 Maxwell's Equations 24

2.2 Plasmas 40

2.3 High harmonic generation 41

2.4 Phase-matching 45

2.5 MIR Gas-HHG 53

2.6 Ionization 55

2.7 Temporal Characteristics 58

Chapter 3 Methods 65

3.1 Lasers 65
3.2 Target 70
3.3 EUV Spectroscopy 73
Chapter 4 High Harmonic Generation from 3d-printed Laser-Gas Targets 86
4.1 Introduction 86
4.2 Methods 89
4.3 Results 93
4.4 Discussion 96
4.5 Conclusion 106
Chapter 5 Mid-Infrared Gas HHG Driven with Laguerre-Gaussian mode and Vector Polarization 108
5.1 Introduction 108
5.2 Methods 111
5.3 Results 115
5.4 Discussion 120
5.5 Conclusion 123
Chapter 6 400nm Solid Harmonic Generation from High-Contrast Drivers 125
6.1 Intro 125
6.2 Methods 130
6.3 Results 131
6.4 Discussion 134

6.5 Conclusion 140

Chapter 7 Conclusion 142

Bibliography 146

List of Acronyms

IR → infrared

MIR → midinfrared

UV → ultraviolet

EUV → extreme ultraviolet

SXR → soft x-rays, light with wavelength in the region of 20nm to 2nm.

Gas HHG → Gas Harmonic Generation. This refers to an intense laser-gas interaction which produces coherent attosecond radiation.

Solid HHG → Solid Harmonic Generation

ROM → Relativistic oscillation mirror, this is a model of relativistic solid harmonic generation.

CWE → Coherent Wake emission, this is a model of *non*relativistic solid harmonic generation

Ti: Saphire, Ti: Saph → Titanium doped sapphire; This refers to a common gain media used in many now commercially available laser systems such as Solstice.

m → meter; base unit of length

mm → millimeter; unit of length, 10^{-3}m

μm→micrometer; unit of length, 10^{-6}m

nm → nanometer; unit of length, 10^{-9}m

pm→ picometer; unit of length, 10^{-12}m

$fm\rightarrow$ femtometer; unit of length, $10^{-15}\mathrm{m}$

$s\rightarrow$ second, base unit of time

$ms\rightarrow$ millisecond; unit of time, $10^{-3}\mathrm{s}$

$\mu s\rightarrow$microsecond; unit of time, $10^{-6}\mathrm{s}$

$ns\rightarrow$ nanosecond; unit of time, $10^{-9}\mathrm{s}$

$ps\rightarrow$ picosecond; unit of time, $10^{-12}\mathrm{s}$

$fs\rightarrow$ femtosecond; unit of time, $10^{-15}\mathrm{s}$

$J\rightarrow$ joule; base unit of energy.

$\mathrm{mJ}\rightarrow$ millijoule; unit of energy, $10^{-3}\mathrm{J}$

$\mu J\rightarrow$ microjoule; unit of energy, $10^{-6\mathrm{J}}$

$nJ\rightarrow$ nanojoule; unit of energy, $10^{-9\mathrm{J}}$

$pJ\rightarrow$ picojoule; unit of energy, $10^{-12}\mathrm{J}$

$eV\rightarrow$ electron volt; unit of energy, The energy gained by a single electron after moving through a one volt potential difference.

$Hz\rightarrow$ Hertz, standard unit of frequency

$kHz\rightarrow$ kilohertz, unit of frequency, $10^{-3}\mathrm{Hz}$

$\mathrm{PSI}\rightarrow$ pound per square inch, unit of pressure

$\mathrm{torr}\rightarrow$ torr, standard unit of pressure, corresponds to 1 millimeter of mercury

$\mathrm{atm}\rightarrow$ atmosphere, unit of pressure, corresponds to the standard pressure of air on the surface of the Earth

$\mathrm{CEP} \rightarrow$ Carrier envelope phase, this quantity is especially important in relation to few cycle beams. If the CEP of a few cycle beam is not stable, its intensity can vary wildly pulse-to-pulse.

$\mathrm{CE} \rightarrow$ Coulomb explosion, this can occur when the nuclear binding fields become repulsive due to an incident field.

$\mathrm{KER} \rightarrow$ Kinetic Energy Release, this is the energy which gets released during a coulomb explosion.

$\mathrm{PiC} \rightarrow$ Particle in a Cell, this is a type of program which maps many charged particles to a single grid point and treats them as a single "macroparticle".

$\mathrm{SNR} \rightarrow$ Signal to Noise Ratio

$FTL \rightarrow$ Fourier Transform Limit.

List of Figures

Figure 1 The light observed from the sun appears as a continuous band, but with some colors missing. These same discrete lines would appear when hydrogen gas was illuminated by white light. 10

Figure 2 A single proton-electron pair can be solved analytically. The energy levels are discrete resonances. Whereas, for many atoms, the energy levels densely overlap and are basically impossible to solve analytically. However, they can be measured experimentally! 12

Figure 3 Muybridge's photos of the galloping horse. The key images that won the wager are the ones on the top row. 16

Figure 4 Motions occur on a variety of timescales. To see something fast, the experimenter needs a detector faster than the event itself. In the long exposure shot, the things that do not move over the course of minutes like the buildings and parked cars are in crisp focus. The fast-moving objects, traffic and people, appear as shimmering light trails. In the short exposure shot, all objects appear in crisp focus, frozen in time. Light Trails in front of a theater, photo reference [51]. Resolved picture of the theater, phoro reference [52]. 17

Figure 5 Edgerton's iconic bullet splitting the apple image captured using strobe photography. Photo reference[53]. 18

Figure 6 This diagram summarizes the characteristic timescale of various physical processes. Femtosecond lasers have been successful at observing chemistry in-action. The current frontier is the attosecond regime. 19

Figure 7 Dipole Radiation profile. The shape and sharpness of the conelike radiation profile is dependent on the details of the shape and size of the sample Δs. The outgoing curved wavefront can be made flat with a lens or curved mirror with the correct focal length f. The light after the lens is a plane wave whose diameter is determined by the size and collection angle of the lens. The wavefronts of this plane wave will have a uniform polarization aligned with the induced dipole moment of the dipole radiator. 29
Figure 8 Three common polarization states. The left most is pure vertical polarization. The middle is pure horizontal polarization. The rightmost is elliptical polarization. NOT DEPICTED, left and right circular polarization. This is a special case of elliptical polarization in which $A = B$ and $\phi = \pm\pi/2$. 31
Figure 9 Illustrations of the concept of flux. LEFT depicts the simplest case of a uniform field through a flat rectangular area. MIDDLE is a more general situation of a curved surface and non-uniform field. Locally, for a very small area of space, the field is uniform and the surface is flat with area $\boldsymbol{dS}$. The total flux is built up from the integration of many tiny flux surfaces. RIGHT depicts a common experimental situation of a light beam incident on a detector. 34
Figure 10 The electrostatic potential felt by the electron in the presence (solid black line) and absence (dotted black line) of the laser potential (solid red line). The ground level energy of the electron is given by 15.8eV. This is the first ionization potential of argon. 42
Figure 11 A plot of returning electron trajectories. The color corresponds to the energy of the electron. Redder is lower energy. Bluer/Purple represents higher energy. 44

Figure 12 The Kinetic energy of the electron during recombination..... 45
Figure 13 A schematic of how phase-matching works... (TOP-LEFT) Resultant signal intensity from ten emitters with random phase. The signal does NOT scale with the number of emitters N. It instead tends toward zero. (BOTTOM-LEFT) Resultant signal intensity if each emitter has identical phase. The signal intensity grows like the number of emitters squared $N2$. (RIGHT-COLUMN) The signal intensity from emitters at different parts throughout the sample is depicted graphically..... 46
Figure 14 Different Phase-matching regimes. (LEFT-Plot) The solid blue depicts the situation of finite Δk. The dotted blue line depicts quasi phase-matched signal buildup. The solid black depicts phase-matched signal which approached an asymptote due to gas reabsorption. The dotted black line depicts theoretical phase-matching..... 47
Figure 15 Coherence length as a function of ionization fraction. At about 4.75% ionization, the coherence length approaches infinity..... 49
Figure 16 The blue line represents the beam radius. The dashed red line represents the geometric/Guoy phase that gets imparted as the beam goes through focus. Plot reference[57]..... 52
Figure 17 The blue-line represents an incoming gaussian pulse. The dark blue line represents the fraction of neutral atoms. It starts at one, but then this fraction begins to decrease as the pulse approaches. The red, purple, and gold lines represent the ionization fraction of various ion species. The black line represents the electron ionization fraction. For these parameters, the target gas is fully ionized well before the peak intensity arrives. This calculation only includes ion species up to Z=+3. 57

Figure 18 Intense electromagnetic plane wave incident on 800 argon which induces tunnel ionization. The LEFT-side represents the situation for a low intensity driver. The RIGHT-side is the situation for a high intensity driver. The top row shows the ionization rate as a function of time. The bottom row depicts the ionization buildup as a function of time. The horizontal blue line represents $\boldsymbol{\eta crit}$. This is the target ionization for phasematched 800nm argon..... 58
Figure 19 This graphic depicts attosecond pulse trains of different lengths on the left and their associated spectrums on the right. From the top row to the bottom row, the number of EUV bursts decreased. The bottommost row shows the situation for just one burst..... 59
Figure 20 The left-side of the figure simulates the qualitative appearance of "single-atom" and "phase-matched" spectra. Both spectra are normalized to a peak value of "1" in arbitrary intensity units. The right-side shows the FTL of each spectrum. ... 60
Figure 21 LEFT is an actual gas-harmonic spectrum measurement. RIGHT depicts this spectrum's FTL. The red-line represents intensity as a function of time. The black line represents the envelope of just one single EUV burst. 61
Figure 22 This figure relates the phase and energy of the electron to its time of recombination. It assumes an incident 800nm plane wave with an intensity of $\text{I} = 1014\text{W/cm2}$. The photons produced by this field should align well with the energies shown in the data harmonic spectrum. 63
Figure 23 The left side shows the spectrum from Figure 21. The right side shows the Fourier transformation of this spectrum for two different spectral phases. 64

Figure 24 LEFT. Typical M2 measurements for our laser system. RIGHT A schematic diagram of how an M2 is performed. It essentially involves measuring the beam waist at multiple points as it goes through focus. 66
Figure 25 LEFT depicts the position of the max-coords of a focal spot as a function of position. These show where the beam would shift over a 3-hr long experiment. RIGHT shows the x and y positions as a function of time. The jitter seems more consistent with random detector noise than anything inherent to the beam itself. 66
Figure 26 A schematic diagram of the FROG used in the UCI lab. 67
Figure 27 A set of FROG traces showing how the beam differs for different positions of the compressive gratings inside the laser box. It can be seen in the leftmost and rightmost traces that the width of the pulse elongates and becomes less symmetric as the beam is moved. At the best compressor spacing, the beam trace is narrowest. 68
Figure 28 Schematic of the OPA. This is a simplified model that intends to accentuate the two key processes that generate the resulting MIR. 69
Figure 29 Mach-Zehnder Interferometry of the plasma produced by a gas capillary backed with 408PSI of Argon (Ar). The density of the gas and the plasma can be determined by comparing the degree of fringe deflection relative to the control image. 71
Figure 30 LEFT The 3d CAD model of one our optimized gas cell designs. RIGHT A schematic depiction of the Gas cell breaking down and how it looks internally. 72
Figure 31 The change in pressure and fluid velocity due to a 45deg bend in an otherwise straight pipe. 73

Figure 32 This diagram was transposed from some of the official documentation included with the Andor camera. It depicts the quantum efficiency of our Andor x-ray camera as a function of photon energy. 74
Figure 33 The Hitachi Grating Spec Sheet. The two gratings employed in the heart of the two EUV spectrometers currently used in the UC Irvine Laser Lab. They are listed as part number "001-0437*1, 2" and "001-0639". Colloquially, the two gratings are simply called the "1200." 75
Figure 34 This depicts how a curved grating versus a flat grating project their diffracted orders. 76
Figure 35 Transmittivity for various 100nm foils These curves were generated from the data in the CRXO database[63]. 78
Figure 36 Annotated Overview of the operation of the code. 79
Figure 37 A sample calculation from the code. This shows the shape of the image plane for a range of wavelengths. 80
Figure 38 Flat field Hitachi grating imaging. This is a distillation of the information from Table 2. 82
Figure 39 CAD drawings of some of the vacuum chambers designed by the author. LEFT was the author's first chamber. It was designed using the spec sheet for the 600nm grating. It was manufactured in the UCI machine shop. RIGHT was a spectrometer assembly. 82
Figure 40 A schematic diagram depicting the experimental setup. 83
Figure 41 Results of shifting the grating position and angle. 84
Figure 42 Estimation of wavelength resolution of the spectrometer by using three closely spaced Oxygen Lines 85

Figure 43 A schematic setup of the experiment. 89
Figure 44 Flux Scaling for Gas Cell targets. "Channel length" (distance between orifices) versus peak flux of the 29th harmonic. 93
Figure 45 The "phase-matching" curves for four different types of targets. The lower bound absolute flux was quoted for each. The pumping system tended to crash when the ambient pressures began to exceed 10mTorr. The curve for the steel-drilled capillary could be acquired for higher pressures by "pulsing" the cell. ("Pulsing" refers to the technique employed of rapidly opening the regulator, acquiring data, then closing the tank again.) This technique did not work for the gas jet which tended to cause the pumps to fail before data could be acquired. So, the curve beyond 10mTorr was inferred from the preceding data points. 95
Figure 46 The LEFT plots are a set of simulations that keep the density in the interaction region constant. The y-axis in each plot marks the pressures in PSI along the lineout. The color bar marks the pressures in each of the 2d images. LEFT-TOP shows the results for the jet. LEFT-MIDDLE shows the result for drilled capillary. LEFT-BOTTOM shows the 3d-printed cell. The CENTER plots are Simulations results for a constant density of 80PSI. CENTER-TOP is the gas jet. Middle is the drilled capillary. CENTER-MIDDLE is the steel-drilled capillary. CENTER-BOTTOM is the gas cell. The RIGHT plot has the lineouts for each target. The colors in each image are related to the local pressure. The color bars are given for both simulation sets. 99
Figure 47 LEFT depicts how different numbers of photons in each arm can be combined to form the multiplicity of overlapping harmonic channels. The units of the y-axis in both of these plots are arbitrary. It was chosen so that the many colors (representing different orders or combinations) did not all overlap all in one place.

RIGHT shows a schematic setup of how the crossing of two beams generates secondary beams with k-vector distinct from the two drivers. The red arrows depict different numbers of photons combining from each arm. The black arrows show the resulting k-vectors..... 102
Figure 48 The raw image signal of the optimized noncollinear HHG. The color bar on the righthand side reports the counts reported by the detector. The overlaid lineout shows the total photon flux for the signal binned along the y-axis. The left hand scalebar estimates the absolute photon flux contained in the overlaid lineout. ... 104
Figure 49 Measurements of the EUV signal output with time. The reported counts were the peak counts contained within the 29^{th} harmonic. "Counts" are what the camera measures directly. As discussed in Chapter 3, these counts can be related to the absolute photon flux. The absolute flux was not calculated because the object of interest was the change in relative flux with time. After an initial increase in flux, the signal underwent a very slow decay. This was ultimately related to fluctuations and drifts in the backing pressure output. 105
Figure 50 Azimuthal polarization states. The lefthand side shows vector polarization. Every point of the beam has the same phase, causing the pattern of intensity to appear uniform. The brightness of this uniform pattern would dim and brighten with a period equal to $c0/\lambda$. The right-hand side shows vortex polarization. The hourglass-shaped intensity pattern would appear to rotate around a central point. The 3d images show the appearance of the phase fronts. For vector polarization, the fronts appear reminiscent of a series of pancakes. For vortex polarization, they appear like a spiral, spaghetti pasta noodle. 110

Figure 51 A graphical diagram of the various applications of vortex and vector beams. 111
Figure 52 The refined gas harmonic setup. The laser is aligned to pass through two bottlenecks or pinholes which serve to impede the flow of the gas from the target. The dotted lines demarcate the different segments of the system. Each of these regions was observed to equilibrate at different pressures depending on the target backing pressure. Both the interaction chamber and the connective piping before the spectrometer were backed by acp28 roughing pumps. The spectrometer was pumped via a hipace 300. 113
Figure 53 RIGHT Schematic of the setup for observing the focal beam profile of vector-polarized MIR. The action of the SHG crystal was like that of a linear polarizer. LEFT A raw image of the CCD display feed. The double-lobed structure of the beam would rotate in tandem with the rotation of the nonlinear crystal. 114
Figure 54 A camera photo of the near field of the 1300nm beam. Like the eye, the silicon chip of a phone camera should also not be able to see the 1300nm. Instead, it is likely seeing leftover "white light" from the "Topas Prime". Unlike a human eye or a scientific camera, the phone camera used here did not have the dynamic range to resolve the mottled-cookie-looking near field described in the paragraph above. Instead, the brightest part of the beam appear to be uniformly saturated. The picture does capture the relative size, color, and shape of the visible parts holdover inside of 1300nm. 116
Figure 55 Gas-harmonics driven by 800nm (indigo-color) and 1300nm (teal-seafoam color) beams. These each represent a single shot with minimum exposure time and "FVB" acquisition mode. The signal for the 1300nm was orders of magnitude less

than that of the 800nm. The 1300nm signal was multiplied by 50 to make its counts comparable to the 800nm. 117
Figure 56 The straight through signal of the optimized EUV. These shots bypassed the diffraction grating. The x and y scales are marked in detectors pixels (each $\boldsymbol{13um \times 13um}$). The colorbar is arbitrary, normalized to the max counts contained in each image. The plaid artifacting is due to transmission through meshed EUV filters. The key takeaway is the appearance of the beam profile. LEFT The linear polarized Gauss. RIGHT The ring/donut shaped vector beam..... 118
Figure 57 Comparison of the 1300nm Phasematching curves for four different situations. TOP-LEFT represents the control case: Linearly Polarized Gauss. The other three sectors contain various forms of vector-polarization. The photon flux is reported as $\boldsymbol{photons/(eV \cdot shot)}$. This number was transformed from the raw detector counts using the known efficiency of $\boldsymbol{0.3\mu m}$ Zirconium as well as the response of the detector. Each horizontal row in the plots represents an image which has been fully binned in the vertical dimension. 119
Figure 58 This figure graphically summarizes the impact of wavelength on gas harmonic flux. It is the convolution of the single-atom and many-atom effects. The longer wavelengths mean that the single atoms present a smaller target during recombination. The different wavelengths also affect the macroscopic propagation of the beam itself. The negative dispersion contribution from plasma is greater and the positive contribution from neutrals is weaker. This means that it takes even higher backing pressures to phase-match. 121
Figure 59 This is a one-dimensional perspective of a laser-solid interface. The x-axis is in units of $\lambda 0$, the driving wavelength. The y-axis is in units of $ncrit$, the critical

density. The red squiggly line is intended to represent a beam interacting with a solid-density plasma. The beam is shown propagating through the under dense plasma regions until reaching the critical density surface. 127
Figure 60 This graphic is not actual data or measurement of prepulse. It is generated via analytic equations. Actual prepulse is not typically this well-behaved. The key takeaway is the suppression of the wings. The "original" line shows a temporal profile which can ionize material about a picosecond before the main femtosecond interaction. Whereas, for the frequency doubled profile, the intensity temporal drops off much more quickly. It no longer causes optical damage 1 picosecond before the main interaction. 129
Figure 61 The is a schematic of CSU experimental setup. The high-contrast 400nm was delivered into the target chamber from a KF100 port. It is focused with an off-axis parabola onto a solid density target. The beam from this interaction was specularly reflected into a high-resolution spectrometer. The distance from target to grating was about 1m from target to grating..... 131
Figure 62 These are not images. They are pseudo-images formed by stacking the data from multiple shots together. Each horizontal row of pixels represents a data image that has been one-dimensionalized by binning in the vertical dimension. Rows of pixels have been grouped together by target type. The x-axis represents wavelength. The wavelength gets longer going from right to left. The color map depicts the relative intensity of signal measured at each wavelength position. The units for this color map are in arbitrary units. They have been scaled by the maximum signal in each pseudo-image. 132

Figure 63 This figure displays two actual data-images side-by-side. The x-axis represents wavelength in nanometers. The y-axis represent solid-angle in steradians. The spatial extent of the harmonics along the y-axis appears to go beyond the lower edge. Overlaid over each image is a lineout. The color map represents the intensity of the signal at each point on the detector. The raw counts have been converted to $photons/eV \cdot sr$ using the known response of the detector. The displayed $photons/eV \cdot sr$ also divides out the efficiencies from $0.2\mu m$ aluminum filters and the grating.. 134
Figure 64 OSIRIS simulations which keep intensity fixed at $\mathrm{a0} = 1.2$, but compare the effect of two different plasma scale lengths L. The Leftmost plot depicts a scale length of $\mathrm{L} = \lambda/2$. The Middle plot depicts a scale length of $\mathrm{L} = \lambda/70$. The rightmost plot shows the output harmonic (Simulation Credit [94])..... 138
Figure 65 1d Simulations which keep the density fixed while scaling the density. From left to right the peak intensity is increased from $\mathrm{a0} = 0.1$ to $\mathrm{a0} = 10$. (Simulation Credit[94])..... 139

ACKNOWLEDGEMENTS

These are the people whose assistance was invaluable:

Professor Franklin Dollar supported and advised me through the PhD program. His encouragement and discussions inspired me to think differently about the world and myself. Your lessons have given me a new set of eyes. There's a vast gulf between the physics taught in classes and books versus the applied physics of the real-world. You and Amina were patient with me through those difficult lessons.

Amina Hussein is now a Professor at the University of Alberta. She was formerly a postdoctoral scholar in the Dollar Lab and my mentor in late 2019/early 2020. She helped me work through a challenging experiment involving an optic called the focal-shaper.

Mark Steinborn is the head of UCI's research machine shop. He taught me some valuable lessons about unit tolerances and trained me in some technical skills such as CNC machining. He was always patient when I needed help or messed something up (like cutting steel with the bandsaw).

Nick Beier, Matthew Stanfield, Tam Nguyen, Deano Farinella, Sahel Hakimi, and Yasmeen Musthafa were my former labmates. Thank you for your goodness, kindness, and accommodating natures.

Danny Attiyah, Chris Gardner, and Victor Flores were my labmates, friends, and "little brothers" these last years of the program. Thank you for the fun times and playing-along with my zany antics. It really has meant a lot to me.

This research was funded by the NSF.

VITA

EDUCATION

Doctor of Philosophy in Plasma Physics *2023*

University of California, Irvine *Irvine, California*

Master's in Plasma Physics *2019*

University of California, Irvine *Irvine, California*

Bachelor of Science in Physics *2016*

University of California, Irvine *Irvine, California*

RESEARCH EXPERIENCE

Graduate Research Assistant *2017–2023*

University of California, Irvine *Irvine, California*

TEACHING EXPERIENCE

Teaching Assistant 2016, 2018

University of California, Irvine Irvine, California

REFEREED CONFERENCE PUBLICATIONS

Millijoule few-cycle pulses from staged compression for strong and high field science

M Stanfield, NF Beier, S Hakimi, H Allison, D Farinella, AE Hussein, ... Optics express 29 (6), 9123-9136 *2021*

Homogeneous, micron-scale high-energy-density matter generated by relativistic laser-solid interactions

NF Beier, H Allison, P Efthimion, KA Flippo, L Gao, SB Hansen, K Hill, ... Physical Review Letters 129 (13), 135001 *2022*

Few cycle euv continuum generation via thin film compression

M Stanfield, H Allison, N Beier, S Hakimi, AE Hussein, F Dollar CLEO: QELS_Fundamental Science, FF2C. 7 *2020*

Constraining Temperature Profiles in High Energy Density Matter Through High-resolution X-ray Spectroscopy

N Beier, B Nima, V Senthilkumaran, H Allison, Y Musthafa, M Logantha, ... Bulletin of the American Physical Society 2022

High Repetition Rate, High Intensity Vector Beams at Short Wave Infrared Wavelengths

D Attiyah, H Allison, C Gardner, P Kazansky, D Schmidt, C Durfee, ... Bulletin of the American Physical Society *2022*

High Harmonic Generation from ultra-relativistic 400nm Laser Solid Interactions

H Allison, F Dollar

Bulletin of the American Physical Society *2022*

Measurement of heating depth of highly-ionized copper from relativistically-intense laser pulses

NF Beier, H Allison, F Dollar, Y Musthafa, V Senthilkumaran, MH Kabir, ... 2021 IEEE International Conference on Plasma Science (ICOPS), 1-1 *2021*

K-shell emission of highly-ionized copper from relativistically-intense laser pulses

N Beier, H Allison, Y Musthafa, F Dollar, V Senthilkumaran, R Hollinger, ... APS Division of Plasma Physics Meeting Abstracts 2021, TO03. 006 *2022*

Generating Relativistic Intensities via Staged Pulse Compression in Dielectric Media

M Stanfield, H Allison, NF Beier, S Hakimi, AE Hussein, F Dollar Compact EUV & X-ray Light Sources, JM3A. 22 *2020*

The role of hot electrons in the generation of anomalous X-ray spectra from ultra-intense laser-plasma interactions

A Hussein, K Flippo, F Dollar, L Gao, K Hill, S Hansen, R Shepherd, ... APS Division of Plasma Physics Meeting Abstracts 2020, ZO03. 006 *2020*

Few-cycle Relativistic Laser-Plasma Interactions at Kilohertz Repetition Rates

M Stanfield, H Allison, N Beier, Y Musthafa, S Hakimi, A Hussein, F Dollar APS Division of Plasma Physics Meeting Abstracts 2020, NO08. 005 *2020*

The Role of Polarization in Relativistic High Harmonic Generation

N Beier, Y Heffes, H Allison, M Stanfield, Y Musthafa, S Hakimi, A Hussein, ... APS Division of Plasma Physics Meeting Abstracts 2020, NO08. 004 *2020*

Mid-Infrared High-order Laser-Plasma Interactions in Solids

N Beier, T Nguyen, J Lin, M Stanfield, H Allison, S Hakimi, J Nees, ...

APS Division of Plasma Physics Meeting Abstracts 2019, PO4. 014 *2019*

Soft X-ray Measurements of High Intensity Kilohertz Laser-Solid Interactions

H Allison, N Beier, S Hakimi, M Stanfield, F Dollar

APS Division of Plasma Physics Meeting Abstracts 2019, TP10. 067 *2019*

Mid-Infrared High-order Laser Plasma Interactions in Solids

T Nguyen, N Beier, J Lin, H Allison, D Farinella, S Hakimi, M Stanfield, ...

APS Division of Plasma Physics Meeting Abstracts 2018, PP11. 020 *2018*

Scaling Self-Phase Modulation in fused silica to MIR Wavelengths

M Stanfield, D Farinella, N Beier, H Allison, S Hakimi, T Nguyen, T Tajima, ...

APS Division of Plasma Physics Meeting Abstracts 2018, PP11. 018 *2018*

Compact Kilohertz Laser Wakefield Acceleration

S Hakimi, H Allison, N Beier, D Farinella, T Nguyen, M Stanfield, T Tajima, ...

APS Division of Plasma Physics Meeting Abstracts 2018, NP11. 013 *2018*

ABSTRACT OF THE DISSERTATION

MULTI-WAVELENGTH HIGH ORDER HARMONIC GENERATION FROM INTENSE LASER PLASMA INTERACTIONS

By

Hunter Allison

Doctor of Philosophy in Plasma Physics

University of California, Irvine, 2023

Professor Franklin Dollar, Chair

Advances in high intensity laser systems enable large energies to be delivered to targets simultaneously with kilohertz repetition rates, making laser driven x-ray sources more accessible. However, the targets needed for full utilization of such sources are still lacking. This work will describe the process of x-ray generation via the high harmonic generation process and how high brightness can be achieved through macroscopic phase-matching. It will show the need for controllable target densities and share measurements of high brightness x-ray beams using carefully designed 3D printed gas cells. It will show how such a source can enable deep investigations into novel polarization and focusing schemes that have been unable to be observed before, such as the wavelength scaling of phase-matching for vector polarization states. Lastly, results from measurements from 400nm high-contrast drivers on laser-solid harmonics will be shown.

Chapter 1 Introduction

1.1 Optical Metrology

Metrology is the science of measurement. It is concerned with the calibration and traceability of measuring devices. Calibration establishes the relationship between one measuring device and another. For example, two separate meter sticks both nominally measure "one meter". However, depending on the quality of manufacturing or the environmental wear of each device, a meter on one stick might be 0.97±0.005 m on the other. This kind of direct comparative measurement would establish the calibration between the two sticks. Using this calibration, two people geographically separated from each other can take measurements, convert between one another's units, and make meaningful statements about their respective measurements. This is essential for the outworking of science.

One of fundamental principles of science is that the laws of physics apply universally[2]. This means that one person's measurements taken at one time and place also apply elsewhere. This relies not only on a shared uniformity and trustworthiness of human perception but also on the regularity of the natural world. The atoms that composed a wooden measuring stick one hundred years ago are the same fundamental kind of matter that exists in a measuring stick made today. In other words, carbon atoms have apparently not fundamentally changed their bonding behavior or physical radii.

It is a bit of a wild understatement to say that the axioms or assumptions of science are just plausible. If this thesis is being read on an electronic device, the proof is right before the reader's eyes. Every day, the physics that undergirds the working and operation of human technology continues to stand. The sun rises and sets. The complicated and highly engineered systems of distribution and production continue to support a growing human population. The physics written in textbooks 100, 200, and even thousands of years ago can still be found to have relevance. Yes, theories expand and refine as measurements continue to be taken. However, even when a principle is misunderstood, a measurement is a measurement. Those fundamental experiments from yesteryear can be set up, reproduced, and repeated.

Just to demonstrate, the longest running experiments in humanity's shared ten-thousand-year written history have involved the observation of cosmic bodies. The ancestors of modern-day humanity made observations of the sky that can be corroborated by those of today[3]. Modern observations can assess the veracity of the star mappings of our ancestors by "turning the clock back". To this end, the theories of physics, mathematics, and logic are like connective tissue of causality. This discussion segues into the second important aspect of metrology, its traceability mentioned earlier.

Traceability refers to a connective-chain of calibration [4]. A direct comparison of every measuring device with every other would not be feasible. Agreement is established by comparison to some limited number of high-precision prototypes or originals. By logic and transitive property, two measuring devices that each separately cohere with a third measuring device must also cohere with each other. In a machinist workshop, uniformity is enforced by a set of calibrated blocks[5] in a temperature-controlled, clean

room setting. All machines, dials, and tools in the shop are calibrated against the machinist's blocks. Those blocks are the products of some even-higher precision originals. They are fabricated, certified, tested, and distributed by a reputable source to machine workshops across the world. Those masters are calibrated against some universal standard that sits at the very top of the chain of traceability.

SI or "Standard International" units known today were successively formalized at conventions beginning in the eighteenth and nineteenth centuries. At one of those conventions in 1875, among other events, a prototype of "the kilogram" was established. Copies of these prototypes were fabricated within some accuracy and distributed. Since the late 1800s, further measurements of "the kilogram" have established a comparative drift between the copies with time. At the very most, some copies differ between one another by as much as 75µg [6].

75uG might seem like a negligible difference. It could very well be, depending on the experiment and the acceptable tolerances of the project. However, an experiment that would want to know the fundamental limits of a theory would want to measure some fundamental property to the highest degree of accuracy. One of the axioms of general relativity relies on the equivalence of gravitational and inertial mass[7]. For this purpose, a 75uG difference in mass may be one of the primary limiting factors in the resolution of the measurement.

This is the problem with any universal standard that relies on a physical object. Matter is subject to physics and chemistry. Meter sticks and volumes of liquid change in density and size alongside temperature fluctuations in the environment. A kilogram will change mass due to handling, scuffing, or oxidation. No copy of a measuring device is a perfect replica. Additionally, even if the measuring devices start out

"identical" within some tolerance, they could still slowly begin to differ with time. Any measuring devices that trace or derive their calibration from such an original would suffer a long timescale drift. These drifts would produce systematic uncertainties with measurements done at earlier or later times in the same lab[8 9].

In response, there has been an increasing push to define universal standards based on fundamental properties and constants of physical reality[10]. Within the timescale of human history, the constancy of universal laws can be benchmarked against star position observation. On the timescale of the universe, constancy can be benchmarked using models of stellar and big bang nucleosynthesis. These are models that relate abundances of matter at past times to their present abundances[11 12]. These sorts of measurements constrain the long timescale drift of various physical constants[13 14]. This knowledge is important to assess how long timescales may create systematic drift in the calibrations of measuring devices. It is also something that would have to be reckoned with anyway, even with a universal physical standard. Hypothetically, these too will drift due to changing physical constants together with drift due to human handling procedures [8 9].

If a beam of light is derived from a coherent source, it has a phase and amplitude with a well-defined relationship with respect to time and space. The details of the beam at one time can be used to accurately determine its properties and details at another. The effects that can arise from this coherence can be used in high precision measurements. The tolerance and error bars of these measurements can be quite small. They are derived from the quality of the light source. Optical-based instruments and technologies have increasingly supplanted physical gauges due to their precision [15].

1.2 Early History of Optics

The survival and success of human beings can be credited to their ability to recognize patterns in the environment. In this endeavor, the eye itself, paired with the human brain, was one of the first scientific instruments. With it, humans could observe the behaviors of animals, identify edible and useful plants, and learn the "lay of the land". These observations gave early humans survival advantages, which they discovered could compound from generation to generation via language [16].

Over time, humankind became less susceptible to environmental circumstances. Instead, humans used their knowledge to reorder, transform, reshape, and control the natural world. This brought about a transition from nomadic hunter-gatherer to a new sedentary lifestyle involving domesticated animals and agriculture. Humans began to use the naked eye to count the stars and used their repetitive movements as a timekeeping device. However, beyond just survival, humans assigned meaning and found stories in the movements of the cosmos. The very foundations of astronomy can be traced to these long nights gazing at the stars. The oldest surviving survey of the stars can be dated to the ancient Egyptians in approximately the second millennium BC [17].

Eventually, human curiosity turned to studying the instrument and outworking of the eye itself. This was the trustworthy "instrument" which had cemented their place at the top of the natural order. It is here that the study of optics began in earnest. In modern terminology, optics refers to the science and study of light. However, the etymology of the word can be traced to the proto-Indo-European root "[18]okw-"which

simply means "to see" [18]. The first foray into the understanding of light came from investigations of sight and its operation.

The oldest and most comprehensive surviving treatments of optics come from the Greek Philosophers in the fourth and fifth centuries BC. Hippocrates and Aristotle performed dissections and put forth anatomical diagrams of the eye. The dominant model for living bodies in general was "Humourism". These theories proposed that a healthy living body contained various "vital fluids" in equilibrium with one another. In line with this model, sight was speculated to be mediated by a special humor carried along the "duct" of the optic nerve. The eye was tactile, touching the environment with the fire-element or sight-humor. Democritus would elaborate further. He contributed the idea that tiny particles called corpuscles emitted from the eyes. These corpuscles extracted other particles from the environment that would reconstruct within the eye. This was the reason for the tiny image of the world that could be seen from inside the pupil [19].

Euclid in the third century BC wrote the book titled the *Elements of Geometry*. Here, he built upon what came before, but he finally put it on geometric and mathematical footing. Euclid's [20]traveled along ray-like paths that emerged from the eyes and returned. In *Elements*, Euclid diagrams how the perception of the size and position of objects comes about due to the geometric angles subtended by the eye rays. He shows how nearer and approaching objects subtend larger ray angles that increase with size [20].

These geometric theories would later be expanded with the invention of transparent glass. In the first century BC, Heron of Alexandria proposed the law of reflection and Ptolemy was the first to measure the refraction angle of light traveling from air into

water. Ptolemy proposed an empirical formula for the angles of incidence and refraction[21] (i and r): $r = u\,i - v\,i^2$. With the decline of Rome and the later destruction of Alexandria, further study mostly ceased. Euclid's writings, in particular, would survive as a textbook for at least another twenty centuries. Just as a brief aside, it is interesting to consider: "What if history had proceeded differently? What if this hub of learning had not been destroyed? What kind of 21st century world would be here today?"

The invention of the printing press resulted in the rapid dissemination and sharing of knowledge. Discoveries made in the Middle Ages could be shared. These included the many advancements in math and science by Arabic scholars in Bagdad. In the 1100s, an Islamic scholar named Ibn al-Haytham was perhaps the first "true scientist" and optical physicist. In his *Book of Optics* he emphasized a scientific method in which knowledge was confirmable via mathematics and reproducible procedures. His contributions to optics were numerous, overturning many of the Greek theories. He formulated Al-Hazen's law of reflection based on studies of curved mirrors and lenses. He measured dispersive phenomena and correctly identified the cause of atmospheric phenomena such as rainbows, the "moon illusion", and afternoon twilight. He even estimated the atmosphere's height by measuring the duration of twilight. His number of 80km was within an order of magnitude of the modern accepted value of 380km. Lastly, he created the forerunner of the modern camera, the *camera oscura*. He detailed its design and operation [22].

Al-Haytham's *Book of Optics* was widely circulated throughout Europe around the time of the Scientific Revolution. Many of his ideas and those of other Medieval thinkers were expanded upon during the Enlightenment [23]. It is here that the science

of Optics begins to take the form familiar to how it is known today. For example, while a precursor of Al-Haytham named Ibn Sahl wrote the law of refraction as the ratio of sides of a triangle, it was Snell who would write it in familiar form: $n_1 \sin(\theta_1) = n_2 \sin(\theta_2)$. The science of Optics collided with familiar names still cherished today, such as Newton [24], Galileo, Huygens, and Fraunhofer. The finite speed of light would be inferred in 1676 by Danish astronomer Ole Christensen Rømer through the measurement of the apparent eclipse durations of Jupiter's inner satellite, Io [25]. A contemporary of Rømer named Huygens would formulate a wave-theory of light that was not initially accepted until later vindication by Thomas Young [26]. Much later in the 1800s, the physicist Wilhelm Eduard Weber would recognize the similar values between $\frac{1}{\sqrt{\epsilon_0 \mu_0}}$ and the measured speed of light [27]. Finally, in 1865, Maxwell published the *A dynamical theory of the electromagnetic field* [28] . Here, he showed how the laws of Ampère, Gauss, Faraday, and Coulomb cohesively merge into wave equations for electromagnetic fields. From the equations for these fields, the laws of optics can be derived.

It is from here that the modern understanding of light and optics begins. A story that traces its origins through hundreds of years of collective thought and inquiry. Like the grapes of a vineyard, these thoughts have been nurtured, pruned, and distilled with the passage of time.

1.3 Modern Application of Optics

Since Maxwell, the understanding of light has greatly advanced. The production of light pulses has become commonplace. Light-based tools and measurements first revolutionized the fields of astronomy and biology. They allowed humans to amplify

the capabilities of their natural senses to see the very small as well as those from afar. Astronomers could now peer further into the cosmos to observe stars and features that are invisible to the naked eye. Biologists gained a tool for peering inwards and could observe the never-before-seen self-propagating building blocks of life. The emission and absorption of light became a useful tool for studying composition of matter and fundamental subatomic interactions. The core applications of light most relevant to this thesis are these:

- Spectroscopy
- Observation of fast events and physical phenomenon (i.e., High speed photography)
- Optical Vortices

Light has been an instrumental tool in the advancement of modern science.

1.3.1 Spectroscopy

Spectroscopy is the study of how matter interacts with the different colors of light. Joseph von Fraunhofer was the first to extensively use diffraction grating. The grating allowed him to isolate the component colors of light and see its spectral composition [29]. In 1811, while working as an optician at the Untzschneider Optical Institute at Benediktbeuern, near Munich, he noticed something peculiar when decomposing the spectral content of sunlight. He found dark bands in an otherwise continuous spectrum [30]. It was later discovered that the lines that appeared in sunlight also appeared in the optical light from the plasma emission of hydrogen! These spectral

lines were later observed to be present in the invisible ultraviolet and infrared parts of the light spectrum. See illustration in Figure 1.

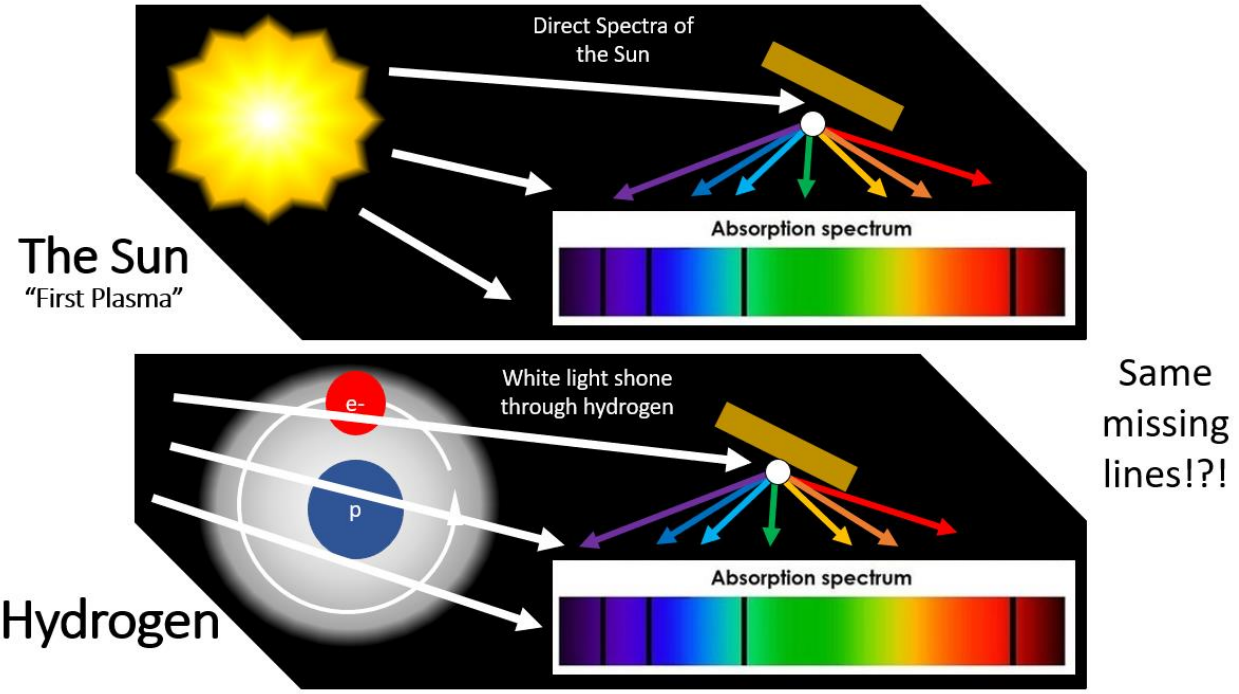

Figure 1 The light observed from the sun appears as a continuous band, but with some colors missing. These same discrete lines would appear when hydrogen gas was illuminated by white light.

The observation of these discrete energy bands was one of the mysteries that pointed toward quantum mechanics[31]. The word quantum is derived from the Latin phrase "how much." It refers to the fundamental concept that undergirds the whole theory: the quantization of space, time, matter, and energy. Early models of atomic structure proposed something reminiscent of gravitational orbits. The electrons were thought to orbit the nucleus like planets orbiting a star[32]. These classical models of the atom allowed for a continuous range of energies. An electron was thought to be able to have any energy within some range. The observations of Fraunhofer, Lyman, Paschen, and others did not mesh with this established theory. The key breakthrough

in understanding came with the recognition of the wave nature of subatomic particles. Classical theory had understood waves and particles as being mutually exclusive categories. Particles were chunks of mass with infinitesimal spatial extent. They were characterized by a well-defined position and momentum. Waves, on the other hand, were understood as propagating disturbances or displacements in an otherwise uniform energy or force field. These variances or displacements were characterized by well-defined wavelengths or frequencies. It was discovered that there are no pure waves or particles. Rather, all physical substances have a dual nature and embody the properties of both categories depending on the spatial scale of observation[33].

The appearance of lines in the emission and absorption spectra was an example of the electron wave nature. The equations of motion for the bound states of the electron are wave functions. An extremely simplified model for the bound electron is the so-called "infinite potential well[34]." The electron is trapped in an inescapable box but free to move unrestricted within the box. The discrete energies that arise are comparable to those of a string of length L held taut at both ends. The requirement that the wave amplitude goes to zero at either end of the string is what restricts the allowed wavelengths to distinct values. Specifically, the wavenumbers are integer multiples or "harmonics" of 1/L.

A more accurate one-dimensional model uses a "harmonic well potential." These have equally spaced characteristic energy levels. Like the infinite well, this is still not entirely realistic though. The three-dimensional generalizations of the string held taut are the spherical harmonics. They come about by treating a single electron and proton as a fully three-dimensional damped oscillator system [35] [36]. Even this is only an approximation. Most real-world atomic systems contain many atoms and nucleons

strongly coupled together with a mess of overlapping and interacting wavefunctions [37]. The math associated with these wavefunctions quickly becomes intractable and impossible to solve analytically. They can be approximated using numerical methods with experimental measurements used to constrain the model. Figure ***2*** illustrates this idea. The series of spectroscopic lines of a system involving many protons and electrons can be measured just as easily as a simple hydrogen atom. Even though, the equations of one is much more difficult to solve.

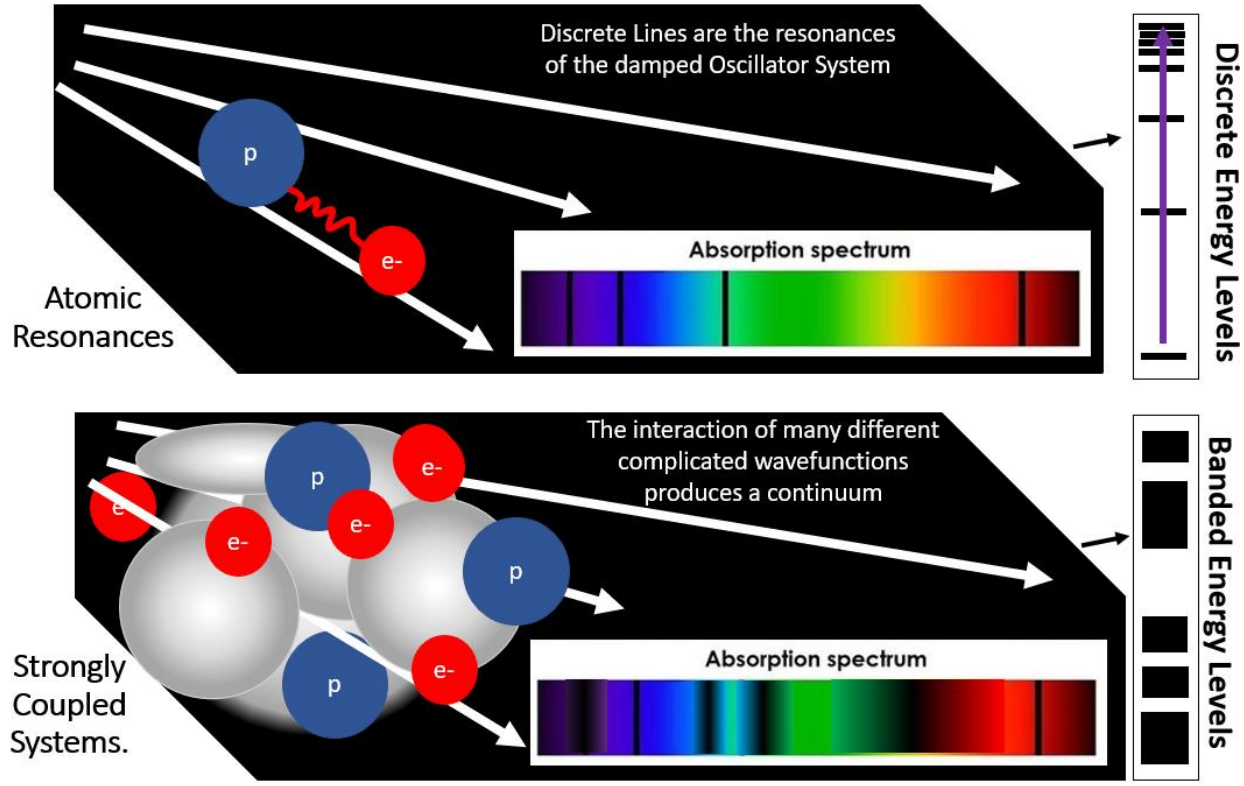

Figure 2 A single proton-electron pair can be solved analytically. The energy levels are discrete resonances. Whereas, for many atoms, the energy levels densely overlap and are basically impossible to solve analytically. However, they can be measured experimentally!

Spectroscopy has been a historically important tool for revolutionizing the human understanding of the world at its most basic level. It continues to find relevance as a

diagnostic tool for probing the states of a matter sample. The spectroscopic line magnitudes are intimately related to the atomic and chemical state of matter. Every possible atomic state forms a kind of identifiable "fingerprint". Many samples contain a multitude of atoms in various configurations. The magnitudes of the different overlapping "fingerprints" can be used to isolate which configurations are dominant[38] [39]. An area of active interest involved what are called "pump-probe" methods. These involve seeing how the dominant equilibrium configurations change as the experimenter interacts with the sample in controlled ways [40]. An experimenter might, for example, compare the spectrum of a sample when a light or laser is illuminating the sample versus when it is not.

As another example, plasma spectroscopy has been a mainstay in the science of understanding the physics of "high energy density" materials. Plasmas are too hot for physical probes which poke into the material. Anything stuck inside the plasma will become plasma itself [40]. So, spectroscopic characterization of the light emitted by the plasma can and has been useful for indirectly inferring the temperature, composition, and charge states of the plasma [41].

1.3.2 High-Speed Photography

The processes and speed of human visual perception is currently an area of active neuroscience research. The light that hits the retina is converted to electric signals by cells containing photoreceptive pigments. The brain takes this pattern of electrical signals and performs seamless visual processing as well as data acquisition. It can be observed that humans are able to perceive and correctly identify images seen for just 13ms or less [42]. For shorter duration events, it can even be observed that visual

information that is not consciously perceived can still leave impressions on the cortical neurons[43].

The storage and recall of the human visual system are aspects of human physiology that have made hunters and gatherers successful. It works very well within a specific spatial and temporal domain. In fact, current research using ex-vivo neural tissues has attempted to replicate it to some extent [44] [45]. Not just to satisfy human curiosity, but also to refine existing machine-vision-learning models. However, as good as it is, there are evident limits to human visual perception. The details of fast motions like the beating of a hummingbird's wings become blurred. Room lights and monitors appear to offer continuous illumination but can be observed to flicker rapidly when slowed down. 13ms seems relatively instant. Yet, it is a literal eternity for objects moving and interacting at or near the speed of light. On femtosecond timescales for example, one second is akin to the entire age of the universe for us. The great power of high-speed photography has been the ability to record visual information and slow it down.

The field of fast photography traces its origin to Edweard Muybridge [46,] . The basic principle of photography at the time was that of a dark box containing photochemical films. These early photographic methods were limited in their capability. They could only capture static scenes or objects. Anything that was not static appeared blurry or, sometimes, ghostlike. Muybridge took advantage of two technological convergences in chemistry and physics. The chemistry innovation came in the form of fast exposing films, whereas the physics innovation came in the form of electronic tripwires and fast shutters. Edweard built multiple cameras and lined them up in

series along a racetrack. As the horse and its rider zoomed past, each camera would fire in sequence.

The commonly claimed motivation for developing this technology was a wager made by Leland Stanford. This is disputed, however. Some scholars state that Stanford employed Muybridge as a form of "scientific philanthropy". It is hypothesized that this kind of philanthropy was a kind done to put his business in a good light and market himself as a "man of science" [47]. He was a proponent of "unsupported transit", the hypothesis that a horse at full gallop lifted all four legs off the ground. The photographic series taken from Reference [48] and shown as Figure ***3***. Frame two and three of Muybridge's photographs proved Standford's conjecture. They also shook the world of art. Since the very dawn of human history humans had depicted horses in art, but it turned out that many of these depictions were inaccurate. These artistic representations typically showed them in a pose known as a "flying gallop" where all four legs were lifted off the ground and outstretched to either side [49]. It turned out that, at some point, running horses would fold their four legs underneath them.

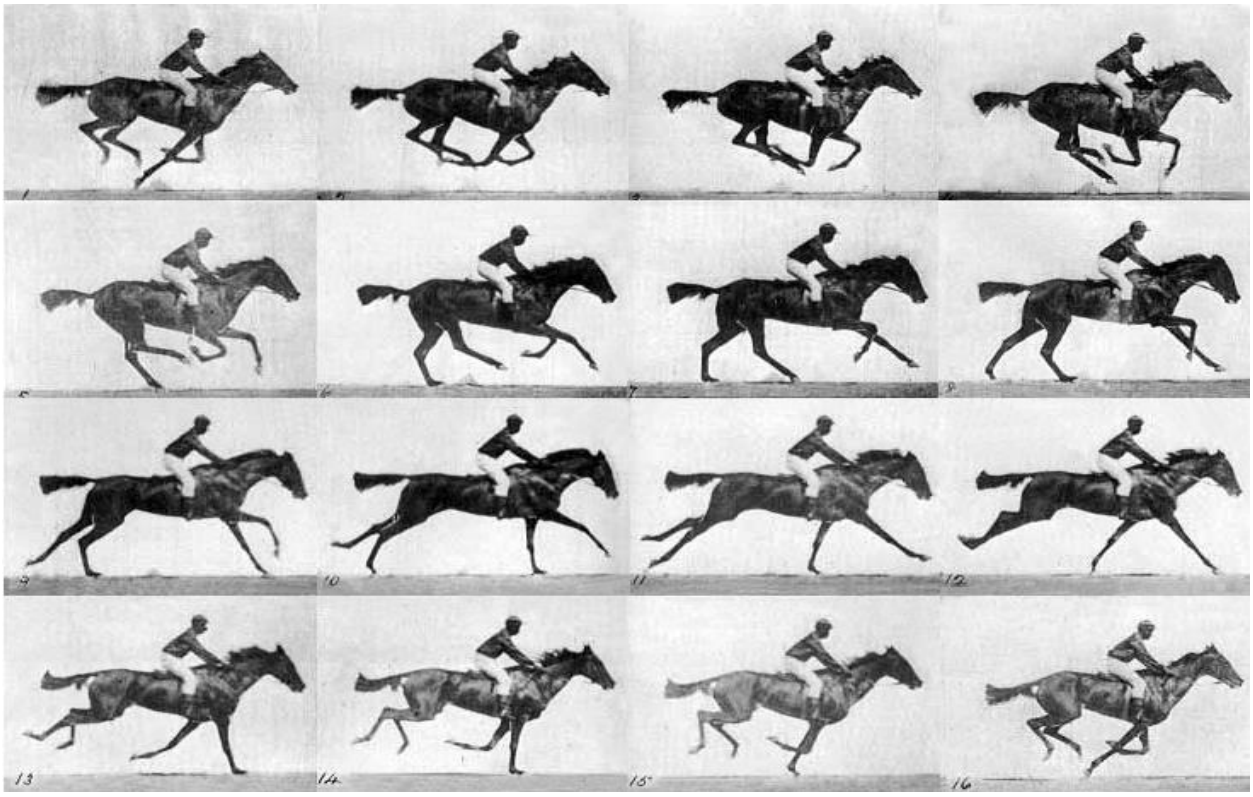

Figure 3 Muybridge's photos of the galloping horse. The key images that won the wager are the ones on the top row.

Muybridge would end up using the money to conduct further studies of animal locomotion and refine his photography techniques [50]. Since this initial proof of concept, the techniques of fast photography have continued to be refined in step with improving technology. The measurement of time is always relative. To measure something fast, you need something faster than the fast event in question. Figure ***4*** is an illustration of this principle. Muybridge measured time relative to how fast his photographs could be exposed. Quartz wrist watches measure time relative to oscillations of a crystal lattice. These crystal oscillations have periods of a few ten-thousandths of a second. Since Muybridge, the field of motion capture has pushed to observe shorter and shorter timescales.

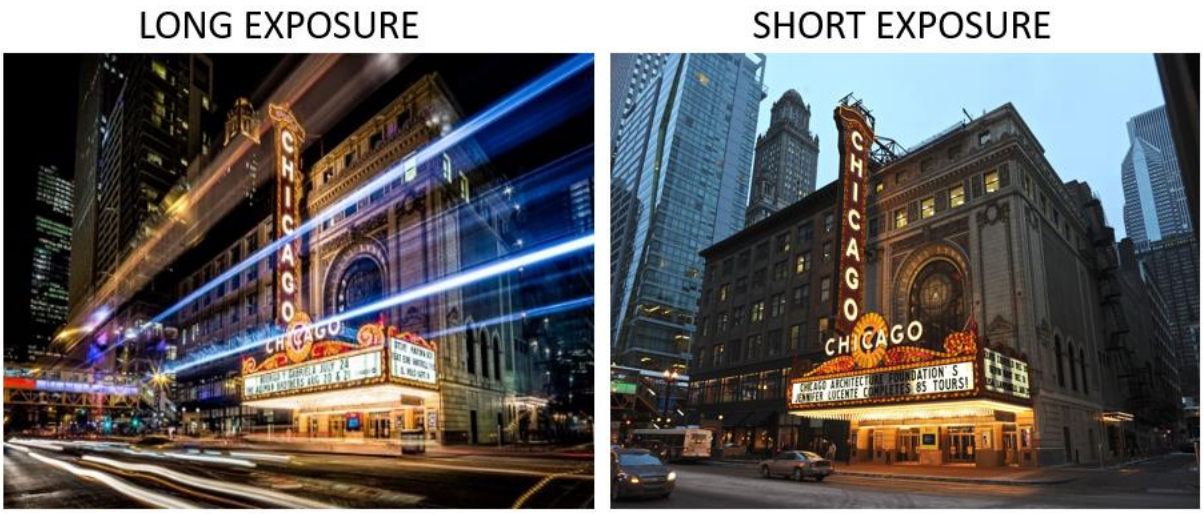

Figure 4 Motions occur on a variety of timescales. To see something fast, the experimenter needs a detector faster than the event itself. In the long exposure shot, the things that do not move over the course of minutes like the buildings and parked cars are in crisp focus. The fast-moving objects, traffic and people, appear as shimmering light trails. In the short exposure shot, all objects appear in crisp focus, frozen in time. Light Trails in front of a theater, photo reference [51]. Resolved picture of the theater, phoro reference [52].

The public imagination would later be captured again almost one hundred years later by the electrical engineer, Harold Edgerton. By some, his 1964 image of a .30-caliber bullet splitting the apple is regarded as much as an art piece as a technological achievement. His great contribution to fast photography was the replacement of Muybridge's mechanical shutter with an optical one. Flash lamps of the past had relied on "flash powder" and long-charging capacitors. The capacitor would spark the powder as it discharged. Edgerton's design obfuscated the need for capacitor banks. He found a lamp filled with inert gas that could be turned on and off as fast as electricity could be applied. Using these lamps, he was able to make pulsed light with duration of one millionth of a second.

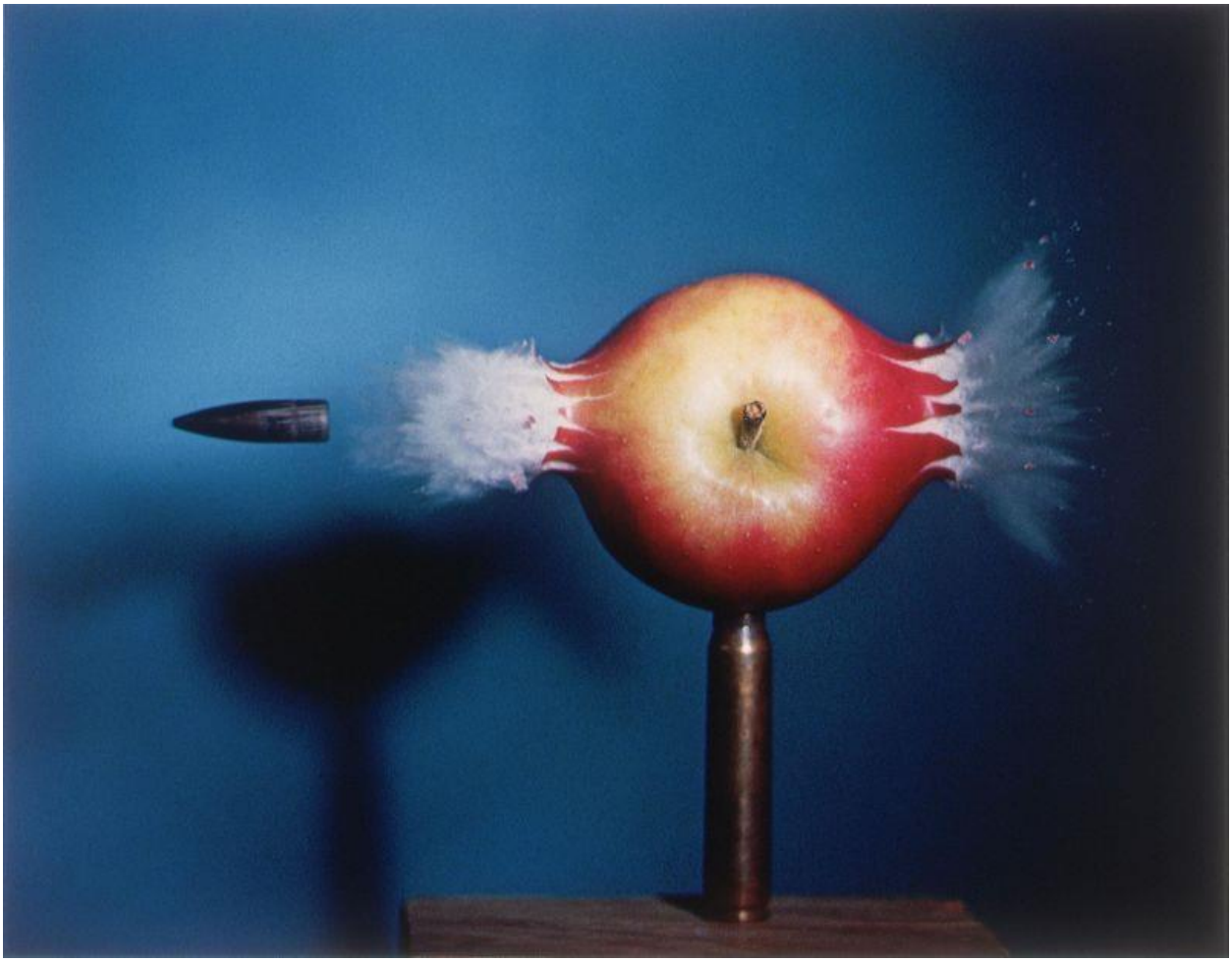

Figure ***5*** Edgerton's iconic bullet splitting the apple image captured using strobe photography. Photo reference[53].

Since the 1960s, the field has expanded on Edgerton's optical shutter. Improvements in LASER (Light Amplification by Stimulated Emission) have allowed the creation of even shorter light durations. At the present, 35 femtosecond light durations have become commonplace. These produce their pulses by using a technique called chirped-pulse-amplification (CPA) with titanium-doped-sapphire (Ti:Sapphire) crystals. One femtosecond is a billionth of a millionth of a second. Instead of apples and fluid droplets, these femtosecond light pulses are used to create movies that

document chemical interactions. Before this innovation, intermediate chemical states and reaction channels were a matter of inference and conjecture. Now, longstanding chemical models can be directly observed and tested.

The approaching frontier for fast duration light pulses is the attosecond regime. These are light pulses that are a thousandth of an attosecond. They can be produced from femtosecond duration light through highly nonlinear photon-mixing and high-harmonic processes. For the past thirty years or so, the theory has been rapidly maturing. Stable sources of attosecond radiation are already being realized. Femtosecond duration light sources have already been revolutionizing the field of chemistry. Attosecond light sources stand to revolutionize the understanding of atomic physics. See Figure ***6***.

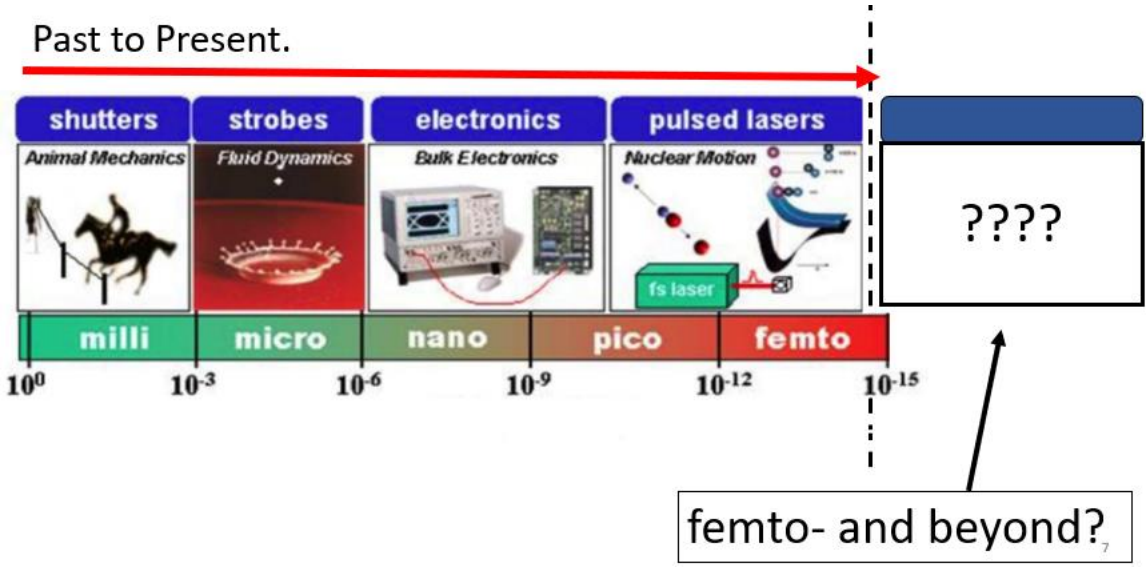

Figure 6 This diagram summarizes the characteristic timescale of various physical processes. Femtosecond lasers have been successful at observing chemistry in-action. The current frontier is the attosecond regime.

1.3.3 Optical Vortices

Laser light is produced through a process called stimulated emission. Matter in an excited state is stimulated by a photon with a resonant frequency to emit a photon with the same frequency. The effect is comparable to dominoes. The tipping of a single domino creates a downstream cascading effect that can knock down many dominoes. For lasers, a single photon initiates a process that causes many photons to gush forth all at once. Lasers take full advantage of this effect by trapping the light inside a box and making multiple passes through the crystal. The outgoing light is imprinted with the properties of the initial seed and details of the crystal lattice. So, a seed pulse with a uniform phase and polarization profile produces an outgoing beam with the same profile. Although this seed profile will typically get convolved to an extent with the spatial variations of the crystal, these crystal variations can be minimized rather easily by focusing the seed and transmitting through only a very small area.

Optical vortices -- an emerging area of interest -- refer to novel light modes and polarization states. Until recently, only beams with constant phase and polarization profiles have been readily accessible to researchers. Commercial products like the Solstice 35fs is a laser system with gain media composed of Ti:Sapphire. It offers a beam with a constant linear polarization across the beam profile. Waveplates can be used to rotate and change the relative phase between x and y components of polarization. Filters can change the relative magnitudes of various colors within the beam. Lenses can be used to change the beam diameter. However, up to this point, many optics act upon a beam uniformly. In other words, they do the same thing to every part of the beam.

Advancements made in nanofabrication have resulted in a renaissance of textured and designer optics. These are optics that can precisely change the local characteristics of a beam. This allows the creation of beams with properties that spatially vary across the pulse. For example, uniform linear polarization can be transformed to what is referred to as "radial polarization." This refers to a beam whose polarization state always points toward the center of the beam. Such beams have found application as "optical tweezers." This is an exciting consideration. They allow the precise manipulation and movement of microscopic particles and even biological cells. Another area of emerging interest is vortex polarization beams with a nonuniform phase profile which can impart orbital angular momentum (OAM).

A body in orbiting trajectory will typically have some "angular momentum" associated with it. The momentum of a body is a way of quantifying the relative strength of its motion. It is related to an object's kinetic energy. An object with considerable momentum requires more energy to bring it to rest, whereas the converse is true for an object with only slight momentum. Angular momentum is a way of organizing the quantity of rotational motion possessed by a body or system. Classical models of the proton-electron atomic system resembled gravitational systems. With this class of systems, angular momentum was an expected feature. In quantum theory though, the wave nature of the electron means that it does not orbit or spin in the classically understood sense, yet these orbits respond to externally applied fields as if they had an "intrinsic" orbital angular momentum. This is the origin of atomic "fine structure." It can be observed that trajectories with the same quantized energy can have different amounts of quantized angular momentum. Electrons inside unfilled valence shells can typically occupy any one of these shells depending on their energy.

The exciting feature of beam profiles with OAM or "orbital angular momentum" is that they can impart angular momentum to microscopic particles. These beams will possibly be able to probe fundamental quantum theories. Samples of molecules can be prepared with identical OAM states. Additionally, there are applications for micro-manufacturing and biology. Optical tweezers can precisely position microscopic objects, while OAM beams will be able to precisely orient them. For example, the orientation of cells in a tissue matters in certain muscle fibers. A biologist could use these sorts of beams to precisely orient cells and build complex tissues.

1.4 Statement of Purpose

Fast-exposing film and electronic shutters were things that other people had made. Muybridge's great innovation came from the simple act of combining them. The act seems almost inconsequential, yet the result was something spectacular that no one had ever seen before. The colloquial term for such a seminal work would be "lightning in a bottle." Muybridge's horse and Edgerton's apple are immortalized in the annals of science history. Other people might come later and attempt to replicate, echo, and mimic. Such efforts will never be able to quite supplant the original work. The horse and apple's meaning and importance is derived precisely from their temporal context. This is because the past is written. Nothing else can ever come out in precisely the same time and place. Hence, anything that comes later can only be what it is because of who and what preceded it. This is the nature of causality.

The author hopes that her story might echo that of Eadweard Muybridge. Spectroscopy, high-speed photography, and optical vortices were technologies with long histories that preceded the author's doctoral work. Spectroscopy was a mature

tool at the time of writing. Its beginnings went back at least 150 years. The objective of the author's work was that of unification: High-Speed EUV spectroscopy with designer light sources. Hopefully, the outcome of this research will emulate the process of making cookies, which takes the ingredients of flour, eggs, butter and sugar and utilizes a thermal process to produce a unique creation. Sometimes, a specific combination gains an identity distinct from the parts that made it. This is because it is recognized as something subjectively better and quantitatively more than any individual component. Based on the flour alone or any one single ingredient by itself, it is unlikely one would know how tasty a simple cookie could be. In the same manner, the hope is that spectroscopy, fast photography and optical vortices together might begin a new field of metrology and spectroscopy. Today's mysteries will be tomorrow's masteries.

The subsequent two chapters provide a theoretical background and the methods required for performing such experiments. The following three content chapters present several experiments producing novel attosecond light sources. Finally, a brief concluding chapter is presented.

Chapter 2 Background and Theory

2.1 Maxwell's Equations

The fundamental fields of electromagnetism are categorized in the table below.

Symbol	Name	Units	Constitutive Relations
E	Electric Field	N/C	
P	Polarization	C/m^2	
D	Electric Displacement	C/m^2	$\boldsymbol{D} = \epsilon_0 \boldsymbol{E} + \boldsymbol{P}$
B	Magnetic Flux Density	$N/A \cdot m$	
M	Magnetization	A/m^2	
H	Magnetic Field	A/m^2	$\boldsymbol{H} = \mu_0 \boldsymbol{B} + \boldsymbol{M}$

In modern formalism, they are most commonly and elegantly expressed as four equations written in vector notation.

$$\nabla \times \boldsymbol{H} = \frac{\partial \boldsymbol{D}}{\partial t} + \boldsymbol{J}$$

$$\nabla \times \boldsymbol{E} = -\frac{\partial \boldsymbol{B}}{\partial t}$$

$$\nabla \cdot \boldsymbol{D} = \rho$$

$$\nabla \cdot \mathbf{B} = 0$$

The connective relationships for **D**, **E** and **H**, **B** are given by the following expressions.

$$\boldsymbol{D} = \boldsymbol{P} + \epsilon_0 \boldsymbol{E}$$

$$\boldsymbol{H} = \boldsymbol{M} + \frac{1}{\mu_0}\boldsymbol{B}$$

In the above expressions, **P** and **M** represent induced fields. They arise in neutral matter due to external fields exerted by free charges and current. The connective equations establish **D** and **H** as the resultant or total field. They are fields measured by an experimentalist.

The force law for charges subject to the fields is $\boldsymbol{F} = q\,(\boldsymbol{E} + \boldsymbol{v} \times \boldsymbol{B})$

Together, the Maxwell Equations represent a system of partial differential equations. They are a complete theoretical description of the fields that arise and how they can evolve. While charges, moving and stationary, can be a source for these fields, electromagnetic fields can also exist absent the presence of any charge.

2.1.1 Wave Solutions to the Maxwell Equations

The classical wave equation is given by the following partial differential equation.

$$\frac{\delta^2 f}{\delta z^2} - \frac{1}{v^2}\frac{\delta^2 f}{\delta t^2} = h(z,t)$$

If $h(z,t)$=0, the wave equations have solutions with the following general form:

$$f(z,t) = g(z - vt) + h(z - vt)$$

The above expression represents the superposition of two waveforms, one moving to the right and the other moving to the left. Both waves move with phase velocity *v*.

In a homogeneous linear dielectric media, the polarization field **P** and the magnetization **M** are proportional to **E** and **B** respectively. The connective equations take a special form.

$$\begin{aligned} \boldsymbol{D} &= \boldsymbol{P} + \epsilon_0 \boldsymbol{E} \\ &= (\epsilon_0 \, \chi_e \, \boldsymbol{E}) + \epsilon_0 \, \boldsymbol{E} \\ &= \epsilon_0 \, (1 + \chi_e) \, \boldsymbol{E} \\ &= \epsilon \, \boldsymbol{E} \end{aligned}$$

$$\begin{aligned} \boldsymbol{H} &= M + 1/\mu_0 \, \boldsymbol{B} \\ &= (1/\mu_0 \;\; \chi_m \, \boldsymbol{B}) + 1/\mu_0 \, \boldsymbol{B} \\ &= 1/\mu_0 \, (1 + \chi_m) \, \boldsymbol{B} \\ &= 1/\mu \, \boldsymbol{B} \end{aligned}$$

The constants of proportionality are encapsulated by χ_e and χ_m. They are small nonzero numbers. The constants ϵ and μ are the permittivity and permeability in linear matter. With the above expressions for **D** and **H**, the Maxwell equations take on a more symmetric appearance.

$$\boldsymbol{\nabla} \times \boldsymbol{B} = \epsilon \, \mu \, \frac{\partial \boldsymbol{E}}{\partial t} + \mu_0 \, J$$

$$\boldsymbol{\nabla} \times \boldsymbol{E} = -\frac{\partial \boldsymbol{B}}{\partial t}$$

$$\boldsymbol{\nabla} \cdot \mathbf{E} = \frac{\rho}{\epsilon_0}$$

$$\boldsymbol{\nabla} \cdot \boldsymbol{B} = 0$$

The vector identity $\boldsymbol{\nabla} \times \boldsymbol{\nabla} \times \boldsymbol{A} = \boldsymbol{\nabla}(\boldsymbol{\nabla} \cdot \boldsymbol{A}) + \boldsymbol{\nabla}^2 \boldsymbol{A}$. Applying it to the expression for the curl of **E**:

$$\boldsymbol{\nabla} \times \boldsymbol{\nabla} \times \boldsymbol{E} = \; \boldsymbol{\nabla}(\boldsymbol{\nabla} \cdot \boldsymbol{E}) + \boldsymbol{\nabla}^2 \boldsymbol{E} = \; -\boldsymbol{\partial}/\partial t(\quad \nabla \times \boldsymbol{B} \quad) = \nabla \times (-\boldsymbol{\partial B}/\partial t)$$

$$\boldsymbol{\nabla}\left(\ \frac{\rho}{\boldsymbol{\epsilon_0}}\ \right)+\boldsymbol{\nabla}^2\boldsymbol{E}=\ -\boldsymbol{\partial}/\partial t(\epsilon\,\mu\,\frac{\partial \boldsymbol{E}}{\partial t}+\mu_0\boldsymbol{J})$$

After some rearrangement…

$$\boldsymbol{\nabla}^2\boldsymbol{E}+\ \epsilon\,\mu\,\frac{\partial^2\boldsymbol{E}}{\partial t^2}=\ -\boldsymbol{\nabla}\left(\frac{\rho_0}{\boldsymbol{\epsilon}}\right)-\frac{\partial}{\partial t}(\mu_0\boldsymbol{J})$$

This is the 3-dimensional generalization of the classical wave equation with $\frac{\delta^2}{\delta z^2}\rightarrow\boldsymbol{\nabla}^2$, $f\rightarrow\boldsymbol{E}$ and $v\rightarrow\frac{c_0}{n}$. Here the expression on the righthand side represents the term $h(z,t)$ seen in the classical wave equation. They are the source or driving terms. Comparison with the eave equation reveals that the wave speed v is equal to $1/\sqrt{\epsilon\mu}=\sqrt{\frac{1}{\epsilon_0\mu_0}}\sqrt{\frac{1+\chi_m}{1+\chi_e}}=c_0/n.$ In the preceding expression, c_0 represents the speed of light in vacuum and n index of refraction. In dielectric media, the polarization and magnetization terms tend to oppose the externally applied fields. This leads to χ_e and χ_m tending to be negative and the phase velocity of light in material tending to be $< c_0$.

It assumes plane wave expressions of the form $e^{i(\boldsymbol{k}\cdot x-\omega t)}$ for the electric field and source terms, then $\nabla^2\rightarrow k^2$ and $\delta/\delta t\rightarrow -i\omega$. The differential equation that expresses the wave equation becomes an algebraic one. Let $\boldsymbol{E}=\widetilde{\boldsymbol{E_0}}\,e^{i(\boldsymbol{k}\cdot x-\omega t)}$, $\boldsymbol{J}=\widetilde{\boldsymbol{J_0}}\,e^{i(\boldsymbol{k}\cdot x-\omega t)}$, and $\rho=\widetilde{\rho_0}\,e^{i(\boldsymbol{k}\cdot x-\omega t)}$. (The tilde over the amplitude denotes that it is a complex number $|\boldsymbol{A}|\,e^{i\,\phi}$. In general, $\widetilde{\boldsymbol{E_0}}$, $\widetilde{\rho_0}$, and $\widetilde{\boldsymbol{J_0}}$ will be functions of $\boldsymbol{k}$ and ω.) The wave equation becomes:

$$\mathrm{k}^2\widetilde{\boldsymbol{E_0}}-\omega^2\,\epsilon\,\mu\,\widetilde{\boldsymbol{E_0}}=\ -\mathbf{k}\left(\frac{\widetilde{\rho_0}}{\boldsymbol{\epsilon_0}}\right)+i\omega\left(\mu_0\widetilde{\boldsymbol{J_0}}\right)$$

$$\widetilde{\boldsymbol{E_0}}=\frac{-\mathbf{k}\left(\frac{\widetilde{\rho_0}}{\boldsymbol{\epsilon_0}}\right)+i\omega\left(\mu_0\widetilde{\boldsymbol{J_0}}\right)}{k^2-\omega^2\,\epsilon\,\mu}$$

The above expression relates the amplitudes of $\widetilde{\rho_0}$ and $\widetilde{\boldsymbol{J_0}}$ to the electric field amplitude. It indicates that a sinusoidal variation of charge and/or current (whether in time or space) will excite an infinite plane-wave electric field with amplitude $\widetilde{\boldsymbol{E_0}}$. (NOTE THIS, it will be important in the next section!) This is the solution for the electric field in what is called "Fourier Space" $(\boldsymbol{k}, \omega)$. We are typically concerned with the value of the electric field in "real space" $(\boldsymbol{x}, t)$. The real space electric field can be found by finding the integration (or summation) over each of the plane waves. (This is otherwise known as "taking the inverse Fourier transform".)

$$\boldsymbol{E}(x,t) = \int d\boldsymbol{k}\, d\omega\ \widetilde{\boldsymbol{E}_0}(\boldsymbol{k},\omega)\, e^{i(\boldsymbol{k}\cdot x - \omega t)}$$

In free space with no source terms (ρ and J equal to zero), the expression for $\widetilde{\boldsymbol{E}_0}$ becomes:

$$\widetilde{\boldsymbol{E_0}} = \frac{0}{k^2 - \omega^2\, \epsilon\, \mu}$$

$\widetilde{\boldsymbol{E_0}}$ is trivially equal to 0, unless $k^2 = \omega^2\, \epsilon\, \mu$ or $\boldsymbol{k} = \pm(\boldsymbol{\omega}\, n)/c_0$. (Where $\epsilon\, \mu = (n/c_0)^2$. Additionally, the boldface $\boldsymbol{\omega}$ is a vector with components $\langle \omega_x, \omega_y, \omega_z \rangle$. The components are the angular frequencies relative to the x, y, and z respectively.) When the expression $\boldsymbol{k} = \pm(\boldsymbol{\omega}\, n)/c_0$ is satisfied, the amplitude $\widetilde{\boldsymbol{E_0}}$ can have any allowed value. Plane waves are the solution to the equation $\boldsymbol{\nabla}^2 \boldsymbol{E} + \epsilon\, \mu\, \frac{\partial^2 \boldsymbol{E}}{\partial t^2} = 0$! These plane waves can be expressed as:

$$A_\omega \exp i[\pm(\boldsymbol{\omega}\, n(\boldsymbol{\omega}))/c_0 \cdot \boldsymbol{x} - \omega\, t + \phi(\boldsymbol{\omega})\,]$$

The amplitude A_ω, phase $\phi(\boldsymbol{\omega})$, and $n(\boldsymbol{\omega})$ are functions of $\boldsymbol{\omega}$. The function $n(\boldsymbol{\omega})$ represents the linear dielectric response to an electromagnetic plane wave with frequency $\boldsymbol{\omega}$. It is alternatively known as the index of refraction. Like it was when ρ and $\boldsymbol{J}$ were nonzero, the most general solution to the sourceless wave equation is the arbitrary summation of plane waves.

$$\boldsymbol{E} = \int A_\omega \ \exp i\left[\frac{c_0}{n(|\boldsymbol{\omega}|)\,\boldsymbol{\omega}} \cdot \boldsymbol{x} - |\boldsymbol{\omega}|\, t + \phi(|\boldsymbol{\omega}|)\right] d\boldsymbol{\omega}$$

2.1.2 *Wave Polarization*

Dipole radiation results when an electric dipole is induced whose dipole moment oscillates sinusoidally with time. This oscillating dipole moment generates light, a propagating electromagnetic wave. This light is radiated in all directions from the location of the induced dipole. The polarization state is aligned with the induced dipole moment. The figure below depicts how dipole radiation gives rise to light with a uniform polarization state.

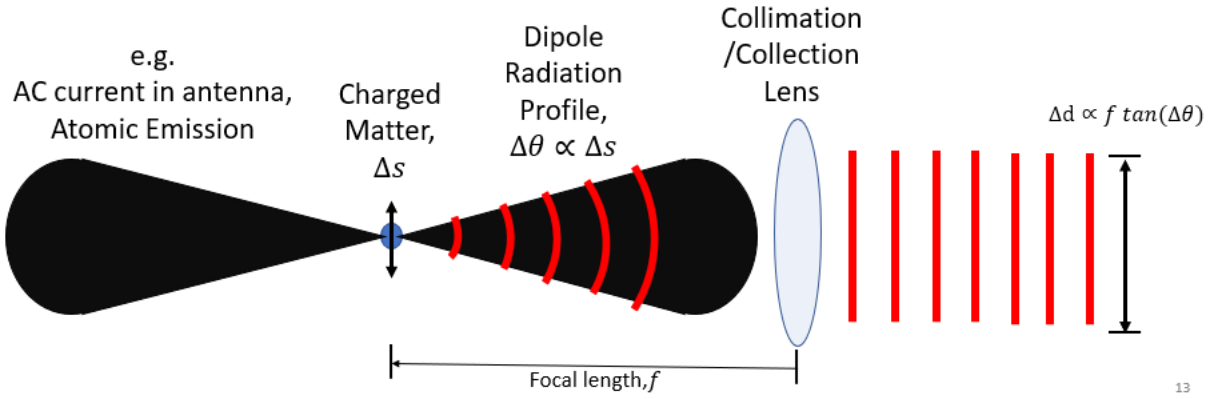

Figure 7 Dipole Radiation profile. The shape and sharpness of the conelike radiation profile is dependent on the details of the shape and size of the sample Δs. The outgoing curved wavefront can be made flat with a lens or curved mirror with the correct focal length f. The light after the lens is a plane wave whose

diameter is determined by the size and collection angle of the lens. The wavefronts of this plane wave will have a uniform polarization aligned with the induced dipole moment of the dipole radiator.

The Maxwell equations admit solutions which are superpositions of plane waves. As an example, consider a plane wave with frequency ω which propagates in the $\boldsymbol{k}$ direction.

$$\boldsymbol{E} = \boldsymbol{E_0} e^{i(\boldsymbol{k}\cdot\boldsymbol{x}-\omega t)}, \qquad \boldsymbol{B} = \boldsymbol{B_0} e^{i(\boldsymbol{k}\cdot\boldsymbol{x}-\omega t)}$$

The $\boldsymbol{E_0}, \boldsymbol{B_0}$ are constant vectors with the respective units of electric and magnetic fields. The "polarization" of a wave is the direction of its electric field. Here, the polarization would be given by $\boldsymbol{E_0}$.

The reason why polarization manifests is because light causes charged particles to emit light with polarization oriented along their direction of motion. The ***Figure 8*** depicts three common polarizations states. The most general polarization is represented by the rightmost beam. Elliptical polarization results from the out-of-phase combination of x and y polarization. It results in the electric field vector tracing an ellipse every period.

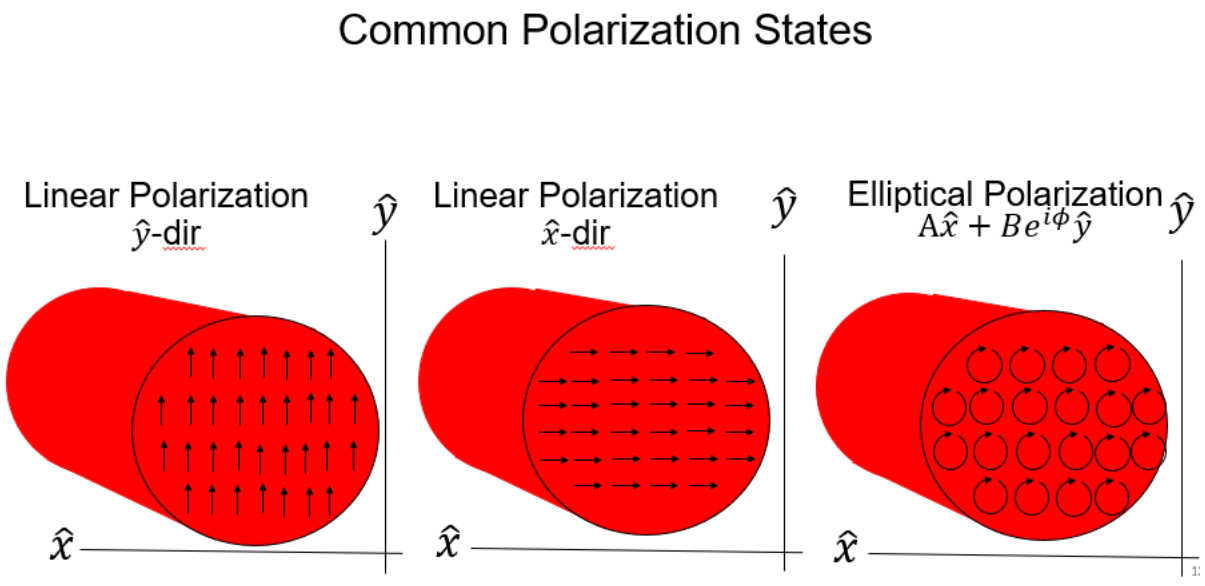

Figure 8 Three common polarization states. The left most is pure vertical polarization. The middle is pure horizontal polarization. The rightmost is elliptical polarization. NOT DEPICTED, left and right circular polarization. This is a special case of elliptical polarization in which $A = B$ and $\phi = \pm\pi/2$.

In the previous section, the Faraday's law was used to derive an expression relating the amplitude of $\boldsymbol{E_0}$ to the amplitude of $\boldsymbol{B_0}$.

$$\nabla \times \boldsymbol{E} = \delta \boldsymbol{B}/\delta t$$

Substituting the above expression for $\boldsymbol{E}$ and $\boldsymbol{B}$ defined above. The following can be found after differentiation and some algebra.

$$\boldsymbol{k} \times \boldsymbol{E_0} = \boldsymbol{B_0}$$

Gauss' Laws for electricity and magnetism in free space ($\rho = 0$) are given by the following:

$$\boldsymbol{\nabla} \cdot \boldsymbol{B} = 0, \qquad \boldsymbol{\nabla} \cdot \boldsymbol{E} = 0$$

By a similar procedure,

$$\boldsymbol{k} \cdot \boldsymbol{B_0} = 0, \quad \boldsymbol{k} \cdot \boldsymbol{E_0} = 0$$

Taking these expressions together, the electric and magnetic fields of a plane wave must be perpendicular to one another. They also cannot point in the direction of propagation.

For an electromagnetic plane wave propagating in the z-direction ($\boldsymbol{k} = k\hat{z}$), the most general expression for $\boldsymbol{E_0}$ is given by:

$$\boldsymbol{E_0} = \left(|\boldsymbol{E_x}|e^{i\boldsymbol{\phi_x}}, |\boldsymbol{E_y}|e^{i\boldsymbol{\phi_y}}, \boldsymbol{0}\right)$$

2.1.3 *Electromagnetic Transport*

One quantity that will be referenced often throughout the paper is something called "flux". The terminology for electrodynamics was coopted from the terms which were first developed for quantifying fluid flow. The flux represents how much fluid or substance is flowing through a given area $\boldsymbol{S}$. This substance can be radiation (photons), water, gas, or particulates. The flux is a way of quantifying a "flow". It is an extensive quantity, which means that it increases along with the size and density of the system. Mathematically, the flux Φ can be expressed by the following expression:

$$\Phi = \iint_S \boldsymbol{A} \cdot d\boldsymbol{S}$$

The integrand, $\boldsymbol{A} \cdot d\boldsymbol{S}$, represents the flux $d\Phi$ through an infinitesimal surface element $d\boldsymbol{S}$. The total flux is the double-integration or sum of all these small elements of flux $d\Phi$. $\boldsymbol{A}$ is some arbitrary vector field. It specifies the magnitude and direction of a vector at each point in space (x, y).

For a uniform vector field at angle θ relative to the normal direction of a rectangular surface $\boldsymbol{S}$, the double integration reduces to a simple dot product $\boldsymbol{A} \cdot \boldsymbol{S} = A\, S \cos\theta$. This special case as well as the more general case of the curved surface is depicted below in the figure.

The change in the state of motion of a distribution of charge is communicated via the emission of waves containing particles called photons. A propagating electromagnetic wave conveys energy from one place to another. It "transports" energy and

information from one place to another. The instantaneous energy density u contained within any electromagnetic field is given by the expression:

$$u = \frac{1}{2}\epsilon\, E^2 + \frac{1}{2\mu}B^2$$

The electromagnetic energy contained within a region of space at one point in time can be found by integration: $E_{tot} \iiint u\, d\boldsymbol{x}$. For an electromagnetic plane wave, the expression for u simplifies further. Faraday's Law $\nabla \times \boldsymbol{E} = -\frac{\partial \boldsymbol{B}}{\partial t}$ suggests the following relationship between E and B:

$$i\, k\, E = i\, \omega\, B \rightarrow E = \frac{\omega}{k}B = \frac{c_0}{n}\, B$$

The magnitude of the excited electric field is stronger than the magnitude of the magnetic field by a factor of c, the phase velocity of the light wave. The expression for the energy density for an incident plane wave then takes the form:

$$u = \frac{1}{2}\epsilon\, E^2 + \frac{1}{2\mu}\left(\frac{E}{c}\right)^2 = \epsilon\, E^2$$

For a flat area $\boldsymbol{S}$ whose normal points parallel to the direction of propagation, the amount of energy per time Δt which passes through that area is given by:

$$E_{tot} = u \cdot volume = \ |\boldsymbol{S}|\, (\epsilon\, E^2)\, (c\, \Delta t) = \frac{(\boldsymbol{E} \times \boldsymbol{B})}{\mu} \cdot \boldsymbol{S}\, \Delta t =$$

The intensity is the energy per time per unit area, $E_{tot}/(|\boldsymbol{S}| \cdot \Delta t)$. The direction of this energy flow is given be $\widehat{\boldsymbol{E}} \times \widehat{\boldsymbol{B}}$. This lends itself to an expression for the incident intensity of an electromagnetic field:

$$I_{inst} = \frac{1}{\mu}(\boldsymbol{E} \times \boldsymbol{B})$$

This represents the instantaneous intensity I_{inst}. It is the energy delivered per area per time. Optical light flips polarity (changes sign) about $10^{14} - 10^{15}$ times per second. This is much faster than the response rate ($\sim 1ns$ or worse) of perhaps the fastest modern electronic detectors. Most detectors instead tend to feel the cycle-averaged intensity of an incident light beam. Since $\int_0^{2\pi} \cos^2 x = \int_0^{2\pi} \sin^2 x = \frac{1}{2}$, the time-averaged intensity I_{avg} is given by:

$$I_{avg} = \frac{1}{2} I_{inst} = \frac{1}{2\mu} (\boldsymbol{E} \times \boldsymbol{B})$$

The figure below depicts the common experimental situation of an outgoing light beam incident on a detector with pixels of size dA. The later chapters refer to the apparent brightness of a beam on a detector as a "flux". This flux will usually be stated as a particular number of "photons" impinging on an area per unit time.

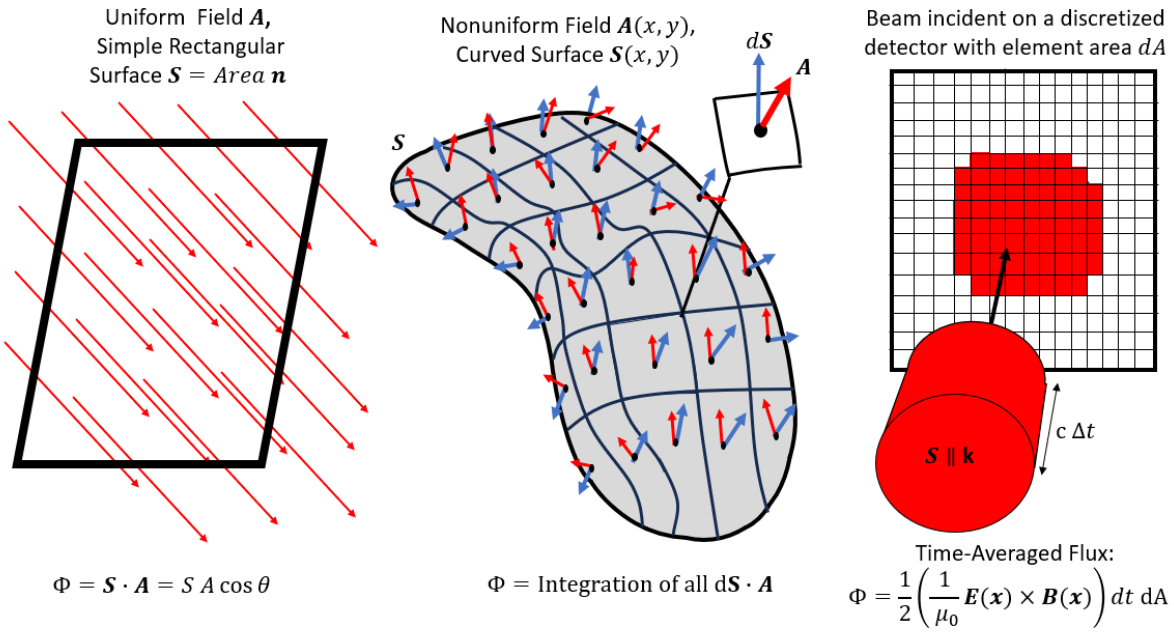

Figure 9 Illustrations of the concept of flux. LEFT depicts the simplest case of a uniform field through a flat rectangular area. MIDDLE is a more general situation of a curved surface and ***non-uniform field.***

Locally, for a very small area of space, the field is uniform and the surface is flat with area $\boldsymbol{dS}$. The total flux is built up from the integration of many tiny flux surfaces. RIGHT depicts a common experimental situation of a light beam incident on a detector.

2.1.4 Nonlinear Optics

The previous analysis used Maxwell's equation to derive a wave equation. This was done by assuming that the polarization field **P** and the magnetic field **H** were directly proportional to **E** and **B** respectively. In general, **P** and **H** can have more complicated "nonlinear" dependencies. For example:

$$\boldsymbol{P} = \epsilon_0 \chi_e^1 \cdot \boldsymbol{E} + \epsilon_0 \chi_e^2 \cdot \boldsymbol{EE} + \epsilon_0 \chi_e^3 \cdot \boldsymbol{EEE} + \epsilon_0 \chi_e^4 \cdot \boldsymbol{EEEE} \ldots$$

In the above equation, χ_e^n is an n-order tensor. The tensor description reflects the fact that the material response will be anisotropic in general. This means that the electric field induced in matter by an applied field might favor certain axes. It also suggests that an applied field along x might induce a field in y and z as well as x.

To some tolerance, many materials are isotropic. The induced electric field is the same regardless of the orientation of the applied field. The induced field also tends to be aligned with the applied field. The tensor χ_e^n can be replaced with a scalar. The total electric field (applied field **E** + induced field **P**) can be written:

$$\frac{\epsilon_0 \boldsymbol{E} + \boldsymbol{P}}{\epsilon_0} = (n_0 |\boldsymbol{E}| + n_1 |\boldsymbol{E}^2| + \cdots) \widehat{\boldsymbol{E}} = n \widehat{\boldsymbol{E}}$$

The expression $n = n_0 |\boldsymbol{E}| + n_1 |\boldsymbol{E}^2| + \cdots$ is the index of refraction. In many materials, the higher order values for n_n get successively smaller (i.e., $n_0 \gg n_1 \gg n_2 \ldots$ and so on and so forth). Hence, for small values of the applied field **E**, $n \cong n_0 \boldsymbol{E}$. This is the regime

of linear optics. The n_0 term is what is colloquially referred to as the "index of refraction." As seen in the previous section, the value n_0 modifies the speed of light in the wave equation, $c_0 \to c_0/\sqrt{n_0}$. In conventional materials and optical wavelengths, n_0 is what gives rise to slower phase velocities in material compared to a vacuum. Practically, this amounts to an experimentally measurable time delay $\frac{\Delta x \sqrt{n_0}}{c_0(\sqrt{n_0}-1)}$ for pulses passing through Δx of material with index n_0 versus an equal amount Δx of air or vacuum ($n_0 \cong 1$).

It is the coefficient n_1 (and higher order $n_{i>1}$) that give rise to so-called "nonlinear `effects". The equation for the electric polarization can be separated as follows:

$$\boldsymbol{P} = \epsilon_0 \chi_e \boldsymbol{E} + \boldsymbol{P}_{NL}$$

In the above expression, $\chi_e = \chi_e^1$. All values of χ_e^n containing $n \geq 2$ get grouped $\boldsymbol{P}_{NL}$. Following a similar procedure to the one carried out in the previous section, a new form of the wave equation can be derived:

$$\boldsymbol{\nabla}^2 \boldsymbol{E} - \frac{c_0}{n_0} \frac{\partial^2 \boldsymbol{E}}{\partial t^2} = \frac{\delta \boldsymbol{P}_{NL}}{\delta t}$$

The derivation assumes that the magnetization (or magnetic polarization) is weak such that $\boldsymbol{M} \cong 0$, then $\boldsymbol{H} = \frac{1}{\mu_0}\boldsymbol{B}$ as before. (This assumption tends to be true for interactions with non-ferromagnetic materials $\boldsymbol{M} \ll \frac{1}{\mu_0}\boldsymbol{B}$.) Additionally, it let $\boldsymbol{J} = \rho = 0$. (The propagating electromagnetic field is far from any free sources of charge.)

In the new "nonlinear" wave equation, the term $\frac{\delta \boldsymbol{P}_{NL}}{\delta t}$ takes the role that $-\boldsymbol{\nabla}\left(\frac{\rho}{\epsilon}\right) - \frac{\partial}{\partial t}(\mu \boldsymbol{J})$ took previously in the last section. Nonlinear polarization acts as a source term.

Let $\mathcal{H}(f) = \nabla^2 f + \frac{1}{v^2}\frac{\delta^2 f}{\delta t^2}$, $\mathcal{H}$ represents the action of the wave equation on the function f. The general solution to the linear wave equation was an arbitrary summation of sines and cosines. Each sinusoidal expression is separable and can independently satisfy the wave equation. In other words, if $E = E_{01}\, e^{i\omega_1 t} + E_{02}\, e^{i\omega_2 t} = E_1 + E_2$, then $\mathcal{H}(E) = \mathcal{H}(E_1) + \mathcal{H}(E_2)$. This is not true for the nonlinear wave equation because of the term $\frac{\delta \boldsymbol{P}_{NL}}{\delta t}$. This is because it contains terms that are higher powers of E. $E^2 = (E_1 + E_2)^2 = (E_1^2 + 2E_1E_2 + E_2^2) \neq E_1^2 + E_2^2$. The higher power E^2 terms have the effect of causing E_1 and E_2 to mix together. There are terms like $2E_1E_2$. If there are two solutions that individually satisfy a nonlinear equation, their summation is not generally also a solution.

To illustrate, let $\boldsymbol{P}_{NL} = n_1 |\boldsymbol{E}|^2$. At one point in space, Let $E = Re(E_1\, e^{i\omega_1 t}) + Re(E_2\, e^{i\omega_2 t})$.

$$|E|^2 = E\, E^* = \frac{1}{4}\left(E_1 e^{i\,\omega_1 t} - E_1 e^{-i\,\omega_1 t} + E_2 e^{i\,\omega_2 t} - E_2 e^{-i\,\omega_2 t}\right)^2$$

$$= \frac{1}{2}\left[\frac{1}{2}(E_1^2 + E_2^2) + \mathrm{Cos}(2\,\omega_1 \mathrm{t}) + \mathrm{Cos}(2\,\omega_2\, t) + \mathrm{Cos}(\omega_1 t + \omega_2 t) + \mathrm{Cos}(\omega_1 t - \omega_2 t)\right]$$

$$\uparrow \quad (Optical\ Rectification) \qquad \uparrow \quad (SHG) \qquad \uparrow \quad (Sum\ Addition) \qquad \uparrow \quad (Sum\ Difference)$$

Applying the trigonometric product-sum identity: $\sin x\, \sin y = \frac{1}{2}[\cos(x-y) - \cos(x+y)]$

2.1.5 Structured Light Source

The electromagnetic force $m\, d\boldsymbol{v}/dt$ on a charged particle with charge q and mass m is given by the expression:

$$m\frac{d\boldsymbol{v}}{dt} = q\boldsymbol{E} + q\boldsymbol{v} \times \boldsymbol{B}$$

Let **E**, **B** be the fields due to an electromagnetic plane wave with period T and wavelength λ travelling in the $\hat{\boldsymbol{z}}$ direction at speed c_0.

$$\boldsymbol{E} = E_0 \cos\left(\frac{2\pi c_0 t}{\lambda}\right)\hat{\boldsymbol{y}} = E\,\hat{\boldsymbol{y}}$$

$$\boldsymbol{B} = \frac{E_0}{c_0}\cos\left(\frac{2\pi c_0 t}{\lambda}\right)\hat{\boldsymbol{x}} = \frac{E}{c_0}\,\hat{\boldsymbol{x}}$$

Inputting these expressions for $\boldsymbol{E}$ and $\boldsymbol{B}$ into the force equation:

$$m\frac{d\boldsymbol{v}}{dt} = qE\hat{\boldsymbol{y}} + q\boldsymbol{v}\times\left(\frac{E}{c_0}\right)\hat{\boldsymbol{x}}$$

$$\frac{d\boldsymbol{v}}{dt} = qE\left[\hat{\boldsymbol{y}} + \left(\frac{\boldsymbol{1}}{\boldsymbol{c_0}}\right)\boldsymbol{v}\times\hat{\boldsymbol{x}}\right]$$

Let $\boldsymbol{v} = \langle 0,\ v_y,\ v_z\rangle$. This means that $\boldsymbol{v}\times\hat{\boldsymbol{x}} = (v_z\hat{\boldsymbol{y}} - v_y\hat{\boldsymbol{z}})$. The equation of motion becomes a system of two differential equations.

$$\dot{v_y} = \left(\frac{qE}{m}\right)\left(1 + \frac{v_z}{c_0}\right)$$

$$\dot{v_z} = \left(\frac{qE}{m}\right)\left(\frac{v_y}{c_0}\right)$$

For the purpose of solving these equations numerically, it is helpful to make each of the variables dimensionless. Since it is difficult to be able to guess how the variables should be redefined. One technique is to write each variable as the multiplication of some dimensionless quantity by a constant with the correct units. Let $v_y = A\tilde{v_y}$, $v_z = B\tilde{v_y}$, and $t = T\tilde{t}$. Then, plug these into the system of differential equations.

$$\dot{v_y} = \frac{d\left(A\tilde{v_y}\right)}{d(T\tilde{t})} = \frac{A}{T}\frac{d\tilde{v_y}}{d\tilde{t}} = \left(\frac{qE}{m}\right)\left[1 + \frac{(B\tilde{v_z})}{c_0}\right]$$

$$\dot{v_z} = \frac{d\left(B\tilde{v_z}\right)}{d(T\tilde{t})} = \frac{B}{T}\frac{d\tilde{v_z}}{d\tilde{t}} = \left(\frac{qE}{m}\right)\left(\frac{A\,\tilde{v_y}}{c_0}\right)$$

If $A = B$, then the equation for v_z becomes:

$$\dot{\tilde{v}}_y = T\left(\frac{qE}{m\,c_0}\right)\tilde{v}_z$$

The quantity $\left(\frac{q\,E_0}{m}\right)$ is the maximum acceleration $\frac{\Delta v}{\Delta t}$ on the particle due to the electric field. It has the units of $[m/s^2]$. The quantity $\left(\frac{q\,E_0}{m\,c_0}\right)$ has units of $[1/s]$. The natural choice for T then is $\left(\frac{m\,c_0}{q\,E_0}\right)$. It represents the amount of time it would take for the velocity of the particle to approach the speed of light c_0.

Inputting the expression for T into the equation for $\dot{v}_y$:

$$\dot{\tilde{v}}_y = \cos\left(2\pi c_0 T\tilde{t}/\lambda\right)\frac{c_0}{A}\left[1 + \frac{(A\tilde{v}_z)}{c_0}\right]$$

The natural choice for A is then equal to c_0. This yields the system of differential equations:

$$\dot{\tilde{v}}_y = \cos\left(2\pi c_0 T\tilde{t}/\lambda\right)\left(1 + \tilde{v}_z\right)$$

$$\dot{\tilde{v}}_z = \cos\left(2\pi c_0 T\tilde{t}/\lambda\right)\tilde{v}_y$$

The period of optical light (λ/c_0) is around $1.33 - 2.64\,fs$. The value for T is only comparable to the period of optical light when $E_0 \sim 10^{12}\,V/m$. For 800nm and 35fs duration light pulses, this would correspond to an incident beam intensity of about $10^{16}\,W/cm^2$. For $T \gg \lambda/c_0$, the cosine would undergo many cycles unless the step size is sufficiently small and basically get averaged to zero.

Using $T = c_0/\lambda$ instead, the system of equations would become:

$$\dot{\tilde{v}}_y = \left(\frac{qE_0}{m\lambda}\right)\cos\left(2\pi\tilde{t}\right)\left(1+\tilde{v}_z\right)$$

$$\dot{\tilde{v}}_z = \left(\frac{qE_0}{m\lambda}\right)\cos\left(2\pi\tilde{t}\right)\tilde{v}_y$$

2.2 Plasmas

2.2.1 Laser Propagation through Plasmas

Consider a plane wave propagating through a plasma. Assuming there are N atoms per unit volume in the neighboring vicinity, the net induced electric field is given by the following expression.

$$\boldsymbol{E}_{net} = -\frac{N\boldsymbol{p}_{net,atom}}{\epsilon_0} = \frac{Ne^2}{3\epsilon_0}\frac{\boldsymbol{E}_0}{m}\sum_i \frac{1}{(\omega_{0i}^2 + \gamma_i i\omega - \omega^2)}$$

This expression is the origin for the electric polarization **P**. It appeared in the derivation for the electromagnetic wave equation. Recall $\boldsymbol{D} = \boldsymbol{P} + \epsilon_0\boldsymbol{E} = \epsilon_0(1+\chi_e)\boldsymbol{E}$. Comparison with that expression suggests that the ϵ in dielectric media is given by:

$$\frac{\epsilon}{\epsilon_0} = 1 + \frac{Ne^2}{\epsilon_0\, m}\sum_i \frac{1}{(\omega_{0i}^2 + \gamma_i i\omega - \omega^2)}$$

In the high-frequency limit ($\omega^2 \gg \omega_{0i}^2 + \gamma_i i\omega$), the expression for the dielectric dispersion simplifies further. $\left(\omega_{0i}^2 + \gamma_i i\omega - \omega^2\right)^{-1} \cong -\omega^{-2}$.

$$\begin{aligned}\frac{\epsilon}{\epsilon_0} &= 1 + \frac{Ne^2}{\epsilon_0 m}\sum_i \frac{1}{\omega^2} \\ &= 1 + \frac{ZNe^2}{\epsilon_0\, m\, \omega^2} \\ &= 1 + \frac{\omega_p^2}{\omega^2}\ \left(where\ \omega_p = \frac{ZNe^2}{\epsilon_0 m}\right)\end{aligned}$$

2.3 High harmonic generation

Laser-Gas High harmonic Generation (Gas HHG) is a technique which produces attosecond duration EUV radiation from intense infrared (IR) laser pulses. Typically, it works by focusing linearly polarized, 30 femtosecond(fs) duration, 800 nanometer(nm) wavelength laser-light from a Ti-Sapphire into a noble-gas such as argon.

The process underlying Gas HHG is fundamentally quantum mechanical. However, a semi-classical description called the "three-step model" is used to conceptualize the physics that takes place[54].

1. The electrostatic potential due to a hydrogen-like atom is given by the following expression.

$$V(r) = -\frac{1}{4\,\pi\,\epsilon_0}\frac{e}{r}$$

At around $10^{14} W/cm^2$ intensities, the electric field of the laser becomes comparable to the electrostatic potential of the atom. The Keldysh parameter is a figure of merit that compares the magnitude of the field of the laser to the binding field of an atom.

$$\gamma_K = \sqrt{I_p/2U_p}$$

I_p is the ionization of the target atom. U_p is the pondermotive energy of the driving fundamental. It represents the cycle averaged energy imparted by the

incident laser field. When γ_K is at or around 1, the field is sufficiently suppressed for electrons to begin tunneling ionizing from their parent atom.

Figure 10 The electrostatic potential felt by the electron in the Figure 10 The intense field of the laser sufficiently distorts the electrostatic potential around the parent atom. The electron tunnel ionizes into the continuum with zero kinetic energy.

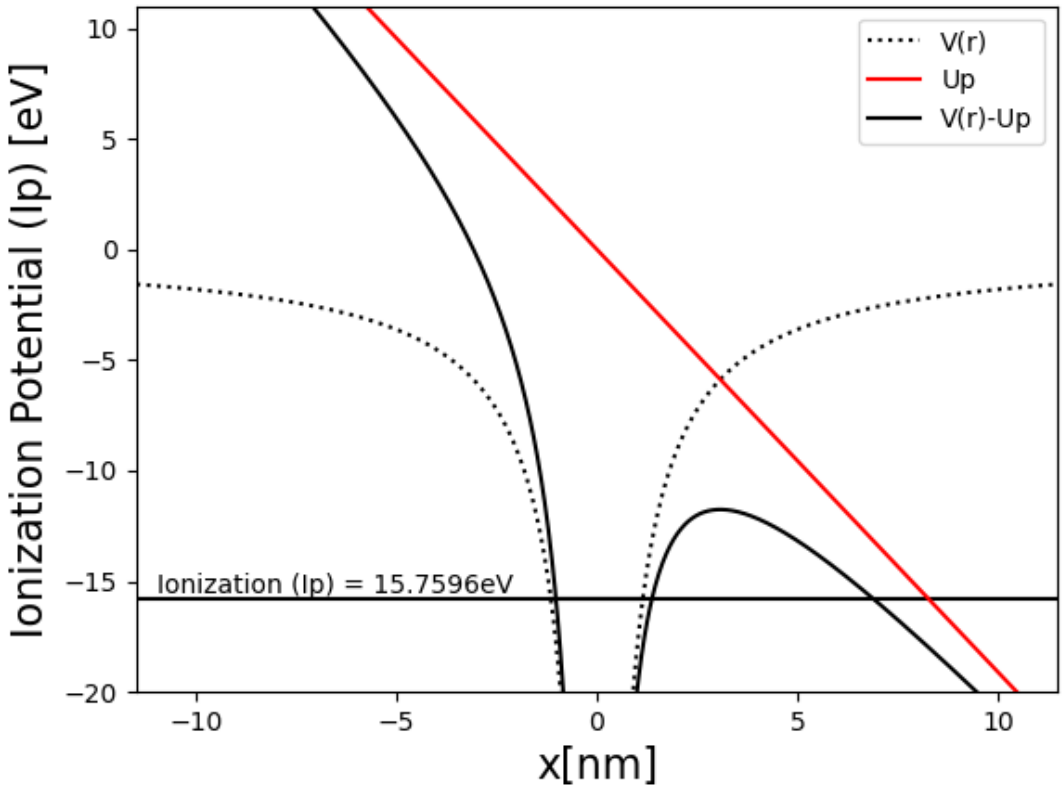

Figure 10 The electrostatic potential felt by the electron in the presence (solid black line) and absence (dotted black line) of the laser potential (solid red line). The ground level energy of the electron is given by 15.8eV. This is the first ionization potential of argon.

2. The newly freed electron begins to accelerate due to the influence of the laser field. It moves away from the atom initially until the beam reverses polarity. After which, it begins to accelerate in the other direction toward the parent atom.

3. The returning electron has a probability of recombining with the parent atom and emitting a photon.

Given the non-relativistic Lorentz force $m\boldsymbol{a} = -e[\boldsymbol{E} + \boldsymbol{v} \times \boldsymbol{B}]$, it was previously shown that the $\boldsymbol{v} \times \boldsymbol{B}$ term is of order v/c. Therefore, it can be neglected if $\boldsymbol{E}$ or $\boldsymbol{B}$ is not strong. Written in this way, the Lorentz Force reduces to the following form.

$$\boldsymbol{a} = d^2x/dt^2 = -(e\ E_0/m_e)\cos\omega t$$

Here, the laser electric field $\boldsymbol{E}$ with frequency ω is given by $E_0 \cos\omega t$. Suppose at time t_b, the electron is born into the continuum. Let $x(t_b) = 0$ and $v(t_b) = 0$ The phase of the field at this time is $\phi_b = \omega t_b$. The equation of motion for the electron can be solved via indefinite integration.

$$v(t) = -(eE_0/m\omega)(\sin\omega t - \sin\phi_b)$$

$$x(t) = (eE_0/m\omega^2)(\cos\omega t - \omega t\sin\phi_b - \cos\phi_b + \phi_b\sin\phi_b)$$

Suppose the electron undergoes a simple there-and-back trajectory. At $t = t_b$, the position of the electron is at the origin $x(t_b) = 0$, near its parent atom. From there, it begins to accelerate under the influence of the laser field. It travels out some distance before turning around. It recombines with the parent atom some later time t_r. The phase of the field at this point is $\phi_r = \omega t_r$.

$$x(t_r) = 0 = (eE_0/m\omega^2)(\cos\phi_r + \phi_r\sin\phi_b - \phi_b\sin\phi_b - \cos\phi_b)$$

$$\cos\phi_r + \phi_r\sin\phi_b = \phi_b\sin\phi_b + \cos\phi_b$$

This equation can be solved numerically to determine ϕ_r as a function of ϕ_b.

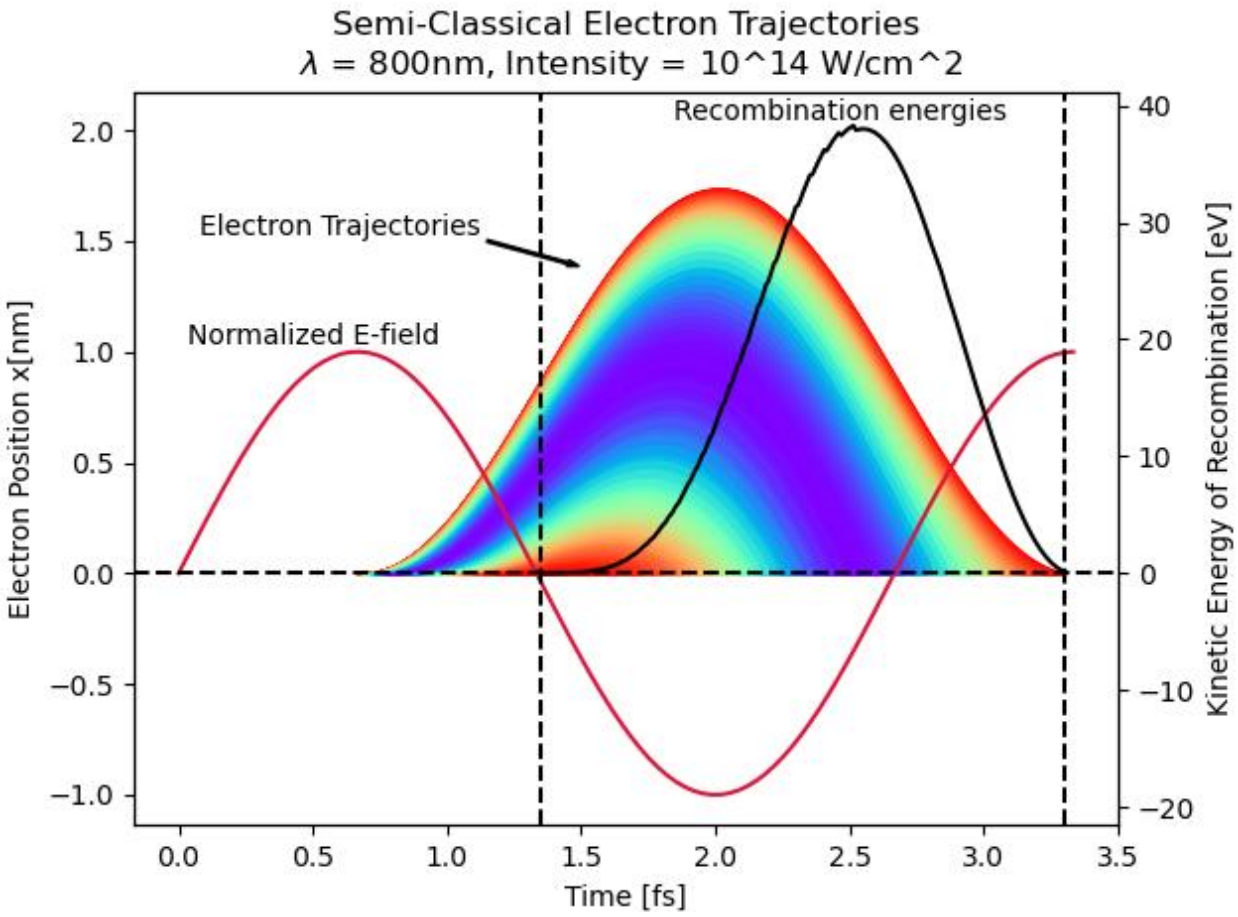

Figure 11 A plot of returning electron trajectories. The color corresponds to the energy of the electron. Redder is lower energy. Bluer/Purple represents higher energy.

Figure 11 depicts the electron trajectories which can recombine with the parent atom. Numerical solutions for ϕ_r only exist for electrons when the electrons are born after the peak of the electric field. If they are born *before* the peak, the electrons never intersect with $x = 0$ again. They instead get pushed further and further away by the $E \times B$ force of the laser field.

Knowing ϕ_r and ϕ_b, the kinetic energy of the electron at recombination can be determined.

$$v(t_r) = v_r = -(eE_0/m\omega)(\sin\phi_r - \sin\phi_b)$$

$$K_{gained} = \frac{1}{2}mv_r^2 = \frac{1}{2}\frac{e^2E_0^2}{m\omega^2}(\sin\phi_r - \sin\phi_b)^2$$

Figure 12 shows the outcome of such a calculation for a field with intensity $I_0 \approx 2 \times 10^{14}\ W/cm^2$. The highest kinetic energy electrons are born a little while *after* the peak with a phase of $\approx +\pi/10$.

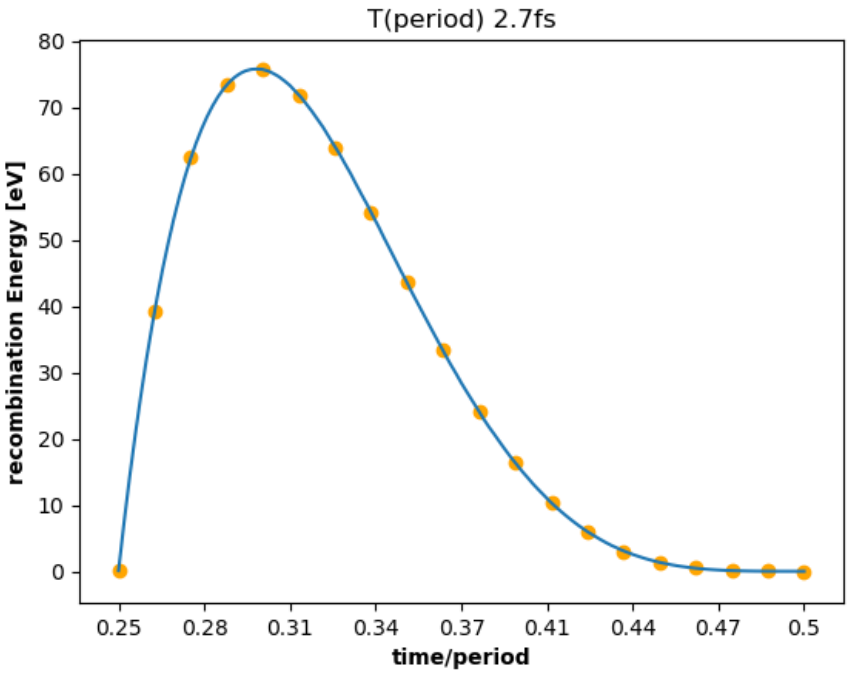

Figure 12 The Kinetic energy of the electron during recombination.

2.4 Phase-matching

Phase-matching is a phenomenon whereby signal from many single-atom emitters builds up longitudinally. It requires the phase of harmonic signal created earlier to cohere and overlap with the signal created later. Figure 13 depicts how the intensity

of the output signal scales with the number of emitters for in-phase and random-phase harmonic emission.

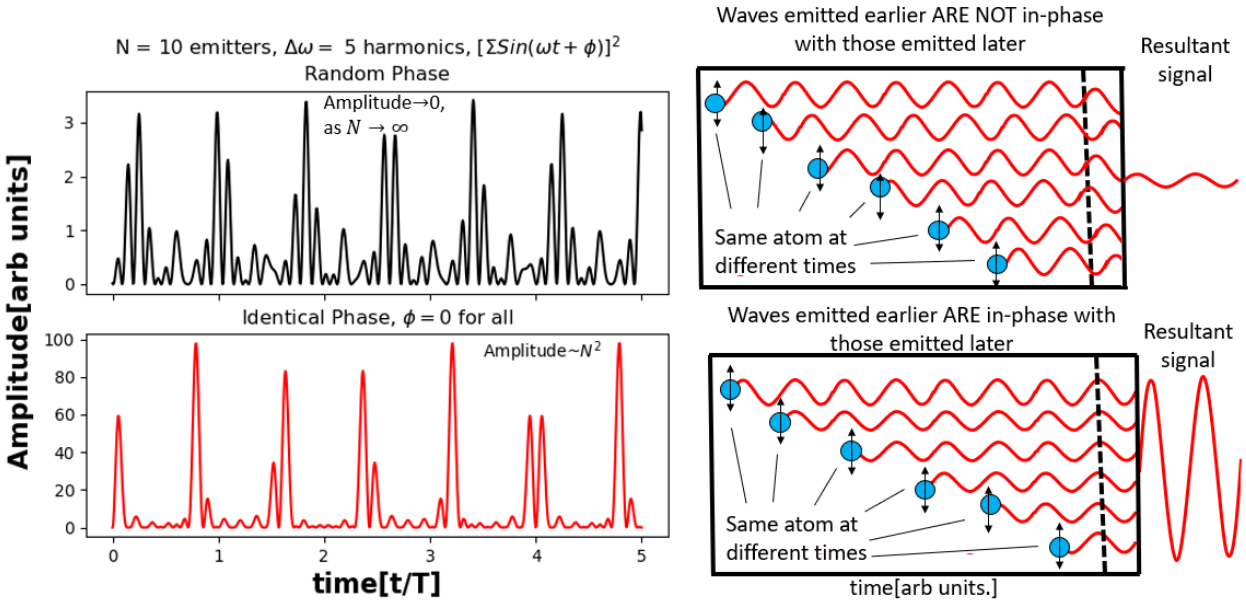

Figure 13 A schematic of how phase-matching works… (TOP-LEFT) Resultant signal intensity from ten emitters with random phase. The signal does NOT scale with the number of emitters N. It instead tends toward zero. (BOTTOM-LEFT) Resultant signal intensity if each emitter has identical phase. The signal intensity grows like the number of emitters squared N^2. (RIGHT-COLUMN) The signal intensity from emitters at different parts throughout the sample is depicted graphically.

The driving fundamental propagates through the plasma and experiences some dispersion k_f. The phase accumulated $\Delta\phi$ by the beam after travelling some distance $v\Delta t$ would be $\Delta\phi = k_f v\Delta t$. At the point of creation, the phase of the harmonics is functionally linked to the phase of the fundamental. They share a "phase relationship". After creation, the harmonics propagate through the sample experiencing some dispersion k_h. If k_f and k_h are different, then the harmonic and

fundamental beams will experience a phase-slip or mismatch over time. The mismatch after some length L through the sample would be $\Delta\phi_{mismatch} = (k_f - k_h)L$.

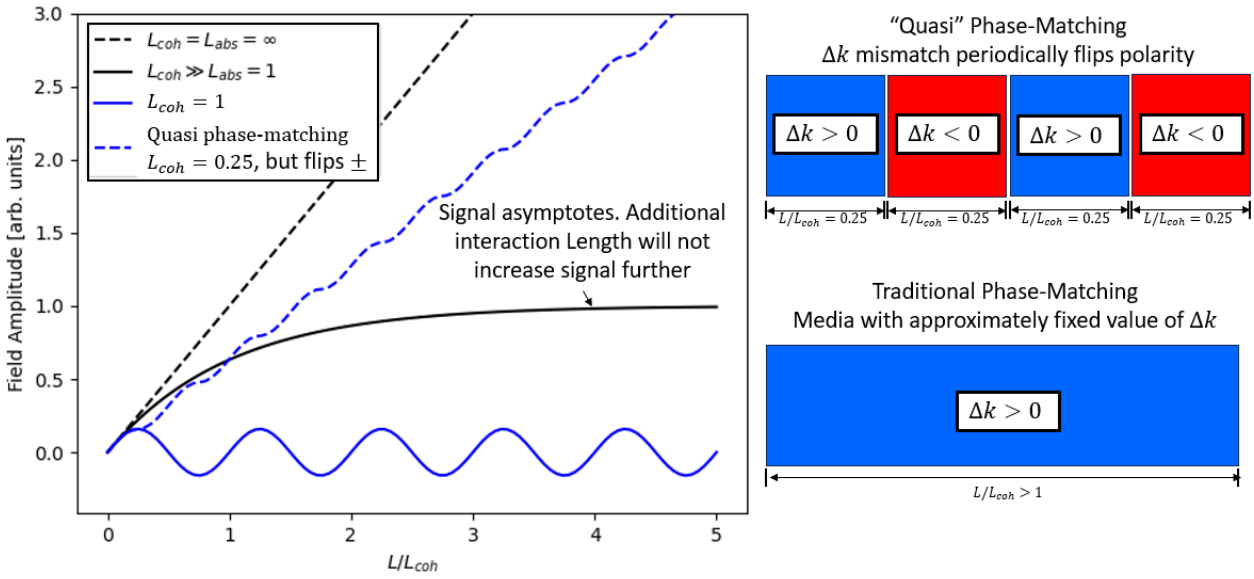

Figure 14 Different Phase-matching regimes. (LEFT-Plot) The solid blue depicts the situation of finite Δk. The dotted blue line depicts quasi phase-matched signal buildup. The solid black depicts phase-matched signal which approached an asymptote due to gas reabsorption. The dotted black line depicts theoretical phase-matching.

The quantity $1/(k_f - k_h)$ has units of length. This length L_{coh} can be thought of as the distance over which the signal intensity can build up constructively. When the size of the target sample L_{med} is much less $\ll$ than L_{coh}, the harmonic signal intensity tends to increase as it propagates from one end of the sample to the other. Traditional phase-matching tunes the experimental parameters such that $\Delta k = (k_f - k_h)$ is minimized and ideally $\cong 0$ throughout the sample.

If coherence were the only effect which determined the final signal intensity, then the harmonic signal could be arbitrarily increased by just continuously making the sample size larger and larger. The harmonic field would increase linearly with L_{med}

(and by-extension the number of emitters N) forever. However, coherence is not the only effect, phase-matched harmonic signal can saturate and asymptote to some maximum value. For gas harmonics, this is generally caused by gas-reabsorption. The target media is not as transparent to the harmonic photons as it is for the infrared-wavelength fundamental. Past a certain characteristic length L_{abs}, the amount of harmonic photons created via Gas HHG equals the number which are absorbed. Figure 14 graphically depicts some of the situations just described.

The equation for Δk can be broken up into a summation of different independent sources of dispersion. The *dominant* contributions to Δk come from the plasma Δk_p and neutral gas dispersion Δk_n. (There are other contributions that will be discussed later.) Assuming $\Delta k \cong \Delta k_p + \Delta k_n$, the equation for phase-matching is given by equation [55, 56]:

$$\Delta k = k_f - k_h \cong \Delta k_p + \Delta k_n = qP(1-\eta)\frac{2\pi\Delta\delta}{\lambda_f} + qP\eta N_a r_e \lambda_f$$

Here, q is the harmonic order. P is the interaction pressure. η is the fractional ionization, a number between 0 and 1. $\Delta\delta$ is the difference in neutral gas dispersion per atmosphere between the fundamental and EUV. r_e is the classical electron radius. λ_f is the wavelength of the fundamental.

Setting $\Delta k = 0$, this equation can be solved for P and η.

$$0 = qP\left[\frac{2\pi\Delta\delta}{\lambda_f} + \eta\left(N_a r_e \lambda_f - \frac{2\pi\Delta\delta}{\lambda_f}\right)\right]$$

Solving for η…

$$\eta_{crit} = \frac{1}{\left(n_a r_e \lambda_f^2 / 2\pi\Delta\delta\right) - 1}$$

There is one value of the ionization fraction which makes Δk equal to zero, regardless of pressure or harmonic order. This value is independent of the value for q or P. This is because q and P immediately factor. Therefore, Δk can be made 0 independent of their values. This value for η is referred to as the critical ionization η_{crit}. Figure ***15*** shows how the coherence length $(1/\Delta k)$ of the 22nd harmonic of an $800nm$ driver varies as a function of η for Argon gas at 0.25 atmospheres.

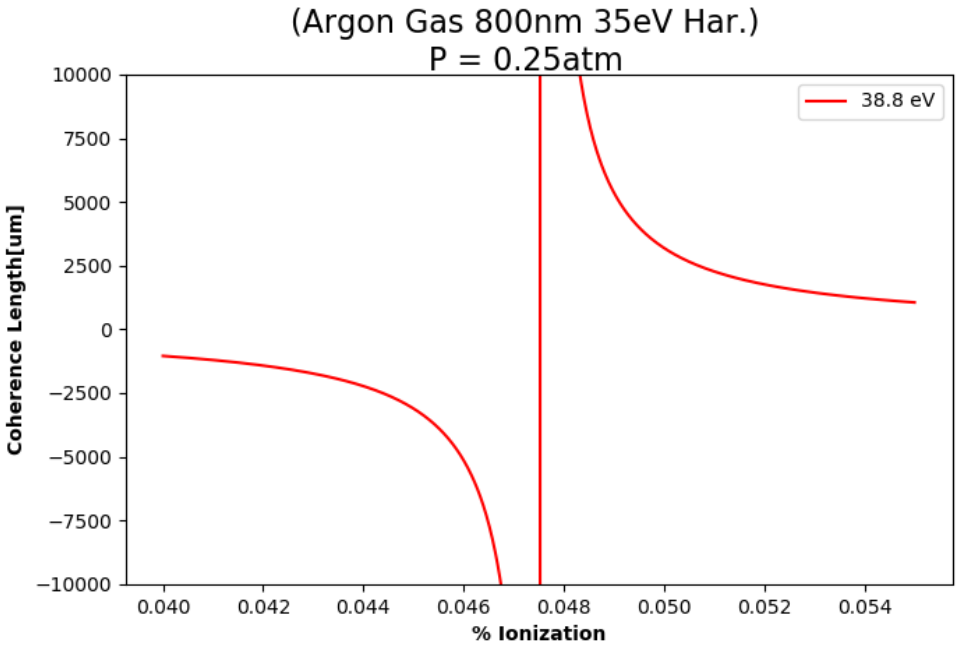

Figure 15 Coherence length as a function of ionization fraction. At about 4.75% ionization, the coherence length approaches infinity.

2.4.1 Geometric Terms

If Δk was *only* equal to $\Delta k_{plasma} + \Delta k_{neutrals}$, it would be possible to phase-match any harmonic (below the single-atom cutoff). It would also be best to use the highest possible pressure because Δk is independent of P at η_{crit} and the signal intensity scales with the number of emitters squared. However, there are other terms which

can be significant in Δk. A more complete expression for Δk is typically represented as follows.

$$\Delta k = \Delta k_{geometry} + \Delta k_{neutrals} + \Delta \mathrm{k}_{\mathrm{plasma}} + \Delta k_{Dipole} \cong 0$$

The term $\Delta k_{geometry}$ represents the geometric phase. It is the phase that a beam experiences due to boundary conditions and its spatial mode. A beam of finite extent is composed of a superposition of plane-waves. This causes the phase ϕ of a beam propagating in the z-direction to not quite be $\phi = k\,z$. Here, "k" represents the magnitude of the k-vector, $k = \sqrt{k_x^2 + k_y^2 + k_z^2}$. For an infinite plane wave propagating in the z-direction, $k = \sqrt{0^2 + 0^2 + k_z^2} = k_z$ However, for a wave of finite extent traveling in the z-direction, this is only approximately true: $\frac{\omega}{c} \cong k_z$.

The next calculations will investigate the case of a TEM_{00} Gaussian mode which focuses on free space. The value of k_z can be calculated from k, k_x, k_y as follows.

$$k_z = k\sqrt{1 - \left(\frac{k_x^2 + k_y^2}{k^2}\right)}$$

In the paraxial approximation, k_x, k_y can thought to be small compared to k_0. To lowest order in (k_x/k) and (k_y/k), the expression of k_z can then be written.

$$k_z \cong k\left[1 - \left(\frac{k_x^2 + k_y^2}{2}\right)\right]$$

Since the beam has a gaussian mode, its representation in Fourier/frequency space will just be another gaussian.

$$FT\left(\frac{1}{\Delta x\sqrt{\pi}} e^{-x/\Delta x^2}\right) \rightarrow \left(\frac{1}{\Delta k\sqrt{\pi}} e^{-k/\Delta k^2}\right)$$

The width of the gaussian in reciprocal space will be different. The relationship between Δx in real-space and Δk in frequency space is given by the uncertainty principle.

$$\Delta k\, \Delta x = 2\pi$$

Based on this expression, Δx and Δk are inversely related. When Δx is small, then Δk is big. When Δx is big, then Δk is small. The beam waist of a TEM_{00} gaussian as a function of z is given by the $w(z) = w_0\sqrt{1-(z/z_r)^2}$. If $\Delta x, \Delta y = w(z)$, then $\Delta k_x, \Delta k_y = (2\pi)/w$ by the uncertainty relation.

Due to the dependence of k_z on k_x and k_y, the uncertainty principle means that k_z will be a spread of possible k_z at and around focus. All these k_z values will all be superimposed together. The phase increase will therefore be due to the average k_z. Or

$\phi = \langle k_z \rangle z$.

$$\langle k_z \rangle = k - \left[\frac{\langle k_x^2 \rangle + \langle k_y^2 \rangle}{2k}\right]$$

The weighted average of k_x and k_y can be calculated as follows. The weight function is just a gaussian normalized to one.

$$\langle k_x^2 \rangle = \langle k_y^2 \rangle = \left(\frac{1}{\Delta k_x \sqrt{\pi}}\right)\int_{-\infty}^{\infty} k_x^2\, e^{-k_x^2/\Delta k_x^2} dk_x = \frac{\Delta k_x^2}{2} = \frac{\pi^2}{2w^2}$$

Plugging back into the k_z gives the following expression for $\langle k_z \rangle$.

$$\langle k_z \rangle = k - \frac{1}{2kw^2} = k - \frac{\lambda \pi^2}{w^2}$$

Since $\phi = kz$ is the phase that one would be expected for a plane wave, he geometric dispersion is given by $\langle k_z \rangle - k = (\lambda\pi^2/w^2)$. This is the "extra" phase that gets added when the beam goes through focus. The total phase is given by integration.

$$\phi_{geometric} = \int \frac{\lambda\pi^2}{w(z)^2} dz = \frac{1}{z_r} \int \frac{1}{1-(z/z_r)^2} dz = \arctan z/z_r$$

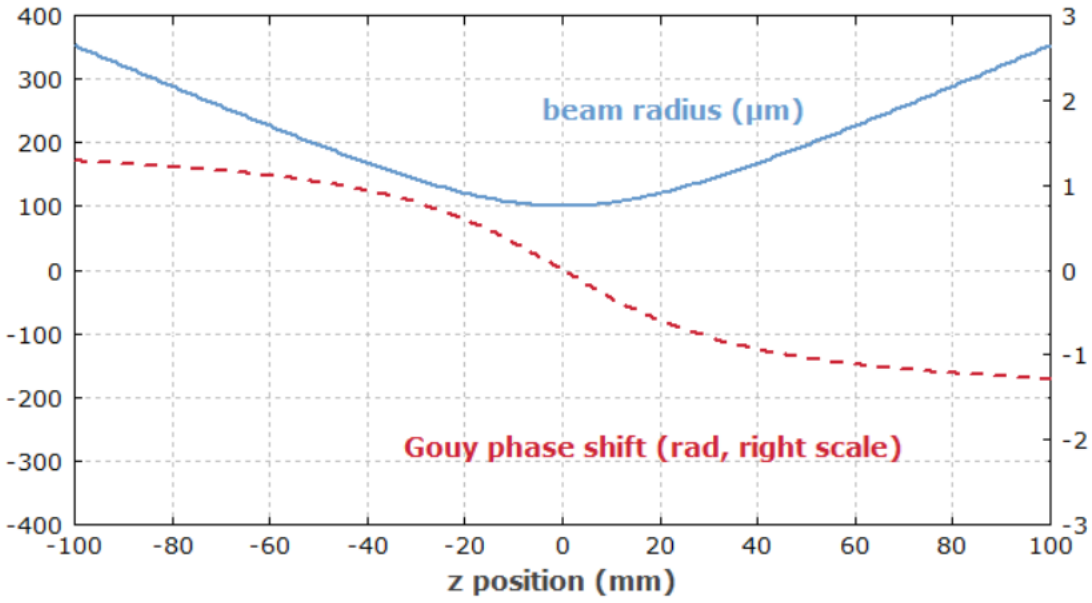

Figure 16 The blue line represents the beam radius. The dashed red line represents the geometric/Guoy phase that gets imparted as the beam goes through focus. Plot reference[57].

$\Delta k_{geometric}$ is due to the difference in geometric dispersion between the fundamental and harmonic frequencies. For a harmonic of order q, the smallest spot radius becomes smaller ($w_0 \to w_0/q$). The Rayleigh length becomes longer ($z_r \to q\, z_r$).

$$\Delta k_{geometric} = k_{f,geometric} - k_{h,geometric} = \frac{1}{z_r[1-(z/z_r)^2]} - \frac{1}{qz_r[1-(z/qz_r)^2]}$$

$\Delta k_{geometric}$ will *always* be positive. For large q, $\Delta k_{geometric} \to k_{f,geometric}$. This term is always positive and is what defines the pressure necessary for phase-matching.

Referring to Figure ***15***, the value of $\Delta k_{plasma} + \Delta k_{neutrals}$ is small and negative just before η_{crit}.

$$\Delta k\, near\, \eta_{crit} = Pressure \times (small\, negative) + (Positive)$$

The closer to η_{crit} the smaller the negative dispersion term but the larger the harmonic order q. The smaller the negative dispersion, the more pressure that is needed to phase-match.

2.5 MIR Gas-HHG

Going to these longer wavelengths produces a higher energy cutoff. For a single atom, the cutoff scales like:

$$h\,\nu_{cutoff} = I_p + 3.17\, U_p$$

$$U_p = \left(\frac{e^2}{8\,\pi^2\, m_e\, c^3}\right) I_L\, \lambda^2$$

$$= 9.33\, I[10^{14}\, W/cm^2]\, \lambda^2$$

I_p is the first ionization potential of the interaction atoms. U_p is something called the pondermotive energy. This term is typically quoted in relation to studies of charged particle acceleration. This is because it has the effect of driving an outward motion of charge (regardless of whether the sign is positive or negative). Here, it is simply used as a figure of merit. It is related to the average kinetic energy imparted to an electron by an electromagnetic field with intensity I_L and wavelength λ. The above equation suggests that the cutoff scales directly with the incident intensity. It is not quite this simple though. To achieve arbitrarily high cutoff energies, one might assume that the intensity I could be continually increased. However, gas-harmonics rely on the incident electromagnetic field not being so intense that it fully suppresses

all bound states. This places a limit on the maximum intensity of the driving field. The binding field felt by a valence or outermost electron can be approximated by a simple electrostatic potential, $E_{bind} = \frac{1}{4\pi\epsilon_0}\frac{Z_{eff}\,e}{r_{eff}^2}$. The effective charge number Z_{eff} can be estimated as $Z-(Z-1)=1$. (This assumes that the $Z-1$ other electrons perfectly screen the attraction due to the Z nuclear protons. In practice, Z_{eff} is likely to be somewhere between 1 and 2.) The effective radius r_{eff} can be estimated as just the radius of the atom. For argon, the experimentally measured radius is about 188pm. The binding field intensity felt by an outer electron in argon is roughly $I_{bind} = \left(\frac{c\,\epsilon_0}{2}\right)\left(E_{bind}^2\right) \cong \left(\frac{c}{8\pi}\right)\left(\frac{e}{(188pm)^2}\right)^2 = 2.2\times10^{14}\,W/cm^2$. The laser cannot exceed the binding energy of the atom. Otherwise, there would be no bound state for the accelerated liberated electron to recombine and emit a photon.

Atom	First Ionization Potential I_p [eV]	Atomic Radius r_{atom} [pm]	Estimated Binding Field Intensity [W/cm^2]	Single Atom Cutoff 400nm [eV]	Single Atom Cutoff 800nm [eV]	Single Atom Cutoff 1300nm [eV]	Single Atom Cutoff 2100nm [eV]
Helium (He)	24.58738	140	7.1×10^{14}	58.21	159.1	379.7	951.4
Neon (Ne)	21.5646	154	4.8×10^{14}	44.3	112.5	261.7	648.1
Argon (Ar)	15.75962	188	2.2×10^{14}	26.18	57.44	125.8	302.9
Krypton (Kr)	13.99961	202	1.7×10^{14}	22.05	46.2	99.04	235.9
Xenon (Xe)	12.1298	216	1.4×10^{14}	18.76	38.65	82.16	194.9

As seen in chapter 4, phase-matched emission produces tremendous orders of magnitude gains in the flux. The phase-matching cutoff, which requires the in-phase

emission of many single atoms, might not necessarily coincide with the single-atom cutoff.

The table suggests a general trend of higher cutoffs pointing toward lighter elements with longer wavelengths. The lighter elements offer two primary advantages. For one, they are more difficult to ionize. The bigger value for I_p figures directly into a higher cutoff based on the single-atom cutoff equation. Secondly, the smaller atomic radius means that the intensity of the binding field felt by the valence electrons is stronger. This means that the incident beam can be more intense without fully suppressing the bound valence states. Like I_p, a bigger value for I_L also ends up figuring directly into a higher cutoff.

2.6 Ionization

The ionization rate can for a physical process can be calculated using the following integral:

$$n_i(t) = (1 - \eta[t]) = 1 - \int_{-\infty}^{t} W[\, I(t)\,]\, dt$$

$n_i(t)$ represents the fraction of some charge state "i" in the media. $n(t) = 0$ would mean that there are no atoms in the media with that charge state. Conversely, $n(t) = 1$ would mean that all the atoms in the media have that charge state. Suppose the media in question contains a single atom, such as argon. Let N be the total number of argon atoms regardless of charge state and $N_0, N_1, N_2, \ldots$ represent the total number with a respective state. For example, N_0 is the number of neutral atoms. N_1 is the

number of atoms with one ionized electron. The fractional density n_i is then given by $n_i(t) = \frac{N_i}{N} = \frac{N_i}{N_0 + N_1 + N_2 + \cdots}$.

Initially, the media is assumed to be neutral. Long before the laser or intense light wave arrives ($t = -\infty$), $n_0(-\infty) = 1$ and $n_{i\neq 0}(-\infty) = 0$. The function W represents the instantaneous rate of ionization $\frac{d\eta}{dt}$. It is a function of the instantaneous intensity of the incident light wave, $I(t)$.

From Wikipedia, the multiphoton tunneling ionization rate is given by[58, 59]:

$$W(t) = \omega_p |C_{n^*}|^2 \left(\frac{4\omega_p}{\omega_t}\right)^{2n^*-1} \exp\left(-\frac{4\omega_p}{w\omega_t}\right)$$

$$\omega_p = I_p/\hbar$$

$$\omega_t = \big(eE(t)\big)/\big(2mI_p\big)^{1/2}$$

$$n^* = Z\big(I_H/I_p\big)^{1/2}$$

$$|C_{n^*}|^2 = 2^{2n^*}[n^*\Gamma(n^*+1)\Gamma(n^*)]^{-1}$$

Here, I_H is the ionization of atomic hydrogen. I_p is the ionization potential of the incident atom. Z is the charge state of the resulting ion after ionization. $\Gamma(x)$ is the Gamma function $\int_0^\infty e^{x-1}e^{-x}dx$. It extends the factorial to complex and real number arguments and is just equal to $(x-1)!$ for integer-valued x[60].

Using the function $W(t)$ for the ionization rate, the ionization fraction can be theoretically determined. Figure ***17*** depicts the result of such a calculation. Every cycle of the laser, the percentage of neutrals decreases while the percentage of electrons and ions grows.

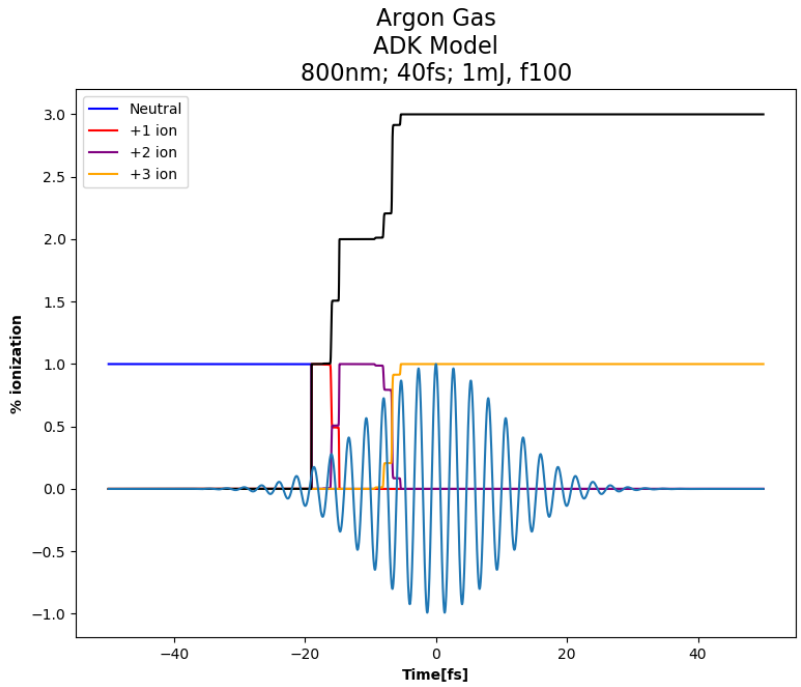

Figure 17 The blue-line represents an incoming gaussian pulse. The dark blue line represents the fraction of neutral atoms. It starts at one, but then this fraction begins to decrease as the pulse approaches. The red, purple, and gold lines represent the ionization fraction of various ion species. The black line represents the electron ionization fraction. For these parameters, the target gas is fully ionized well before the peak intensity arrives. This calculation only includes ion species up to Z=+3.

It is the rate of ionization that determines which harmonics are phase-matchable. Consider Figure 18. Each beam cycle, the ionization fraction increases in a step-like pattern. The low intensity field has a cutoff of only $35eV$, but the ionization fraction builds up more slowly. This allows it to linger near η_{crit} longer and, hence, be coherent phase-matched over more cycles. The length of time or number of cycles over which $\eta \approx \eta_{crit}$ defines the "phase-matching window".

The high intensity field permits a higher cutoff of $75eV$, but it causes the ionization fraction to build up too quickly. In less than one cycle, η jumps from 0 to 25%. This

already greatly exceeds η_{crit}. These higher cutoff harmonics have a very short phase-matching window and the signal will not be able to coherently build up.

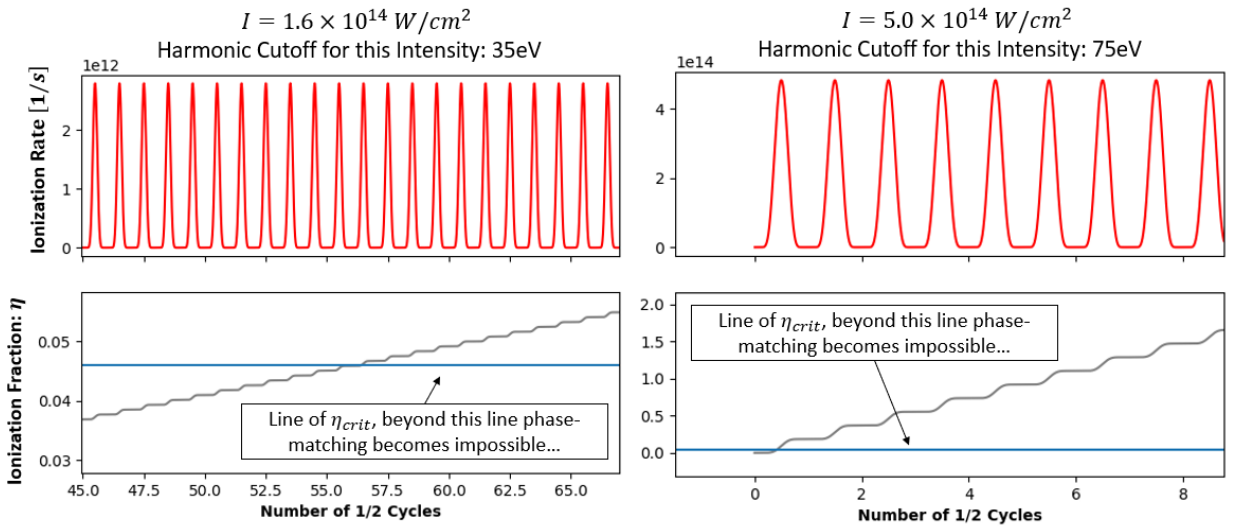

Figure 18 Intense electromagnetic plane wave incident on 800 argon which induces tunnel ionization. The LEFT-side represents the situation for a low intensity driver. The RIGHT-side is the situation for a high intensity driver. The top row shows the ionization rate as a function of time. The bottom row depicts the ionization buildup as a function of time. The horizontal blue line represents η_{crit}. This is the target ionization for phasematched 800nm argon.

2.7 Temporal Characteristics

The periodicity of the gas harmonic generation process results in sub-femtosecond bursts of EUV produced every half-cycle. In time, this signal appears as a series or train of pulses with width $< 1fs$ which are each separated by half a period $T/2$. Figure ***19*** depicts a few examples of such signals. The length of the pulse train or number of bursts is a function of the size of the phase-matching window discussed in relation to Figure 18. When there are many EUV bursts in the train, the spectral width $\Delta\omega$ of the harmonics appear very thin and sharp in a spectrometer. But, as the number of

bursts decreases, the width of the harmonics $\Delta\omega$ becomes wider until finally, for just a single burst, the harmonic spectrum becomes continuous. This is because the spectral width goes roughly like $1/N$.

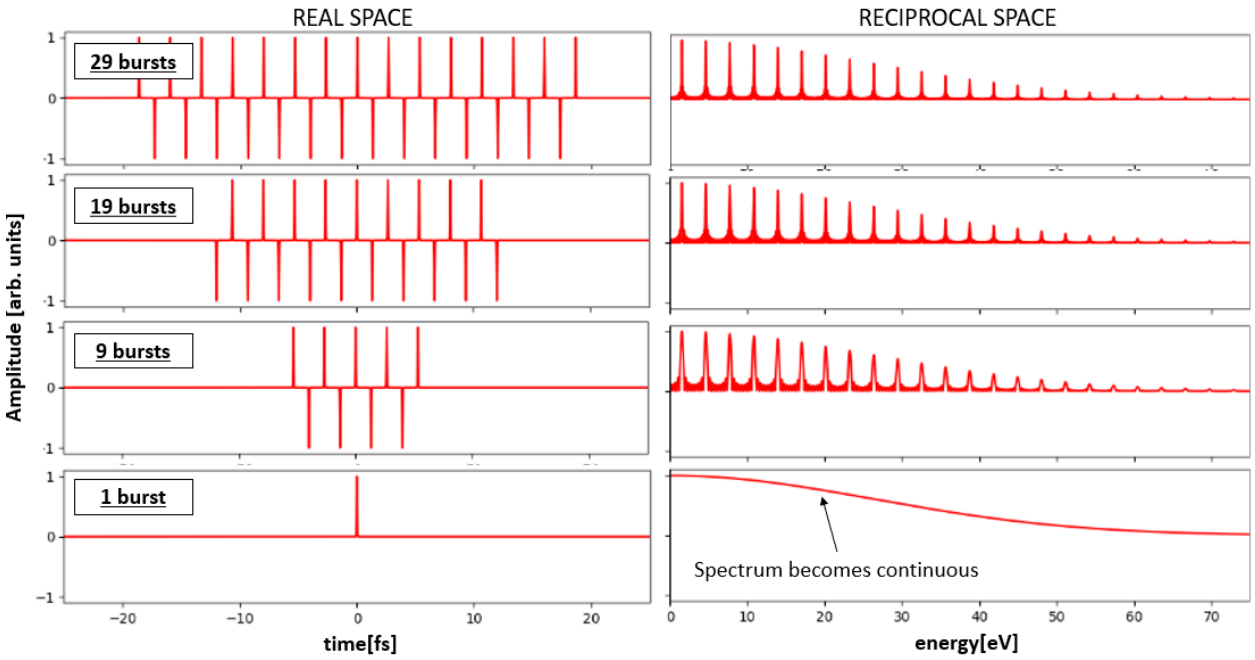

Figure 19 This graphic depicts attosecond pulse trains of different lengths on the left and their associated spectrums on the right. From the top row to the bottom row, the number of EUV bursts decreased. The bottommost row shows the situation for just one burst.

Figure 20 depicts simulated single atom spectra. One spectrum takes on the characteristic appearance of "single atom" emission. That is, a long relatively constant intensity plateau which sharply cuts off at some value. The other spectrum takes the characteristic appearance of a "phase-matched" signal. The Fourier Transform of each spectrum is shown on the righthand side. These should be the appearances of the two harmonic spectra in real space. The calculation assumes that each of the frequency components are in-phase and Fourier Transform Limited (FTL). Each of the signals in real space contain about 7 "bursts" of radiation. This is because

the number of bursts is a function of the harmonic width which was assumed to be the same for both spectra and every harmonic. The bursts of the FTL for single atom are much thinner, essentially point-like. This is because the single-atom is broader band and contains more frequency components. On the other hand, the FTL for phase-matched has bursts with much wider envelopes. The carrier frequency of about $45eV$ is also visible under the envelope.

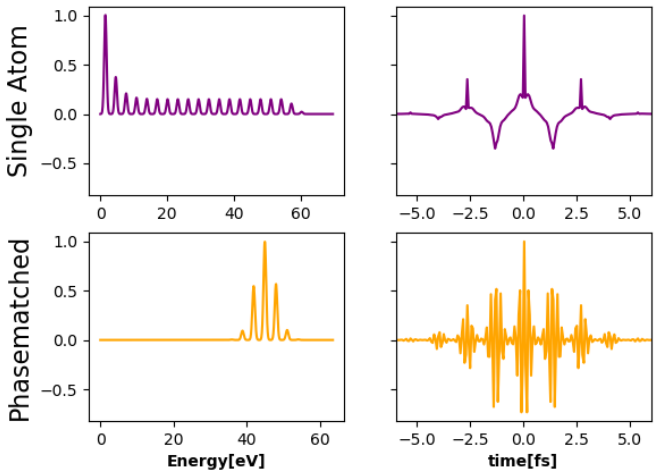

Figure 20 The left-side of the figure simulates the qualitative appearance of "single-atom" and "phase-matched" spectra. Both spectra are normalized to a peak value of "1" in arbitrary intensity units. The right-side shows the FTL of each spectrum.

Real spectra usually do not have the "single-atom" emission and the "phase-matched" spectra separated. If the signal is phase-matched, then the two will be simultaneously present in the data. However, because of the difference in magnitudes, it might appear that there is only "phase-matched" when there is really both. Phase-matching can be $10^3 - 10^6$ times brighter. Additionally, depending on the signal-to-noise and the noise floor of the detector, it might not be possible to observe

"single-atom". The only signal that "rises above the noise" is that which is at-least *weakly* phase-matched.

Figure 21 shows a data measurement of a phase-matched gas-harmonic spectrum and its corresponding FTL. Because the gas-harmonics are well-phasematched, they have a very narrow $\Delta\omega$ width and there are many bursts in the real-space signal. The input beam was $800nm$ argon with $35fs$ pulse duration. In the FTL, each of the peaks is separated by roughly $1.3fs$ which is what would be expected for a burst of EUV radiation every half-cycle. The temporal width Δt $(1/e^2)$ of one burst/peak is just $344as$! This number was found by taking the Fourier Transform of the gaussian-shaped envelope bounding the harmonics, rather than the data itself. (The FTL of the harmonic envelope is what the real-space signal would look like if the spectra were continuous. It would just be a single burst.)

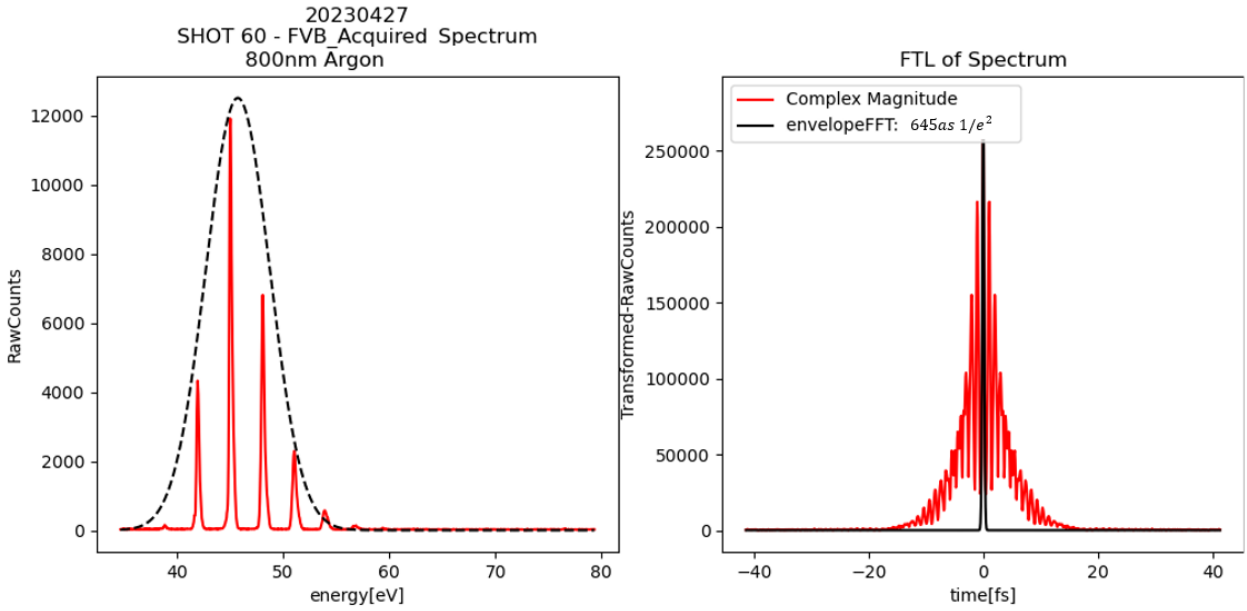

Figure 21 LEFT is an actual gas-harmonic spectrum measurement. RIGHT depicts this spectrum's FTL. The red-line represents intensity as a function of time. The black line represents the envelope of just one single EUV burst.

The FTL of the spectrum assumes that each of the frequencies has the same phase. This means that each of the frequencies automatically make the shortest pulse when superimposed together. However, due to the nature of the gas-harmonic generation process, each harmonic will have a different phase which is related to its energy and how long it spends tunnel-ionized. The wavelength of an electron is given by the De Broglie relation:

$$\lambda = \frac{h}{mv} = \frac{h}{\sqrt{2mE}}$$

Here, h is the Plank Constant. λ is the wavelength of the electron. m_e is the mass of the electron. E is the energy of the electron.

The phase of the electron will be $\phi = \lambda(t)\, x(t)$. (There is a time-dependence on λ because the electrons are accelerated by the laser-field.) Electrons which take longer trajectories will gain more phase than electrons that take shorter trajectories. They will also be accelerated to higher instantaneous velocities, which will result in shorter have wavelengths and hence bigger overall phases. Figure ***22*** estimates the semiclassical phase for the parameters of the data in Figure 21.

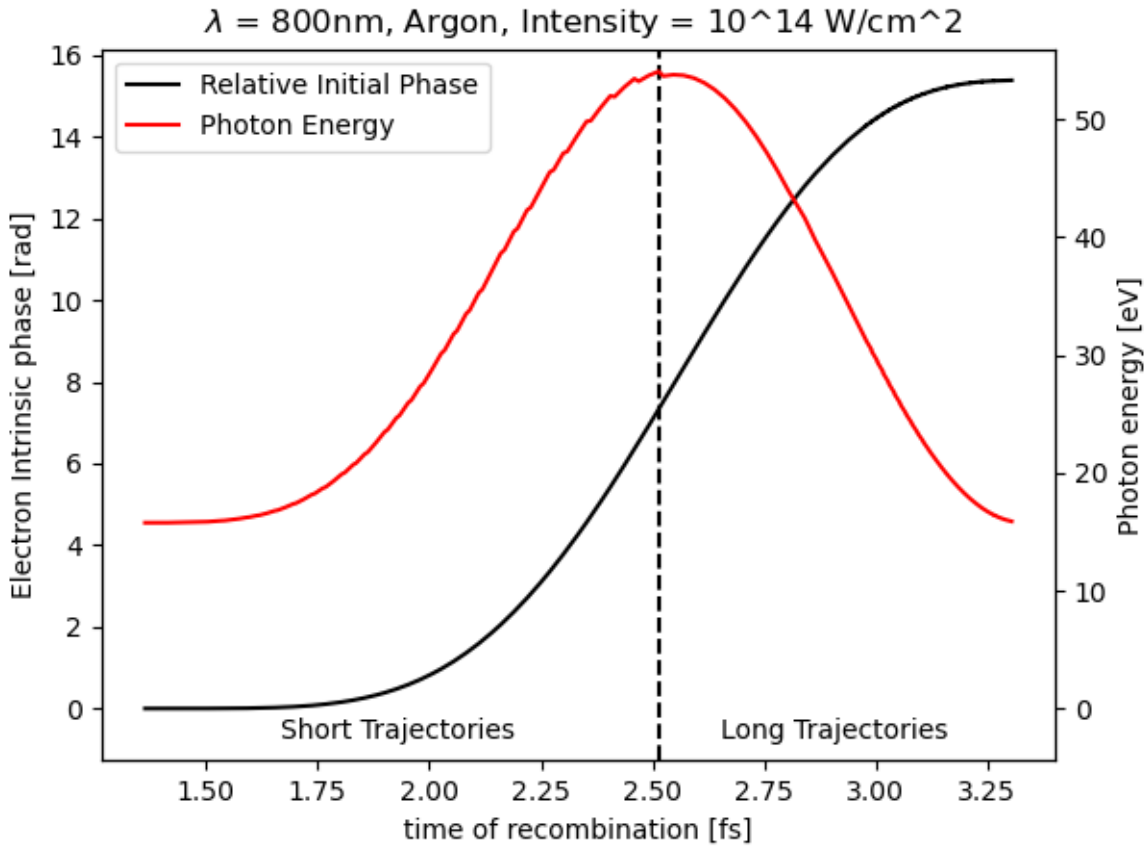

Figure 22 This figure relates the phase and energy of the electron to its time of recombination. It assumes an incident $\boldsymbol{800nm}$ plane wave with an intensity of $\boldsymbol{I = 10^{14} W/cm^2}$. The photons produced by this field should align well with the energies shown in the data harmonic spectrum.

In Figure 23, the phase calculated for the "short trajectories" of Figure 22 is applied to the Fourier transform of harmonic data's envelope. On the right side, the black curve represents the FTL (Fourier transform limit). This is the Fourier Transform also calculated in Figure 21 that assumes zero phase. (All spectral components sum constructively in time.) The red curve represents the Fourier transform with the calculated phase added to it. It can be seen that the spectral components added in this way come out with a longer pulse duration of $888as$ versus $645as$.

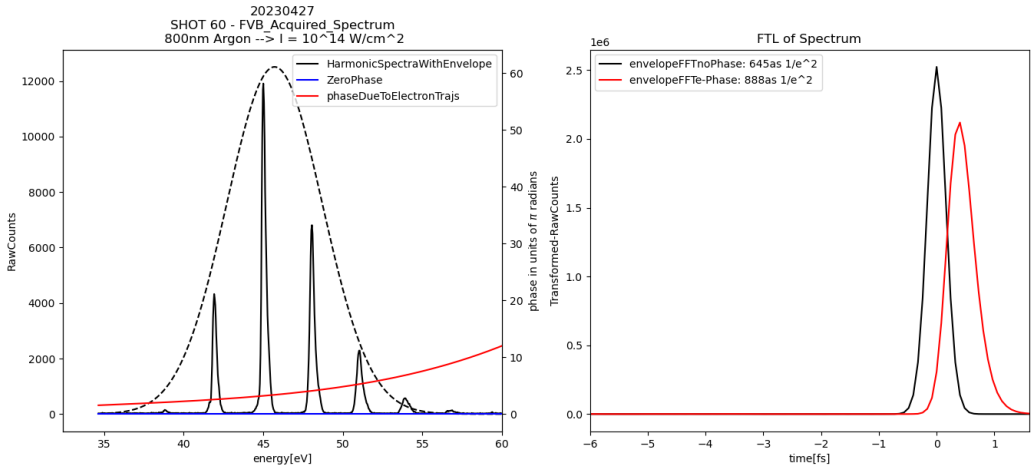

Figure 23 The left side shows the spectrum from Figure 21. The right side shows the Fourier transformation of this spectrum for two different spectral phases.

Chapter 3

Methods

3.1 Lasers

3.1.1 Solstice Laser

The Plasma Physics Research Group at UC Irvine houses a commercially available Ti: Sapphire laser system (Spectra-Physics Solstice ACE). The entire laser system, encapsulating the mode-locking and chirped pulse amplification system, was housed in a single box. To deliver the beam from place to place, the intensity had to be regulated to ensure a linear response. Typically, the laser was operated at one 7th of its maximum energy of $7mm$ with a diameter of $12mm$. At these conditions, the B-Integral value was low—much less than one.

When the laser arrived at the target, it was focused to intensities from $10^{14-18}\ W/cm^2$.

The laser had an M2 value of about 1.1 (See Figure 24).

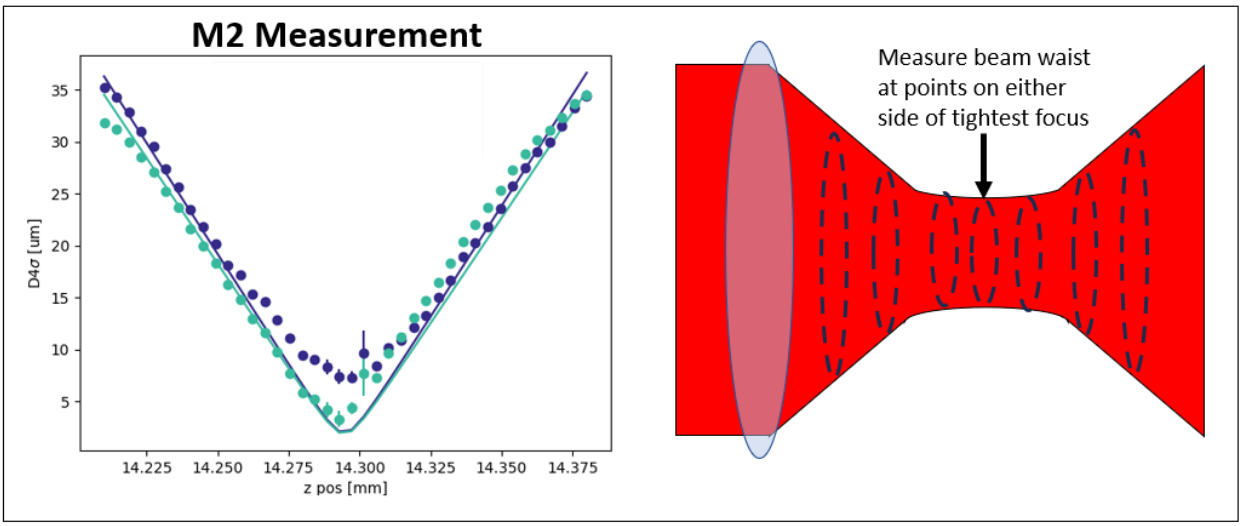

Figure ***24*** LEFT. Typical M2 measurements for our laser system. RIGHT A schematic diagram of how an M2 is performed. It essentially involves measuring the beam waist at multiple points as it goes through focus.

The physical jitter was measured to be $\frac{3.5um}{30} \cong 0.1um$, smaller than the Rayleigh length of even the highest intensity experiments (See Figure 25).

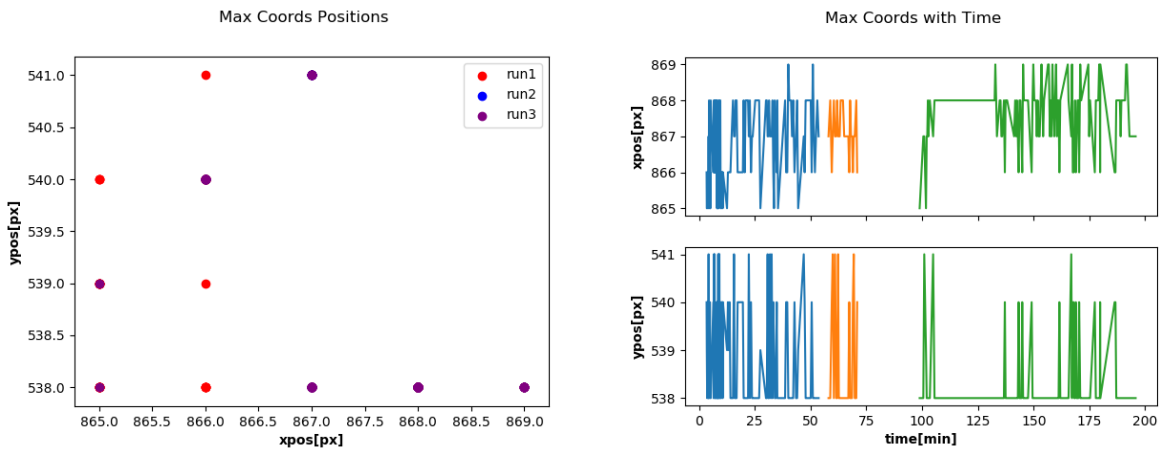

Figure ***25*** LEFT depicts the position of the max-coords of a focal spot as a function of position. These show where the beam would shift over a 3-hr long experiment. RIGHT shows the x and y positions as a function of time. The jitter seems more consistent with random detector noise than anything inherent to the beam itself.

The temporal characteristics of our beam were characterized using second harmonic generation frequency resolved optical gating (SHG-FROG). We used a homebuilt FROG, as shown in Figure 26. The laser had a motorized compressor enabling the laser chirp to be controlled by computer. FROG measurements of the laser chirp are shown in Figure 27.

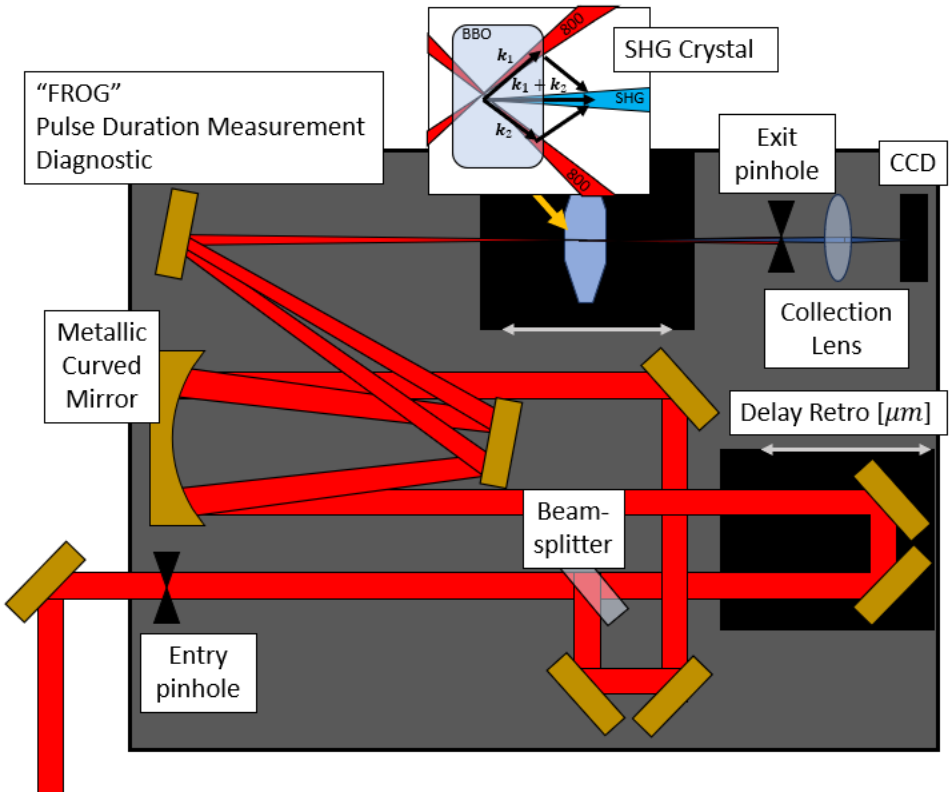

Figure ***26*** A schematic diagram of the FROG used in the UCI lab.

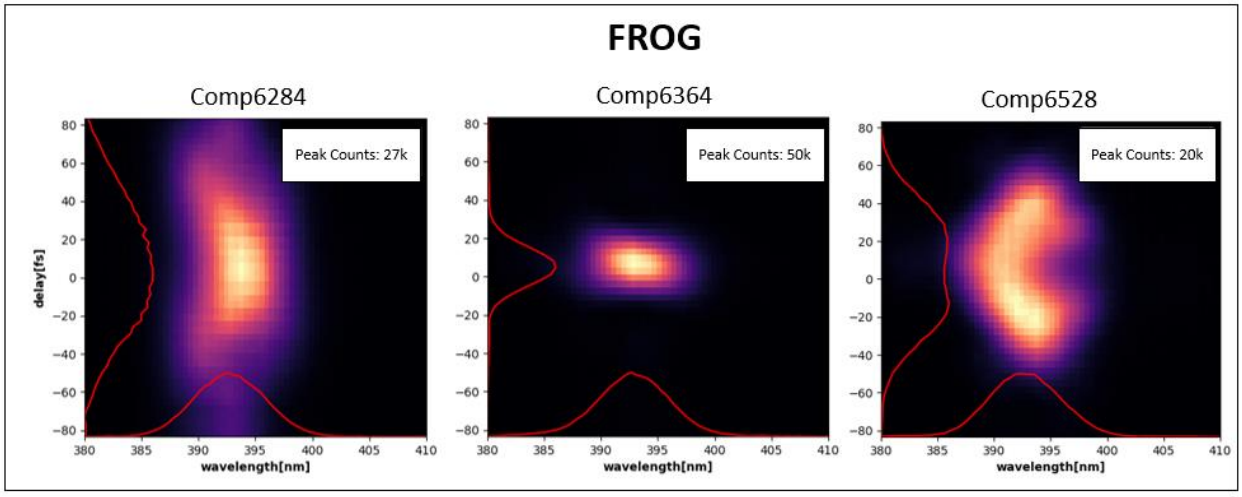

Figure ***27*** A set of FROG traces showing how the beam differs for different positions of the compressive gratings inside the laser box. It can be seen in the leftmost and rightmost traces that the width of the pulse elongates and becomes less symmetric as the beam is moved. At the best compressor spacing, the beam trace is narrowest.

3.1.2 Mid-Infrared Light Conversion

Access to longer wavelengths was attainable via the SpectraPhysics "Topas-Prime" optical parametric amplifier (OPA). See Figure 28 for a schematic of the system. A higher frequency "pump" beam and a lower frequency "signal" beam enter a transparent material with sufficient nonlinear index. The nonlinear beating of these two frequencies amplifies the signal beam while drawing energy from the pump beam.

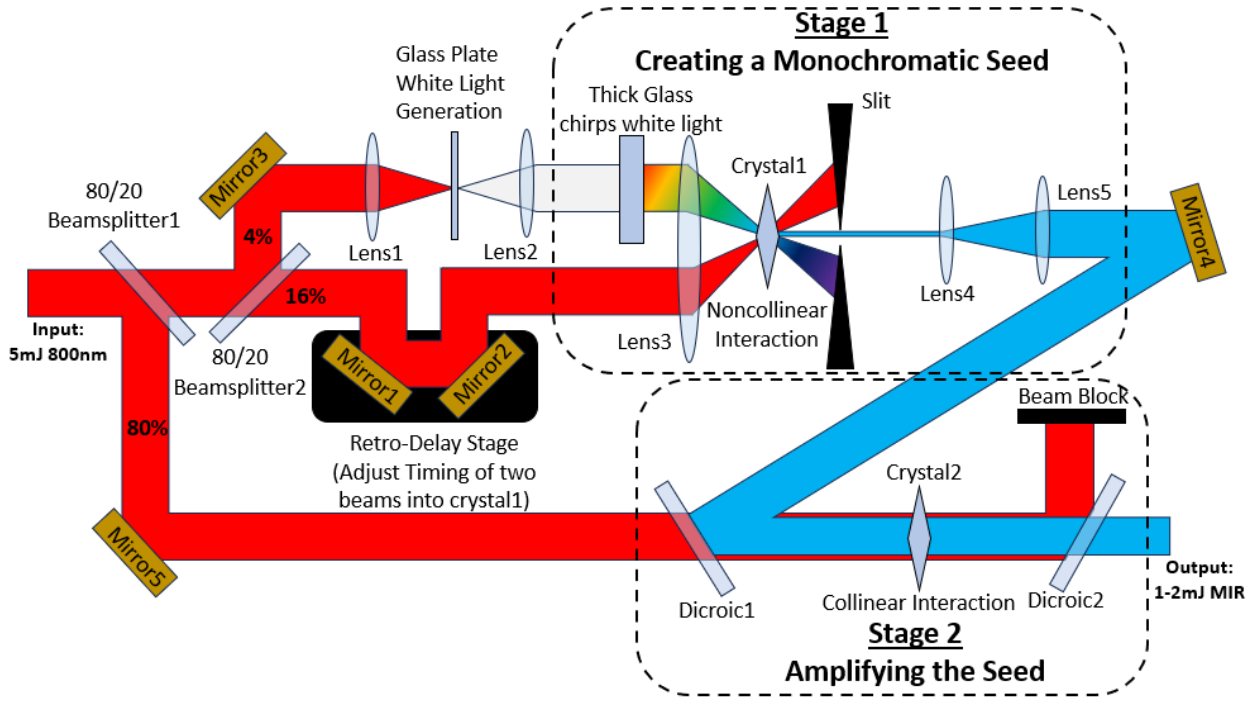

Figure ***28*** Schematic of the OPA. This is a simplified model that intends to accentuate the two key processes that generate the resulting MIR.

The beam going into the OPA is a $5mJ$ beam with 800nm central wavelength. The wavelength bandwidth of this input light source is about $800nm \pm 20nm$. The OPA pump is an 80% reflection split from the original 5mJ input beam. This beam has roughly $4mj$. The 20% portion of the beam containing roughly $1mj$ is used for "white light generation" (i.e., light of many colors that span the optical band, but also the MIR 1100-1500). The other arm is just left as $0.8mJ$ of $800nm$. These two beams are each focused into a nonlinear crystal. This process tends to be optimally efficient around $1250 - 1300nm$ so that is what is typically used.

The result is about $1mJ$ of $1300nm$ "signal", a little less than $1mJ$ in an "idler" 2100nm beam, and a residual $2 - 3mJ$ in the 800nm "pump". These three beams are separated using dichroic mirrors placed immediately after the "Topas Prime" box. If it doesn't

need to be used elsewhere, the pump is usually thrown away into a beam dump. The other two beams are used to drive MIR HHG experiments.

3.2 Target

For a freely flowing gas, controls might be needed to check that the density and pressure remain constant—even as the intake pressure from the tank continues to slowly dissipate. If this gas is not pumped from the room or the chamber, the ambient background pressure will change the material conditions of the environment.

Additionally, the gas-harmonics needed to be generated in a vacuum. The reason was at least twofold: One, the beam focusing in air is intense enough to generate plasma well before it achieves tightest focus or interacts with the target. This interaction before focus would lead to nonlinearities in the beam and even instabilities like beam breakup [61, 62]. Secondly, the EUV light generated in the interaction would be heavily absorbed by air at densities of 1atm. According to the x-ray database CRXO[63], the transmission of a 10-60eV beam traveling through 1m of nitrogen at even 1Torr would be 10^{-12}. The vacuum system achieved chamber pressures of 3×10^{-5} Torr when there was no load from the gas-targets. When the target was flowing gas though, the ambient pressures in the chamber could rise to as high as 1 to 10mTorr. This still offered EUV transmission of >70%.

A common target is the free-flowing capillary, or gas jet. In the experiments presented, the gas jet was cut from 1/16" diameter PEEK tubing which had a 250μm orifice diameter. It was mounted using 1/16" compression fittings. And continuously flowed gas into the vacuum chamber. With sufficient backing pressure, high densities are achievable, though the spatial extent is limited as shown in Figure 29.

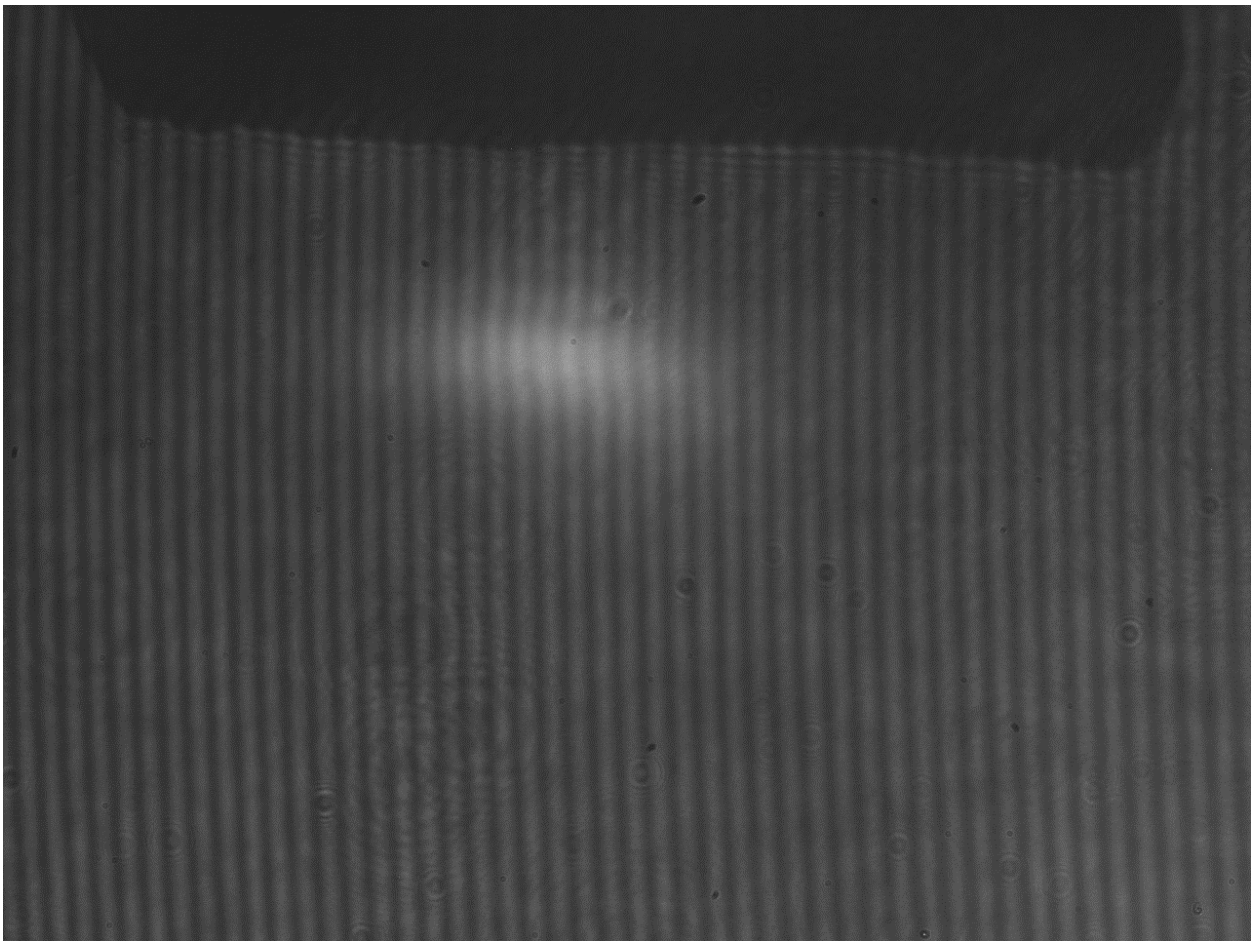

Figure ***29*** Mach-Zehnder Interferometry of the plasma produced by a gas capillary backed with 408PSI of Argon (Ar). The density of the gas and the plasma can be determined by comparing the degree of fringe deflection relative to the control image.

3.2.1 3D-printed Laser-Gas Targets

A second target system was employed utilizing 3D printing. A Stratasys Objet printer with a theoretical minimum print resolution of about 15microns was used to fabricate these targets. These used a high-density "VeroClear" plastic.

Figure 29 LEFT the Stratasys printer. RIGHT the resolution targets used to experimentally assess the accuracy of the printing and the thoroughness of the cleaning methods.

Figure 30 shows a picture of some of our optimized designs. We ended up favoring designs in which the diameter tapered smoothly and linearly to some desired experimental diameter. The laser entered and exited the target through two orifices on either side of the target. These were chosen to be as small as possible without creating interference or clipping the beam. From our tests using the 3d-printed "calibration slide", the smallest holes that could be repeatably produced had diameters of about 100um. We tended to prefer orifices of about 250 to 500um. These tended to be both easier to clean and align. The key highlight, though, of these 3d-printed targets was the region between the two orifices. This was a region of homogenous pressure that scaled well with the backing pressure. The size and dimension of this region could be scaled as desired. We also found that adding some empty or dead volume above the area through which the laser propagates further improved the density homogeneity.

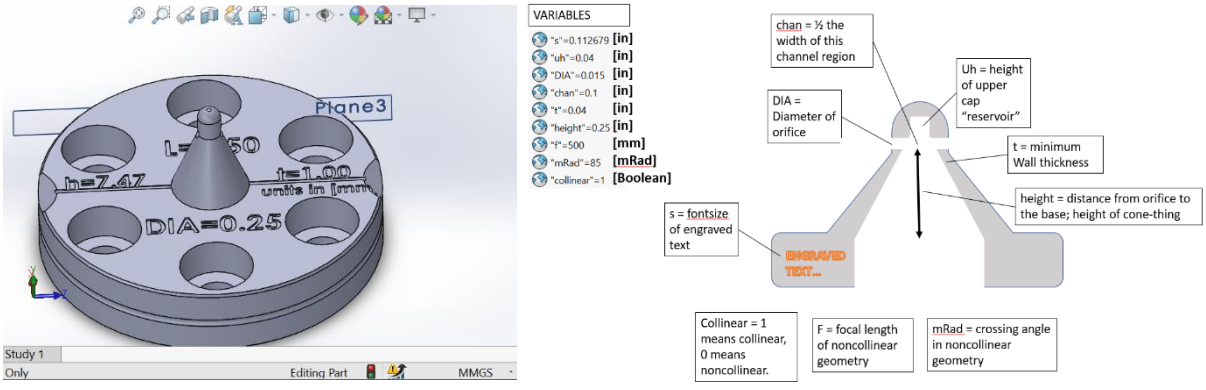

Figure 30 LEFT The 3d CAD model of one our optimized gas cell designs. RIGHT A schematic depiction of the Gas cell breaking down and how it looks internally.

3.2.2 *Flow Modeling*

To determine nominal density profiles of the targets, computational fluid dynamic (CFD) modeling of the targets was carried out using SolidWorks Flow Simulation. We benchmarked its accuracy using some simple situations. Figure 31 shows the pressure and flow speed for a simple pipe bent at 45 degrees. Theoretically, there is an expected drop in the initial and final pressures. The CFD model agreed for this simple situation.

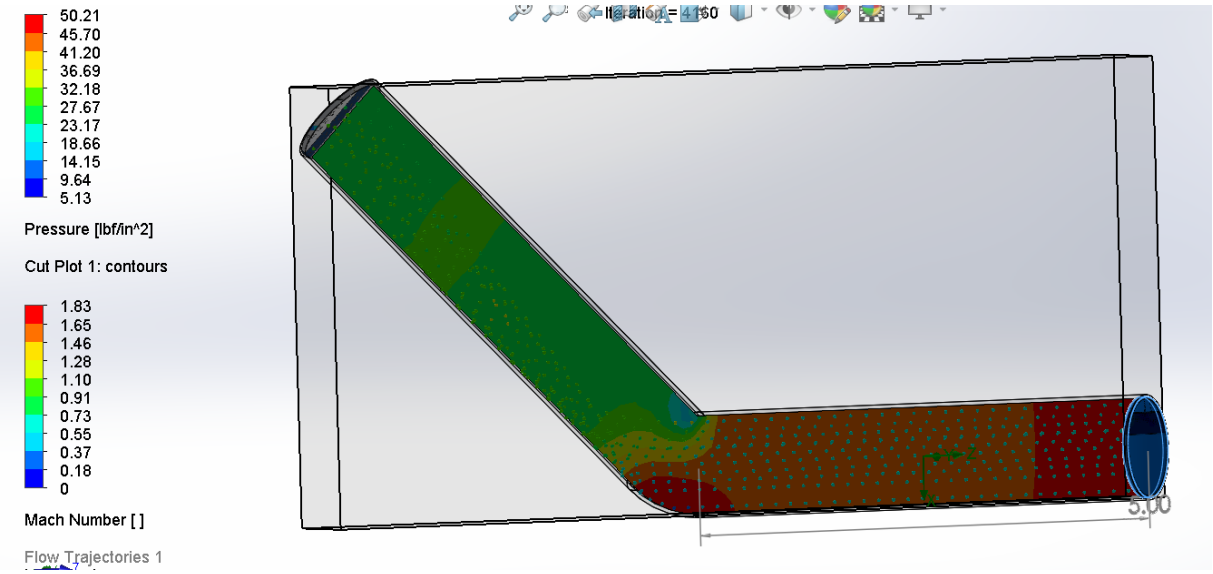

Figure 31 The change in pressure and fluid velocity due to a 45deg bend in an otherwise straight pipe.

3.3 EUV Spectroscopy

3.3.1 *Detection Equipment*

The two different models of x-ray cameras used were manufactured by Oxford instruments. One was the I-Kon M and the other, which had a spectroscopic chip, was the Newton. Both detectors were made of silicon. Figure 32 shows the response of the chip as a function of energy. It depicts how many photons of a particular wavelength it takes to trigger a response on the detector. A quantum efficiency (QE) at or near one means that every photon will trigger a detectable response. A QE of zero means that no amount of photons incident on a camera will trigger an electronic response.

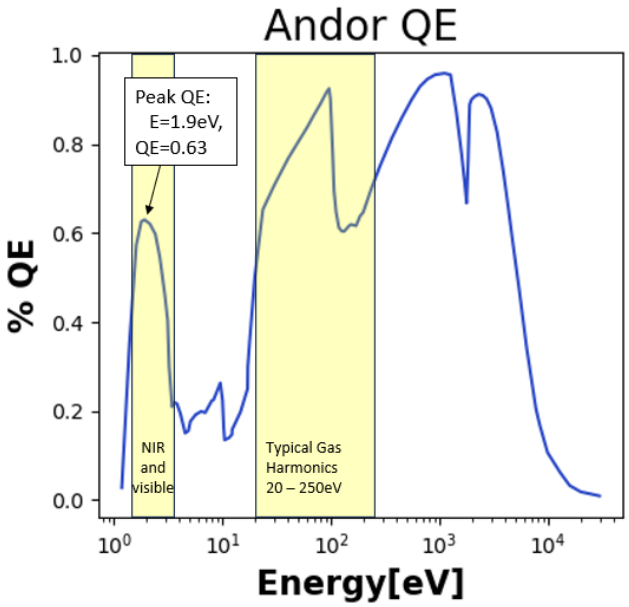

Figure ***32*** This diagram was transposed from some of the official documentation included with the Andor camera. It depicts the quantum efficiency of our Andor x-ray camera as a function of photon energy.

3.3.2 Diffractive Optics

To lowest order, the action of gold reflective grating is a simple specular reflection. For some types of grating, the zeroth order diffraction which contains all wavelengths is aligned with this specular reflection. The incoming and outgoing angles relative to

the "blaze normal" are equal. The echelle grating contains a periodic pattern of triangular steps. These steps serve to shift the specular away from the zeroth order. This increases the efficiency of a higher order diffractive mode for a particular wavelength.

$$\theta_i - \theta_B = \theta_B - \theta_f$$

$$\equiv \theta_f = 2\,\theta_B - \theta_i$$

$$m\,\lambda = d\,[\,\sin(\theta_i) + \sin(\theta_f)\,]$$

$$= d\,[\,\sin(\theta_i) + \sin(2\theta_B - \theta_i)\,]$$

$$= d\,[\sin(\theta_i) + \sin(2\theta_B)\cos(\theta_i) - \sin(\theta_i)\cos(2\theta_B)]$$

$$= d\,[\sin(\theta_i) + 2\sin(\theta_B)\cos(\theta_B)\cos(\theta_i) - \sin(\theta_i)\cos^2(\theta_B) + \sin(\theta_i)\sin^2(\theta_B)]$$

$$= d[2\sin(\theta_B)\cos(\theta_B)\cos(\theta_i) + 2\sin(\theta_i)\sin^2(\theta_B)]$$

$$m\,\lambda = 2d\,sin(\theta_B)\sin\,(\theta_i + \theta_B)$$

For a given blaze angle θ_B and input angle θ_i, there is a wavelength that is maximized for a higher diffractive order, m.

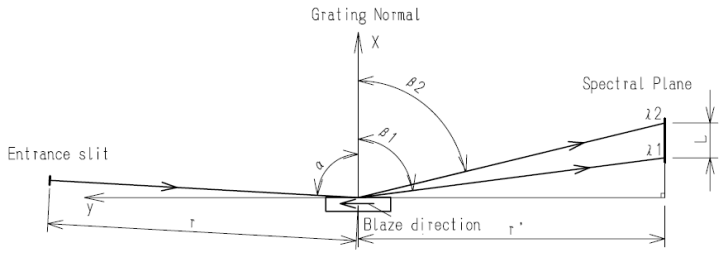

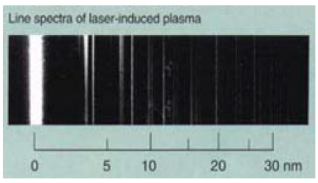

Grazing-incidence soft X-ray spectrograph with flat-field image focusing
The spectra of the soft X-ray region can be observed on a flat photographic plate when the grating is mounted at an incidence angle of 87°(001-0437, 001-0266).

Part No.	Grooves per mm	Radius of curvature (mm)	Blaze WL (nm)	Blank size H×W×T (mm)	Blaze angle (degree)	α (degree)	r (mm)	β1 (degree)	β2 (degree)	r ' (mm)	VL Rang λ1 to λ2 (nm)	L (mm)	Material
001-0437 *1,2	1200	5649	10	30×50×10	3.2	87	237	-83.04	-77.07	235.3	5~20	25.3	Pyrex
001-0266 *1,2	1200	5649	10	30×50×10	3.2	87	237	-83.04	-77.07	235.3	5~20	25.3	Zero Dur
001-0450 *2	2400	15920	1.5	30×50×10	1.9	88.7	237	-85.81	-81.01	235.3	1~5	19.99	Pyrex
001-0471 *2	2400	15920	1.5	30×50×10	1.9	88.7	237	-85.81	-81.01	235.3	1~5	19.99	Zero Dur
001-0639	600	5649	31	30×50×10	3.7	85.3	350	-79.56	-67.26	469	22~124	110.16	Pyrex

Figure 33 The Hitachi Grating Spec Sheet. The two gratings employed in the heart of the two EUV spectrometers currently used in the UC Irvine Laser Lab. They are listed as part number

"001-0437 *1, 2" and "001-0639". Colloquially, the two gratings are simply called the "1200."

The grating used was cylindrically curved resulting in sub-micron spot. (See Figure 33) This was much smaller than the 13-micron pixel sizes of our x-ray cameras. A schematic of this advantage is shown in Figure 34. The position and angle of the grating and the camera relative to the grating is what determines the imaging quality.

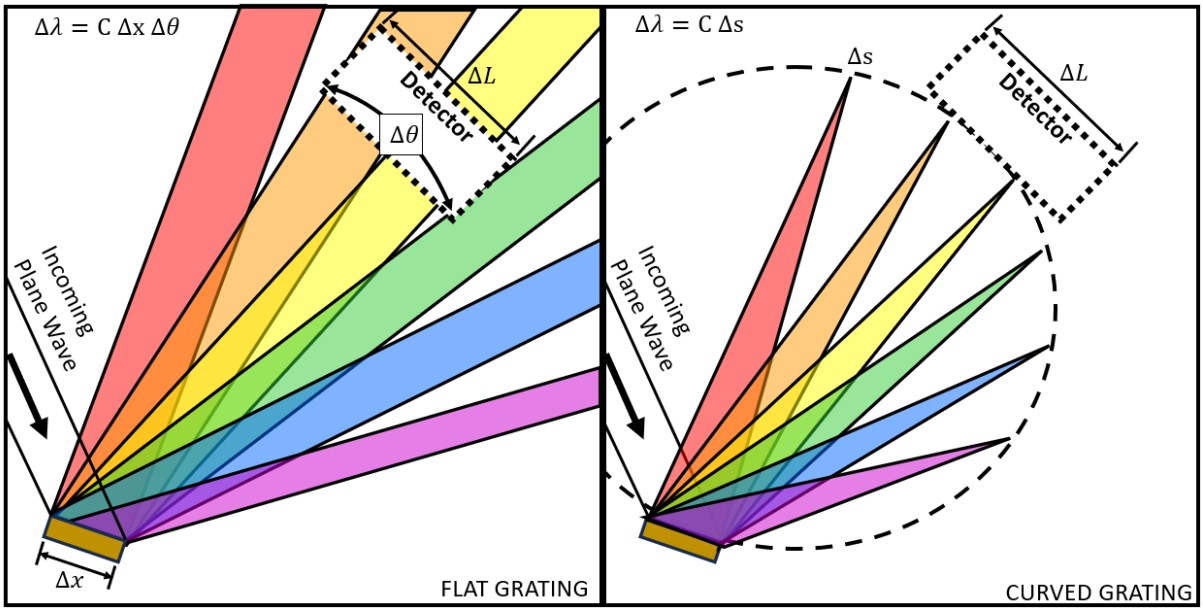

Figure ***34*** This depicts how a curved grating versus a flat grating project their diffracted orders.

3.3.3 X-ray filters

X-ray filters are required because the detector is still very sensitive to visible and optical light. In fact, a response from the detector is triggered for every other photon. The energy of one single 800nm photon is 2.83×10^{-19} Joules. Each pulse of the laser can contain up to 7mJ. Additionally, on continuous fire mode, a thousand of these

pulses are incident on the chip every second. $\frac{7J}{2.83\times10^{-19}J/photon} = 2.819 \times 10^{19}$ photons. The counts produced by a single photon on the Andor is $(Photon\ Energy\ eV)\ /\ (3.55 \times Gain)$. The standard gain setting is 7, which corresponds to 7 photoelectrons per count. For an 800nm photon, the counts/photon would be 0.062 for the standard gain. Combined with the 50% QE, this would mean that full beam impinging on the detector would produce about 8.8×10^{17} counts/s. The Andor camera used was only 16-bit though. This translates to a bit depth of about 65,000 counts. Even if the roughly 10^{18} counts/s (rounding-up) were dispersed over every one of the camera's million pixels, the out-of-the-box Solstice laser would still fully saturate the camera.

Filtering and total removal of optical light is thus paramount. Even if 1% of the fundamental makes it to the detector, the noise from the fundamental will obscure any measured signal.

Except Cobalt, the Figure 35 shows the EUV transmission of various 200nm thick filters used. The two most commonly used were Aluminum (Al) and Zirconium (Zr). Even using just Aluminum and Zirconium, the transmission coverage was above 50% almost everywhere except for a dip in Zirconium just before 250eV. For the infrared though, the referenced transmission for just 5nm of Al is 35% or 0.35. With 200nm, the transmission is exponentially lower $0.3^{(\frac{200nm}{5nm})} = 5.8 \times 10^{-19}$. This would completely block the fundamental (or driver-beam)—assuming there are no pinholes in the filter. Even if there were though, this could be managed by stacking a second filter.

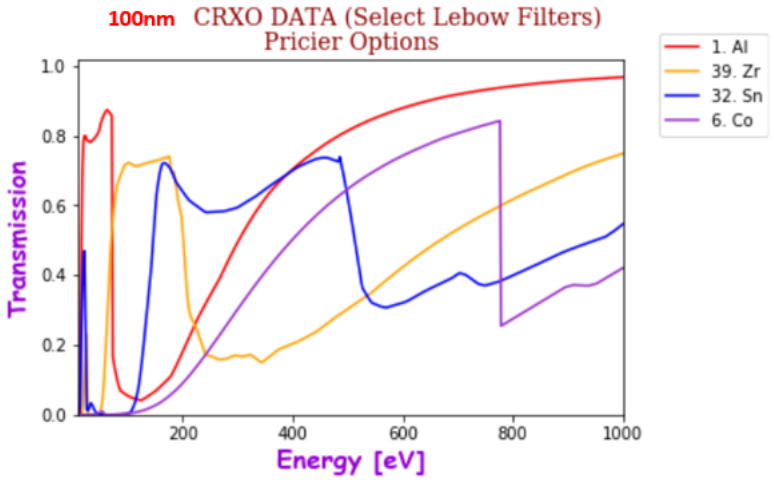

Figure ***35*** Transmittivity for various 100nm foils These curves were generated from the data in the CRXO database[63].

3.3.4 Optical Ray Tracing

The grating has a curved surface like that of a simple metallic cylindrical mirror. However, the focusing of the harmonics is like that of a simple curved mirror only for the zeroth order diffracted beam. For the higher diffractive orders, the grating equation must be combined with the law of reflection for a curved surface. This already seemingly complicated calculation is further compounded by the grating having a nonuniform groove density. The groove density is described by a cubic polynomial and unspecified by the official documentation. The spec sheets only list the groove spacing in the very center of the grating although these same gratings have been manufactured and distributed by Hitachi since the 1980s. This is the equation for the "1200" or the 001-0437 *1, 2 [64, 65]:

$$d(x) = 12000\frac{lines}{cm} + 849.74\left[\frac{lines}{cm^2}\right]x + 51.42\left[\frac{lines}{cm^3}\right]x^2 - 3.15\left[\frac{lines}{cm^4}\right]x^3$$

A uniform line-spaced grating focuses different wavelengths to a curved image plane. If the curvature is not too great, this is appropriate for most digital cameras. Many cameras tend to have a flat rectangular chip. The purpose of the nonlinear spacing is to focus each wavelength focus to a flat plane. This means that every wavelength can be in crisp focus if the camera is correctly oriented.

Raytracing is a graphics method for simulating light's physical behavior. While there are many commercially and freely available ray-trace codes such OpticsStudio and SHADOW, the interface for these ray-trace codes was not very user friendly. Therefore, the focus turned to writing simple line-by-line code using the python packages *NumPy* and *matplotlib.pyplot*. With matrix methods, it turned out to be surprisingly simple—a figure showing just the lines of code could be posted. Figure 36 below shows some of the ray tracing in action.

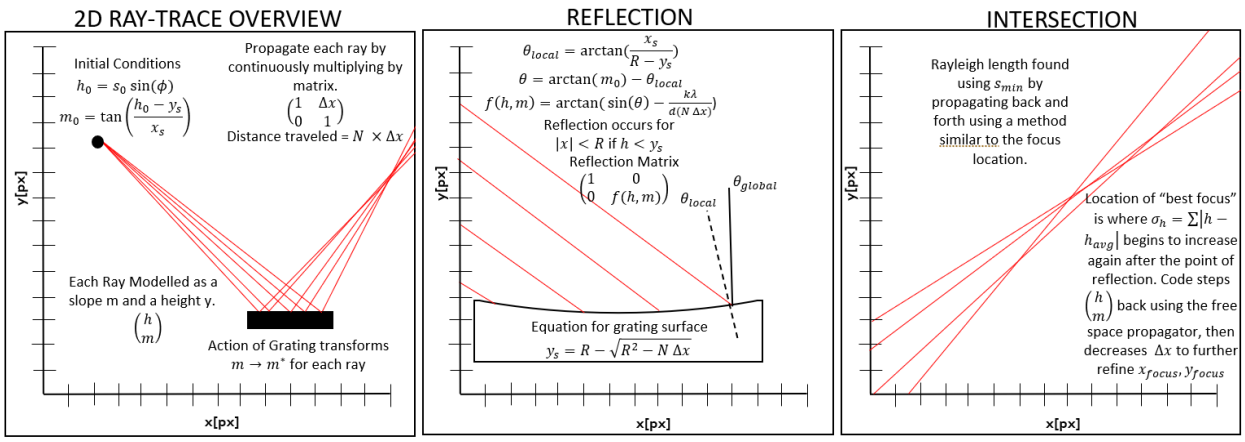

Figure ***36*** Annotated Overview of the operation of the code.

A sample output of the code is depicted in Figure 37. At a fixed grating angle of 3deg, it depicts how the shape of the focal plane for 5 to 20nm wavelengths changes as a

function of source distance. For a source distance of 300mm, the image plane approximates a straight line for the listed parameters. This "flat field" operation is typically what was desired because a field that becomes too curved causes only some signals on the chip to be in focus.

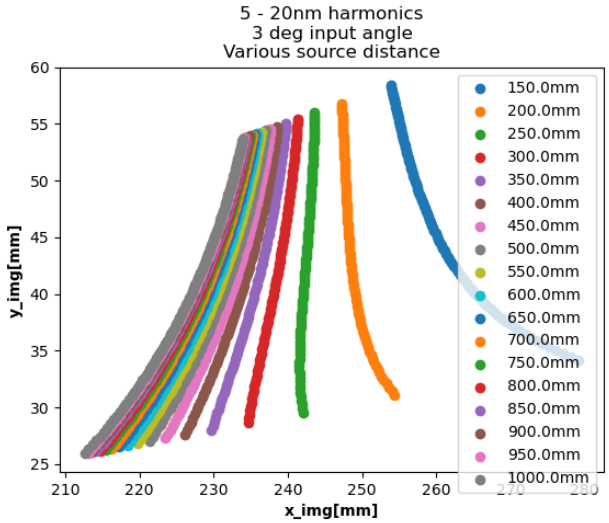

Figure 37 A sample calculation from the code. This shows the shape of the image plane for a range of wavelengths.

The ray-tracing calculations were used to generate the following table. These show the parameters for flat field operation for the 1200nm grating. These assume a beam containing 20 to 45nm.

SourceDist[mm]	Angle[deg]	x-img [mm] (∥ to grating)	$\sigma_x\,[mm]$	y1-img [mm] (⊥ to grating) Highest-E	Y2-img [mm] (⊥ to grating) Lowest-E
237	2.4	230.08	0.411	52.081	79.248
300	2.62	230.14	0.409	52.292	79.386
400	2.86	230.09	0.409	52.504	79.521
500	3.02	229.98	0.409	52.628	79.599
600	3.14	229.89	0.408	52.725	79.659
700	3.25	229.89	0.408	52.848	79.739

800	3.32	229.81	0.408	52.898	79.769
900	3.39	229.80	0.407	52.974	79.819
1000	3.45	229.79	0.407	53.043	79.863
1500	3.62	229.65	0.407	53.201	79.962
2000	3.72	229.60	0.406	53.309	80.031
3000	3.82	229.52	0.406	53.408	80.093
5000	3.92	229.50	0.405	53.534	80.175
10000	3.99	229.45	0.404	53.612	80.279
100000	4.06	229.42	0.404	53.697	80.279
1000000	4.06	229.39	0.404	53.686	80.271

Table 1 Flat field operation of the Hitachi grating for wavelengths from 20 to 45nm

Here is a similar table for the same grating, but a beam containing 5 to 20nm:

Source Dist[mm]	Angle[deg]	x-img [mm] (∥ to grating)	$\sigma_x\ [mm]$	y1-img [mm] (⊥ to grating) Highest-E	Y2-img [mm] (⊥ to grating) Lowest-E
50	1.51	234.96	0.45	26.810	52.904
100	2.11	235.16	0.39	27.504	53.306
200	2.82	235.35	0.31	28.570	53.932
237	3.00	235.40	0.29	28.881	54.116
300	3.25	235.52	0.26	29.352	54.396
400	3.54	235.58	0.23	29.919	54.737
500	3.75	235.62	0.21	30.351	54.999
600	3.91	235.66	0.19	30.695	55.208
700	4.04	235.75	0.18	30.998	55.392
800	4.14	235.74	0.17	31.216	55.526
900	4.23	235.85	0.16	31.445	55.666
1000	4.3	235.85	0.15	31.606	55.765
1500	4.53	235.87	0.13	32.148	56.101
2000	4.66	235.91	0.12	32.472	56.303
3000	4.8	235.96	0.11	32.827	56.524
5000	4.92	235.99	0.10	33.137	56.719
10000	5.02	236.09	0.096	33.414	56.893
100000	5.11	236.11	0.089	33.653	57.044
1000000	5.12	236.13	0.089	33.682	57.062

Table 2 Flat field operation of the grating for wavelengths from 5 to 20nm.

Figure ***38*** shows the information included from the "high energy" 5 to 20nm chart in a graphical form:

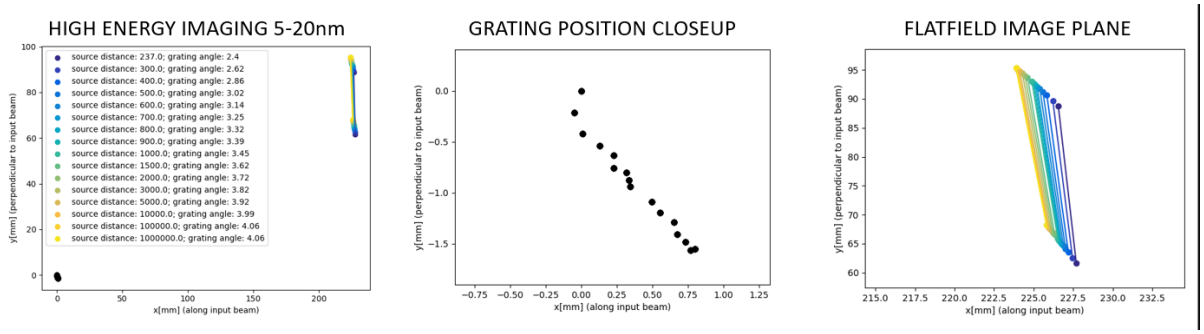

Figure 38 Flat field Hitachi grating imaging. This is a distillation of the information from Table 2.

These calculations were used to inform the design of two spectrometer chambers. (See Figure 39)

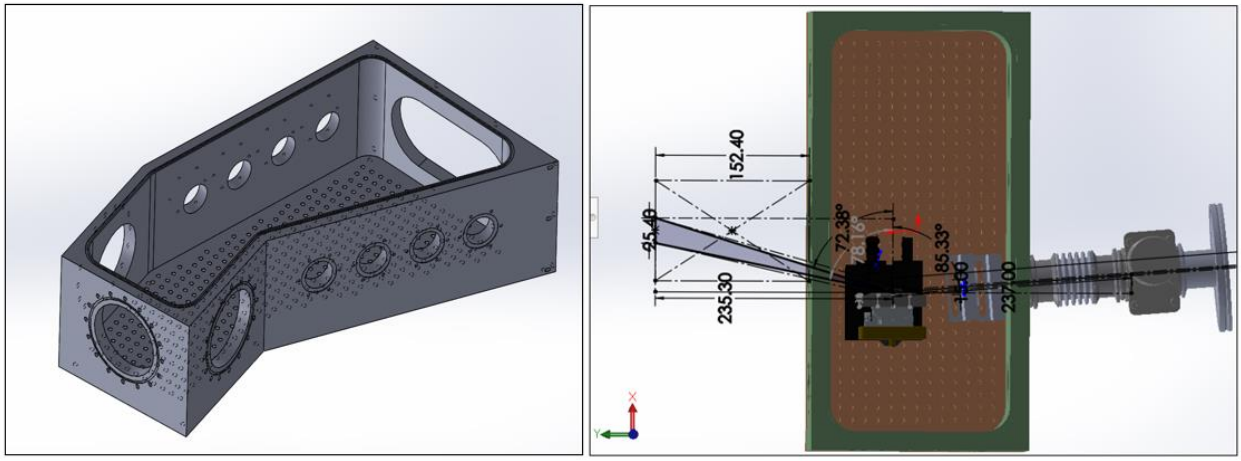

Figure ***39*** CAD drawings of some of the vacuum chambers designed by the author. LEFT was the author's first chamber. It was designed using the spec sheet for the 600nm grating. It was manufactured in the UCI machine shop. RIGHT was a spectrometer assembly.

3.3.5 Experimental Characterizations

Some of the results from the theoretical ray tracing were verified experimentally.

The source chamber was set up for a laser-solid plasma interaction. The beam fired was the standard beam from the Solstice operating at spec: $800nm\ 35fs$ pulses at a $1kHz$ repetition rate. The energy per pulse varied from 2 to $5mj$ to determine if the plasma emission lines could be observed turning on and off. The beam was focused on intensities ranging from $9.5 \times 10^{17}\ W/cm^2$ to $2.4 \times 10^{18}\ W/cm^2$ with an f/2 OPA.

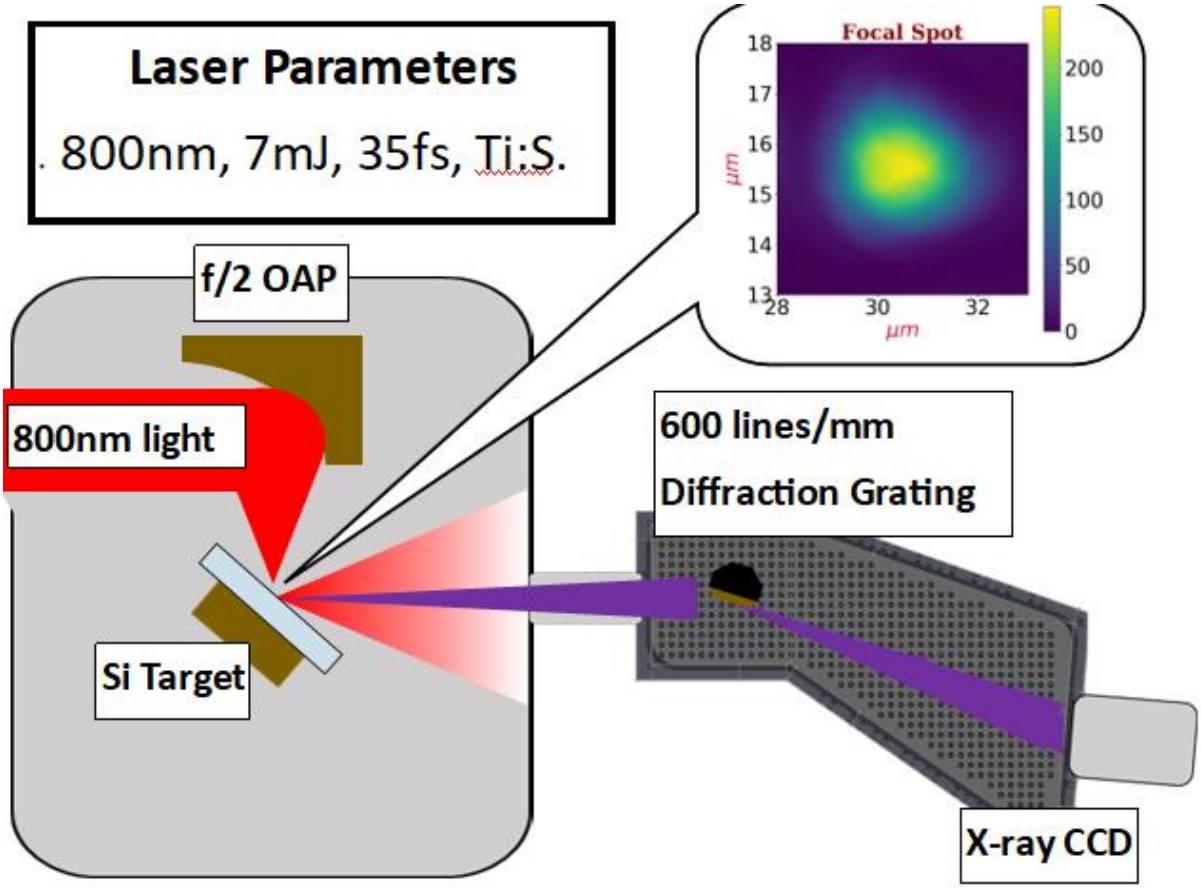

Figure 40 A schematic diagram depicting the experimental setup.

Whilst keeping the source parameters fixed, we shifted and scanned both the grating angle and position. The two vertically stacked images on the left side show the results of shifting the angle. The two dark red lines seen at horizontal pixel positions 650 and 1000 in the top image are the same lines seen at 150 and 350 in the bottom image. The bottom image was at a bigger grating angle and the narrower and higher count lines suggest higher contrast imaging. The plot on the right depicts the impact of shifting the grating position parallel to k-vector of the incoming source beam. The reading on the stage was shifted continuously from 1.5 to $2.4mm$. There was a clear optimization at $1.8mm$. (See Figure 41.)

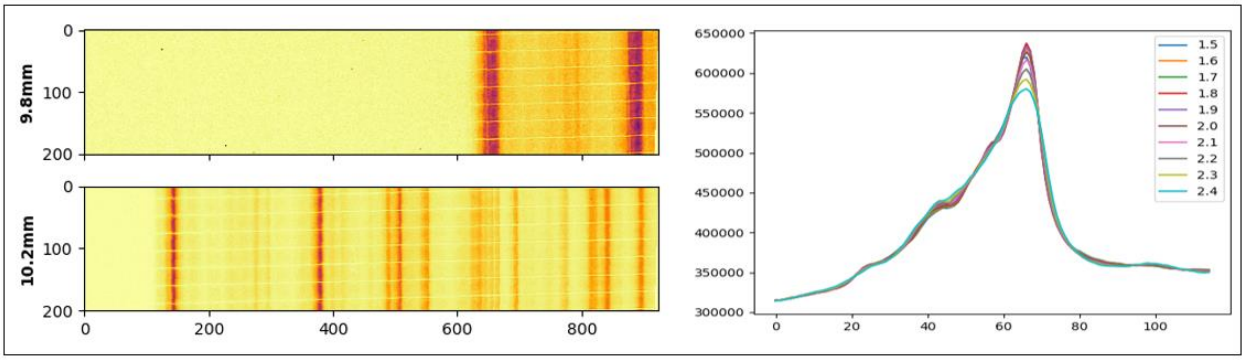

Figure ***41*** Results of shifting the grating position and angle.

The wavelength resolution could be quickly estimated by just looking at some closely spaced emission lines. (See Figure 42.)

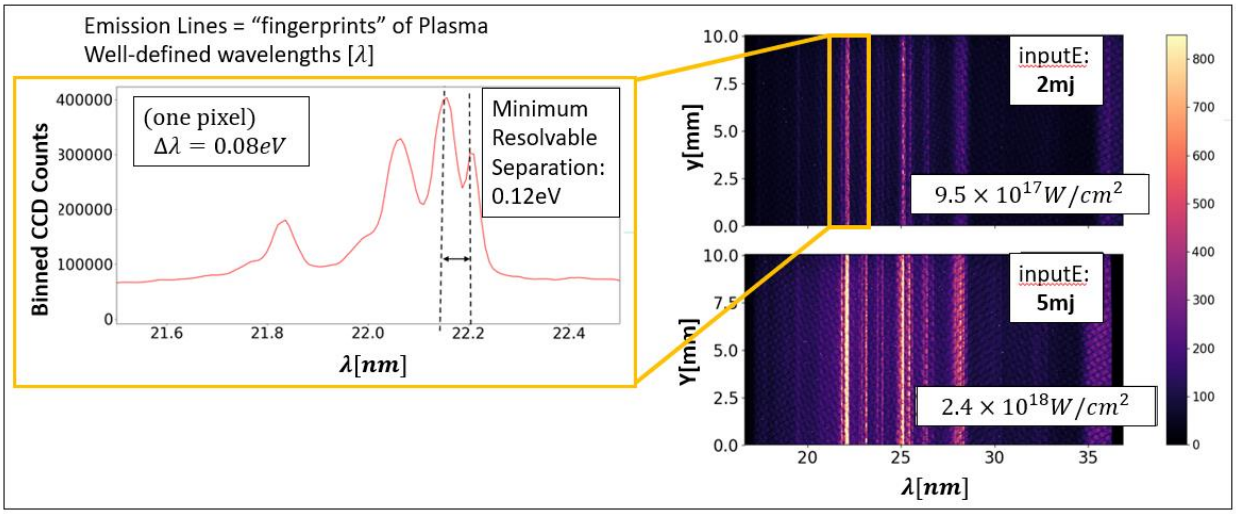

Figure ***42*** Estimation of wavelength resolution of the spectrometer by using three closely spaced Oxygen Lines

Chapter 4

High Harmonic Generation from 3d-printed Laser-Gas Targets

4.1 Introduction

Spectroscopy is a well-established technique of using light to probe matter on the smallest scale. Many neutral materials contain resonances in which light with very specific wavelengths (especially EUV wavelengths) is strongly absorbed. The pattern and structure of this absorption is intimately related to the fundamental quantum properties of the material. To resolve this structure, EUV beams with sufficient brightness and signal-to-noise contrast are required. For example, the transmission of light $(I_{final}/I_{initial})$ through 200nm thick aluminum drops by 10^{-3} beyond the k-edge at $72eV$. The light incident on the detector for a specific exposure would need to have a reading of at least $10{,}000$ counts to see any signal in the region of the absorption

edge. Synchrotrons can easily supply the necessary light, but they are only available through large facilities and are very expensive.

Gas Harmonic Generation is a technique whereby infrared and mid-infrared wavelengths can be converted into high harmonics of the driver. Depending on the driving wavelengths, the high harmonics can have EUV energies and beyond. The conversion efficiency can range from 10^{-6} to 10^{-12} depending on the details of the interaction. Phase-matching is a technique which can produce signals with efficiencies at the upper end of the stated range. When phase-matched, signal can be built-up and will scale with the length of the interaction media. This scaling will continue until reaching a point of saturation called the absorption limit.

There are a variety of different targets used for gas harmonics. Those commonly used are cheap, mass-produced, and commercially available. The gas jet is one such target. It is simply a tube with an orifice that allows gas to flow when backed with some nominal pressure. It is versatile and can be employed in a variety of setups. However, its small interaction length can make it difficult to achieve absorption-limited fluxes. A tight micron-diameter focus and high gas-density (1-10 atmospheres) can overcome the short interaction length. For example, absorption-limited fluxes were achieved by one lab group with 800nm argon, a $150\mu m$ gas jet, and a backing pressure of 6.5 atmospheres[66]. Relying on sufficiently powerful pumping speeds[66], these on-target densities are difficult to achieve practically. Without the required density, the flux from a gas jet geometry drops precipitously to the single-atom yield [67] [68]. Hollow core waveguides are a ubiquitous alternative to the gasjet. It can circumvent the issue of the shortcoming of small interaction lengths, instead offering good gas confinement as well as centimeter-long media

lengths[55]. 800nm Argon can achieve absorption-limited flux with just 1 PSI ("pound per square inch") backing pressure[66]. These stated benefits do come at the cost of versatility. Unlike the gasjet, the beam must couple into a waveguide mode and is confined to just one dimension.

In recent years, advancements in additive manufacturing technologies have opened a third option: 3d-printing. In theory, this technology permits inexpensive custom gas-targetry with a fast turnaround. The following sections describe an experiment to assess the viability of 3D-printed gas cells. The new 3D-printed targets were compared to the gas jet as well as a gas cell analogue, the steel-drilled capillary. The 3d-printed targets showed orders of magnitude improvement in photon flux. These measurements suggest that 3d-printed targets may be a superior alternative to all existing targetry. They appear to offer both the high-flux of the hollow core fiber without sacrificing flexibility. Additionally, as most university campuses offer 3d-printing services, a successful target design can be tested, then rapidly shared and disseminated to gas-harmonic experiments worldwide.

Harmonics produced via Gas High Harmonic Generation (Gas HHG) are a promising way of generating extreme ultraviolet (EUV) light with attosecond duration pulses. In this section, Gas HHG signal produced from a couple of different target types, including 3d-printed gas cells, is shown. It was found that the novel 3d-printed gas targets were able to be phase-matched with integrated fluxes of 10^7 29^{th}-harmonic photons per single interaction. This signal was an order of magnitude brighter than the other tested off-the-shelf target types. The reason for this improved performance is discussed. The viability and flexibility of 3d-printed gas cells for exotic gas-harmonic geometries is also discussed. These are gas-harmonic systems which would

normally be difficult to achieve with standard targetry. Experiments involving 3d-printed gas cells and phase-matched noncollinear harmonics are shown as proof of concept.

4.2 Methods

The experiments were performed with a commercially available Ti: Sapphire laser system (Spectra-Physics Solstice ACE). The energy accessed was 1 mJ of 800nm light. The spatial mode of the laser was a gaussian with an m-squared of $M^2 < 1.25$. The pulse duration was observed to be 35fs with a FROG measuring device. The primary focusing optic was an IR-coated f=30cm lens. The beam was variably apertured by an iris before the lens. When the aperture was fully open, the f-number of the focusing geometry was twenty-five.

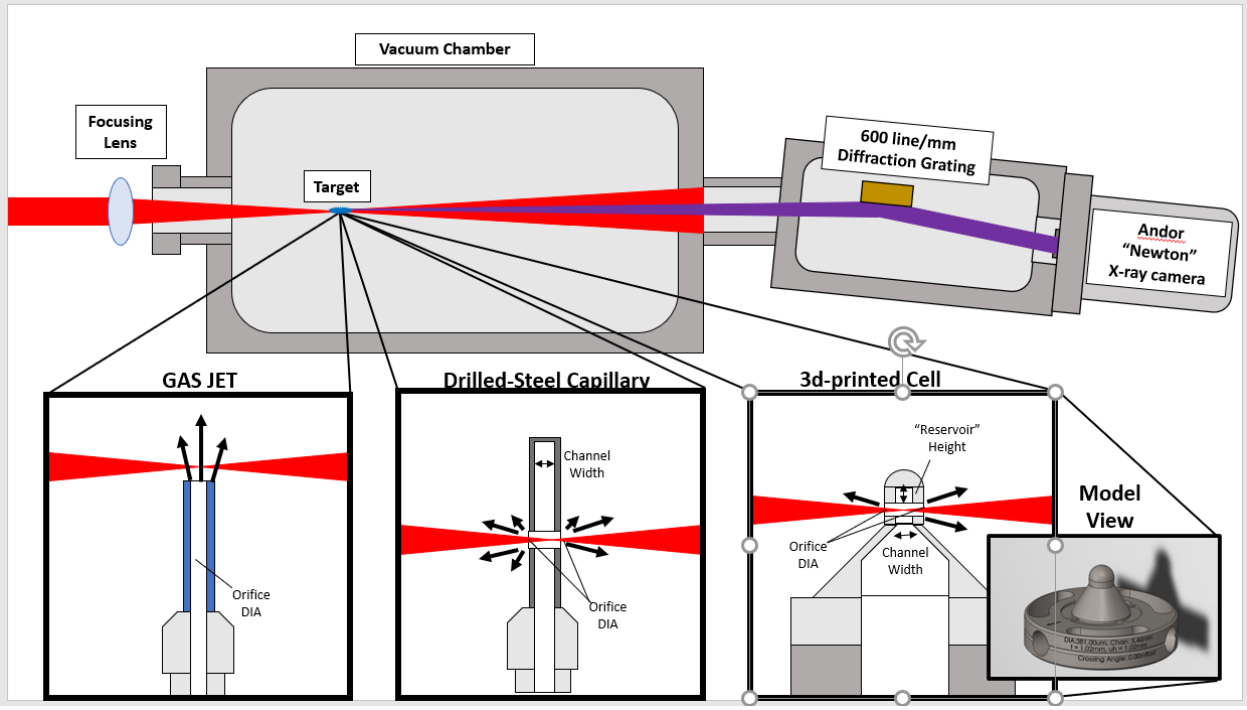

Figure 43 A schematic setup of the experiment.

Three target-types were compared. Number one was the free-flowing capillary or gas jet. The gas jet was cut from 1/16" diameter peek tubing which had a $250\mu m$ orifice diameter. It was mounted using 1/16" compression fittings. Number two was the drilled-out steel capillary or conventional gas cell. It was made from 1\16" diameter steel tubing also with a $250\mu m$ orifice. One side was crimped, then the side was manually drilled through to create a $500\mu m$ thru-hole. The third target was the 3d-printed gas cell. Unlike the other two target types, it was fully customizable. The entry and exit orifices were each made to be $500\mu m$. This was to make it more comparable to the drilled steel capillary. However, the channel width was allowed to be continuously varied from 1mm to 5mm. The initial batch of gas contained a set of targets (some duplicates) that were mostly identical except for mostly differences in the channel width. These were used to generate measurements of the photon flux versus interaction length. Some subsets of the targets contained an "upper reservoir". This was a region of free volume above the location where the laser passes. These targets were found to have the best flux and were used in the measurements of phase-matching. A graphical depiction of each target archetype as well as a schematic of the setup are shown in Figure 43.

The targets directed argon gas into the region of interaction. No differential pumping setup was employed. This had the advantage of a lower overall ambient pressure in the region of the target. Smaller ambient pressure typically means less gas reabsorption of the harmonics and more counts on the detector. When argon was flowed continuously, the chamber ambient pressure could only get as high as 10^{-2} Torr.

The 3d printed targets were created with a Stratasys Objet260 Connex3 3D printer, with high-density VeroClear as the print material. The printing-system itself was capable of an idealized layering resolution of 15 microns. The printing process would fill open areas of the print with support material (SUP706). This was removed with water jets, lye-solution, and an ultrasonic cleaner. Small features like the 250-500um orifices were cleared mechanically by poking them through with $250\mu m$ music wire. The CAD (computer-aided design) drawing of the 3d printed part is depicted in Figure 43. The design had three priorities. One, it had to interface with our existing gas-components. Two, it had to transmit an $\geq f30$ focus without interference. Three, the density in the interaction region was homogeneous.

The first tests with the printed targets verified their vacuum compatibility. The targets were attached via a CF16-to-1/4" Swagelok adapter and a Viton O-ring gasket. The vacuum tightness of this connection was verified by flowing argon into a test target with no orifices. The chamber pressure remained at the no-load ambient pressure of 10^{-5} Torr even when backing this test target with 10 atmospheres or more.

In terms of alignment, the gas jet was most difficult to align. This is because the height and positioning of the beam relative to the orifice strongly affects the shape of the density profile in the interaction region. The standard alignment procedure was to position the gas jet first by hand. Then, if necessary, fine adjustments of no more than $\pm 100\mu m$ were made with actuation knobs which translated the position of the focusing lens. The brightness of the plasma emission was used as a guide. The gas jet was run at a pressure of at least a few atmospheres to make the plasma and changes in brightness more apparent. Final optimizations were made under vacuum looking at the harmonic signal. The gas jet would be run at just a few PSI. Then, the

beam would be positioned as close to the gas jet orifice as possible without burning. The signal tended to increase dramatically the closer it could get to the orifice.

The two kinds of gas cell were much more straightforward in terms of their alignment. If the focus of the beam passed through both holes without visible aberration of the outgoing beam profile, the system was aligned. This could be done consistently just by hand. These procedures were first carried out first with a low-power collinear alignment beam. Then, a reduced power ASE beam was used as a final check before pumping down the chamber.

For the purposes of making a systematic comparison of each target type, as few parameters as possible were changed during target swaps. Once the pointing of the beam was initially defined, further tilting of mirrors or lenses was specifically avoided. The key experimental parameters that changed between targets were the diameter of the aperture before the lens, the input beam energy, and the target backing pressure. The diameter of the aperture changed the on-target beam intensity and Δk_{guoy} phase-matching term. The backing pressure changed the interaction density. The best parameters for intensity and density tended to optimize in the same place within tolerance for the targets.

The outgoing EUV beam from the interaction was diffracted into discrete harmonics by using a 600 line/mm grating. The EUV harmonics were detected with an Andor-Newton x-ray CCD. The spectrometer was also held under vacuum and could be isolated from the interaction chamber via a KF40 gate valve. It was optimized for observation of the 29^{th} harmonic. Between target swaps, the interaction chamber had to be vented to access the targets. However, the spectrometer was kept under vacuum with the settings kept fixed.

4.3 Results

The peak flux for three different targets is shown in Figure 44. (Peak flux refers to the maximum photons captured by just a single pixel.) For each target, the harmonic flux optimized for 0.3mJ input energy through the aperture before the lens. This translated to a f-number of fifty-five. This f-number and energy corresponded to an optimal interaction intensity of roughly $1-2\times10^{14}\,\mathrm{W/cm^2}$. The optimal pressure was $1\pm0.5\,PSI$ for each target. The figure below depicts the measurements of "channel length" (distance between two orifices) versus peak flux of the 29th harmonic. It could be seen that the harmonic flux increased with the channel length.

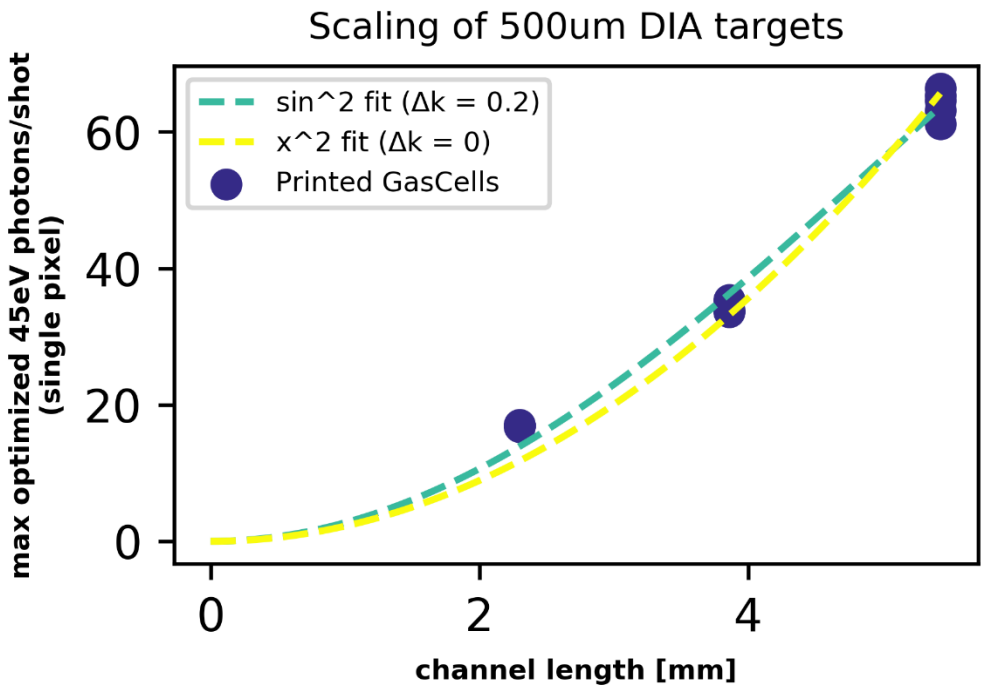

Figure 44 Flux Scaling for Gas Cell targets. "Channel length" (distance between orifices) versus peak flux of the 29th harmonic.

At the optimal intensity of $1-2\times10^{14}\,W/cm^2$, the density was varied. This corresponded to energy after the aperture of $0.05-0.4$ mJ. Figure 45Figure 44 compares four different targets: two of the 3d-printed gas cells, a drilled-steel capillary (conventional gas cell), and a gas jet. Only the 3d printed gas cells would optimize before the shutoff point. For the other targets, the limit before shutoff of 10^{-2} Torr ambient pressures could only be exceeded by "pulsing". This "pulsing" amounted to opening and closing the valve on the regulator, then acquiring a shot as fast as possible. This was necessary to fill out some of the data points for the phase-matching curves. The technique worked for the steel-drilled capillary, but the gas jet saturated the chamber with gas too quickly to take a camera acquisition.

Figure 45 depicts how measurements of the integrated 29th harmonic flux varied as a function of backing pressure. The chamber ambient pressure is quoted as a proxy for the backing pressure/gas density. This was because the cold-cathode gauge attached to the vacuum chambers had a better resolution (quoted accuracies of up 10^{-8}) than the gauge attached to the regulator (dial with 1 PSI divisions). The two 3d-printed cells had the same "channel length" (distance between the orifices), but they differed in the presence or absence of the "upper reservoir." It was observed that the two 3d-printed cells optimized with roughly the same density and laser parameter inputs. However, for these same input parameters, the cell *with* the reservoir showed an appreciable (orders of magnitude) flux enhancement. The integrated flux of 29th harmonic for the gas cell with the 2mm reservoir was about 10^2 times more than the cell without. The inferred absolute flux for the "reservoir cell" was ($2.1\times10^7\,photons/shot$).

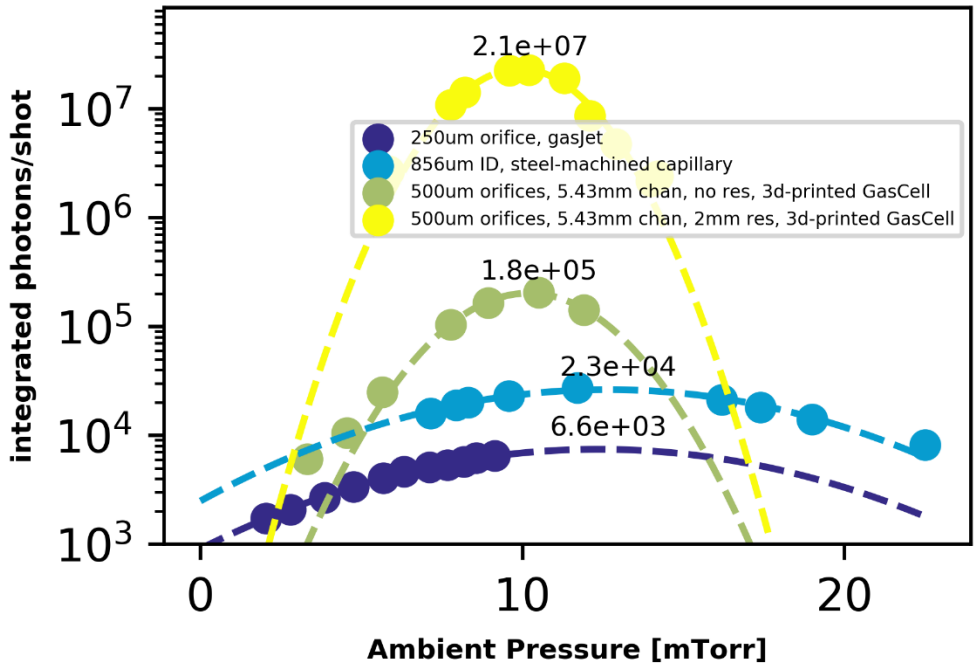

Figure 45 The "phase-matching" curves for four different types of targets. The lower bound absolute flux was quoted for each. The pumping system tended to crash when the ambient pressures began to exceed 10mTorr. The curve for the steel-drilled capillary could be acquired for higher pressures by "pulsing" the cell. ("Pulsing" refers to the technique employed of rapidly opening the regulator, acquiring data, then closing the tank again.) This technique did not work for the gas jet which tended to cause the pumps to fail before data could be acquired. So, the curve beyond 10mTorr was inferred from the preceding data points.

The gas jet signal often operated much closer to the baseline noise level of the detector even for signal integrations of thousands of shots. The gas cell data, on the other hand, could be acquired with just single shot integrations. In this experiment, there was about 0.3mJ per pulse that drove the interaction or about 10^{15} 800nm photons per pulse. Based on the figure, the reservoir gascell achieved a

conversion efficiency of at least $(2.1 \times 10^8)/(10^{15}) = 10^{-8}$. Conversely, the gas jet achieved of at least $(6.6 \times 10^3)/(10^{15}) = 5 \times 10^{-12}$ From literature, hollow core fiber targets can achieve conversion efficiencies of about 10^{-6} [69] [55]. The 3D-printed targets measured absolute conversion efficiencies that were comparable to hollow core fiber results referenced above.

4.4 Discussion

4.4.1 Signal Growth Due to Phase-Matching

The k-vector mismatch Δk quantifies how quickly the fundamental and harmonic will slip out of phase with one another. For finite Δk, as the fundamental propagates a distance Δx, the harmonic light will initial build up before decreasing again. This happens as the light produced later begins to cancel with the light produced earlier. For an interaction length L_{med}, the intensity of the outgoing harmonic radiation I_q can be estimated with the following model:

$$I_q = \left| \int_0^{L_{med}} \mathcal{E}_q^0(x)\ e^{i\,\Delta k\,x}\, dx \right|^2$$

$\mathcal{E}_q^0(x)$ represents the field induced by the driving fundamental. As $\Delta k \to 0$, $e^{i\,\Delta k\,x} \to 1$. Assuming $\mathcal{E}_q^0(x)$ is a constant, then $I_q = \left|\mathcal{E}_q^0\right|^2 L_{med}^2$. This means that flux of the phase-matched harmonic signal should grow quadratically with interaction length. If Δk is nonzero, the intensity scaling would instead grow like $Sin^2(\Delta k\, L_{med})$. Figure 44 features both an L_{med}^2 and $Sin^2(\Delta k\, L_{med})$ fit. For the case of nonzero Δk, the data best fit was 0.2 for the value of Δk. This corresponds to coherence length of 10mm or

longer. This suggests that if Δk is indeed finite, the EUV flux should continue to increase with L_{med} at least until 10mm.

Figure 45 showed the pressure optimization for each target. For single atom, the signal would tend to scale just linearly pressure because pressure is directly proportional to the number of emitters. However, if the integral is solved is solved for constant $\mathcal{E}_q^0(x) = \mathcal{E}eff_q^{0\,2}$, it can be seen that a phase-matched signal will obey the following equation:

$$I_q = \left| \int_0^{L_{med}} \mathcal{E}_q^0(x)\ e^{i\,\Delta k\,x}\,dx \right|^2$$

$$I_q = \mathcal{E}eff_q^{0\,2} \frac{\left| e^{i\,\Delta k\,L_{med}} - 1 \right|^2}{\Delta k^2}$$

$$I_q = \mathcal{E}eff_q^{0\,2} \frac{[2 - 2\cos(\,\Delta k\,L_{med})]}{\Delta k^2}$$

$$I_q = \left(\frac{\mathcal{E}eff_q^{0\,2} L_{med}^2}{2} \right) \frac{\sin^2(\Delta k\,L_{med}/2)}{(\Delta k\,L_{med}/2)^2}$$

$$I_q = I_q^{max}\,\mathrm{sinc}(\Delta k\,L_{med}/2)$$

For fixed L_{med}, this equation approaches a peak I_q^{max} as $\Delta k \to 0$. Near $\Delta k = 0$, the Taylor series representation of $\mathrm{sinc}^2 x$ is $1 - x^2/3 - \mathcal{O}(x^4)$. To lowest order, the signal functional dependence on pressure should be like $P^2\,\alpha\,\Delta k^2$. The density optimums observed for each of the four targets in Figure 45 corresponds well with this finding. They each seem to grow quadratically with pressure, but with different peaks I_q^{max}.

4.4.2 *Gas-Target Homogeneity and Density*

The previous section inferred phase-matching from the shape of the data measurements. This section proposes to answer why the 3d-printed targets appear to offer much brighter phase-matched signal.

The SolidWork's add-on package, "Flow Simulation", was used to model each of the three target-types. It is a CAD-embedded CFD code that solves the full Navier-Stokes equations[70]. SolidWorks' Flow Simulation has already been applied in industry and has been benchmarked against other Computational Fluid Dynamics (CFD) code packages like ANSYS. [71] [72] [73]. For the target modeling, the CFD simulations were conducted to determine how backing pressure related to the density in the interaction region. Figure 46 summarizes the results of two sets of simulations for each target. One set of simulations keeps the density fixed in the interaction, but changes the backing pressure. The other set keeps the backing pressure fixed, but examines the density at the point of interaction.

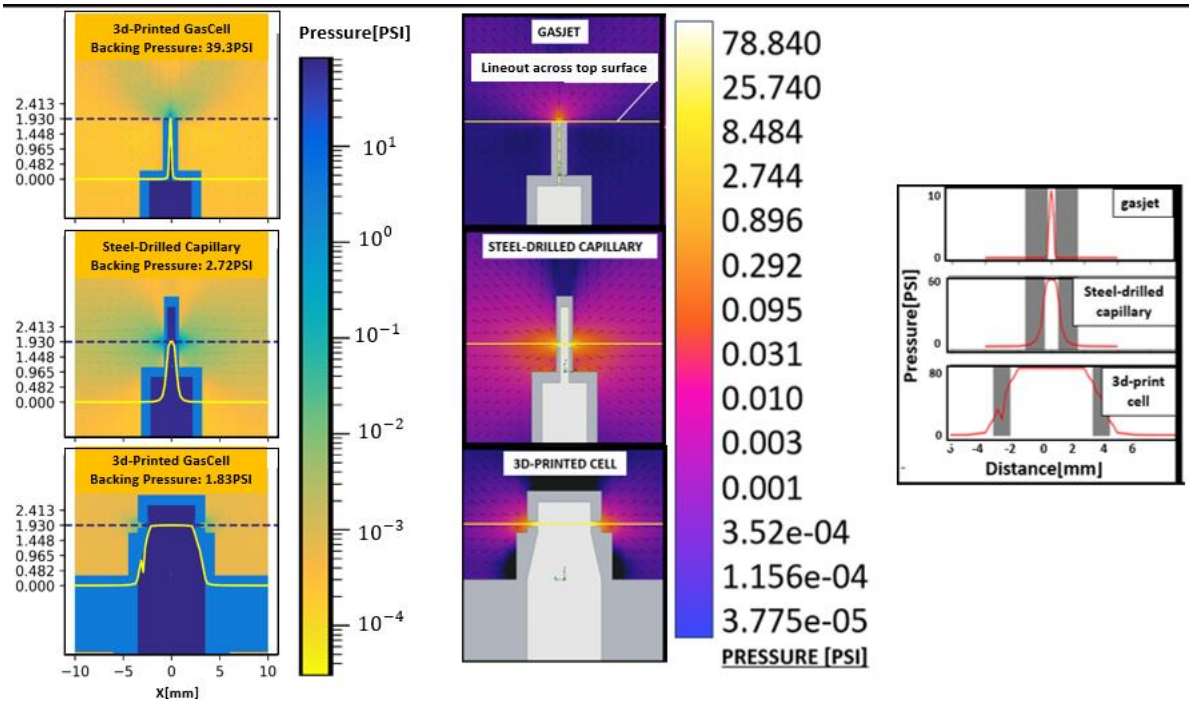

Figure 46 The LEFT plots are a set of simulations that keep the density in the interaction region constant. The y-axis in each plot marks the pressures in PSI along the lineout. The color bar marks the pressures in each of the 2d images. LEFT-TOP shows the results for the jet. LEFT-MIDDLE shows the result for drilled capillary. LEFT-BOTTOM shows the 3d-printed cell. The CENTER plots are Simulations results for a constant density of 80PSI. CENTER-TOP is the gas jet. Middle is the drilled capillary. CENTER-MIDDLE is the steel-drilled capillary. CENTER-BOTTOM is the gas cell. The RIGHT plot has the lineouts for each target. The colors in each image are related to the local pressure. The color bars are given for both simulation sets.

In both sets of simulations, the 3d-printed gas cell offers a millimeters-long region of constant interaction density. For the cell, the lineouts depicting pressure versus distance has a flat-top-like shape. The density at the point of interaction is constant and does not begin to change until reaching the vicinity of the entry and exit orifices. Conversely, both the gas jet and steel-drilled capillary have a much more

inhomogeneous density profile. Their lineout of pressure versus distance are Lorentzian-like with the gasjet much more sharply peaked.

Another interesting characteristic, for the 3d-printed gas cell, there is a one-to-one correspondence between the pressure reported at the regulator versus the actual interaction density. This means that 80 PSI backed results in an identical 80 PSI at the point of the interaction. This was unlike the gas jets, which could require at least 2.5 atmospheres of pressure just to have 1.93PSI in the interaction region. This is just a lower bound though. In practice, the beam must be some distance away from the gasjet so as not to burn the target. This would necessitate even higher backing pressures to achieve a interaction pressure of 1.93PSI.

	BackingP: 1.93PSI	BackingP: 2.72PSI	BackingP: 39.3PSI	BackingP: 80 PSI
Gas Jet			1.93PSI	10 PSI
Steel-Drilled Capillary		1.93PSI		50 PSI
3d-printed Gas Cell	1.93PSI			80 PSI

Table 3 A chart comparing how the peak density at the point of interaction relates to the pressure a particular target is backed with.

In summary, the key feature of the 3d-printed gas cell was its homogeneous density profile. Since Δk is proportional to the pressure P, it would seem that the high brightness of the 3d-printed gas cells might be explained by its homogeneity.

4.4.3 Noncollinear Proof of Concept

Noncollinear gas harmonic generation (noncollinear HHG) is a technique of generating gas harmonics from two focused beams with different $\boldsymbol{k}$-vectors[74]. The overlap of the two foci is typically enforced by sending each beam parallel through

the same focusing optic. The harmonics from such an interaction emerge with many different $\boldsymbol{k}$-vectors. This experimental geometry results in EUV and x-ray gas-harmonics emerging in directions distinct from the driving beams. A basic schematic is shown in Figure ***47***

EUV filters have a limited transmission window that can restrict the range of wavelengths. They will wear and break as they suffer degradation with time. A broken filter at the wrong time can potentially delay an experimental, ruin or cause damage to a spectrometer system. Work with noncollinear gas-harmonics bypasses all these disadvantages entirely. Non collinear gas HHG has the primary advantage of driving beams that can be isolated from the harmonics without EUV filters. Since the harmonics and the drivers are spatially separated, the drivers can just be mechanically blocked.

Experiments involving noncollinear gas-harmonics have been done before. However, previous setups have traditionally employed free-flowing gas capillaries that made phase-matching difficult or impossible for some systems. The measurements of noncollinear gas harmonics here was intended as a proof of concept for the 3d-printed gas cell. Not only can it make very bright signal, but it also enables observation of physics that might be otherwise much harder to do.

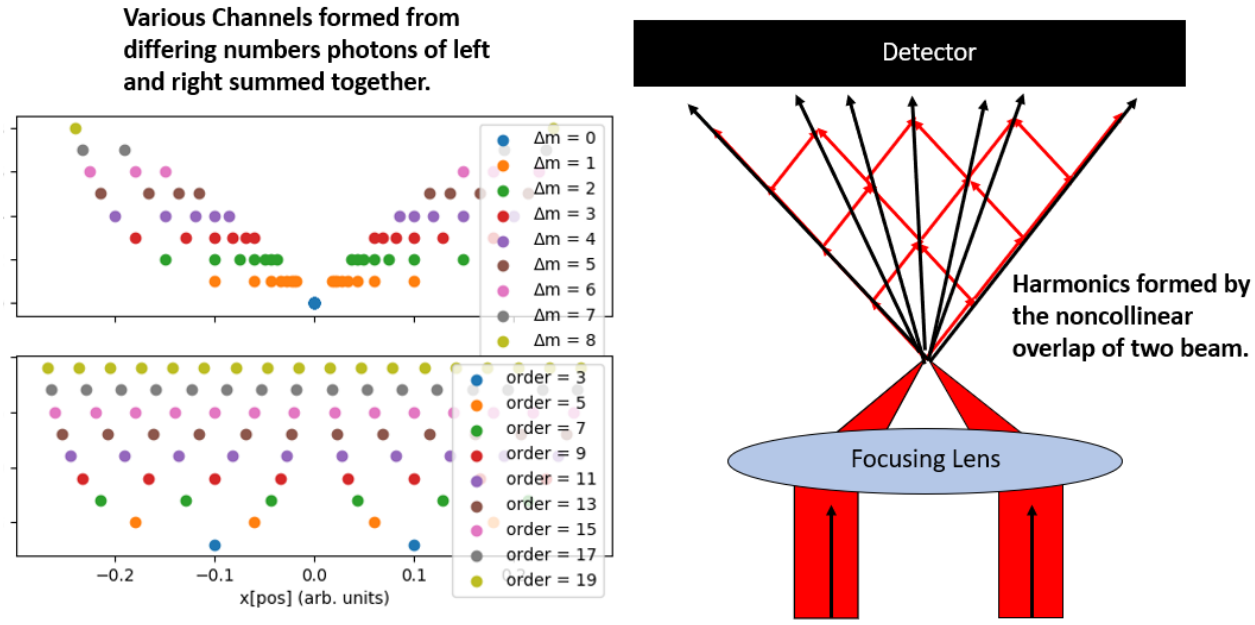

Figure 47 LEFT depicts how different numbers of photons in each arm can be combined to form the multiplicity of overlapping harmonic channels. The units of the y-axis in both of these plots are arbitrary. It was chosen so that the many colors (representing different orders or combinations) did not all overlap all in one place. RIGHT shows a schematic setup of how the crossing of two beams generates secondary beams with k-vector distinct from the two drivers. The red arrows depict different numbers of photons combining from each arm. The black arrows show the resulting k-vectors.

After collecting the data to make Figure 44 and Figure 45, the set up was changed. The x-ray camera was attached directly to exit port of the interaction chamber. The 800nm beam out of the solstice was converted into a little less than 1mj of 400nm using a BBO crystal. This new 400nm beam was isolated from the residual parent 800nm by using two HR400/HT800 dichroic mirrors. (400nm was used to drive the noncollinear experiment because it was expected to phase-match at lower densities.)

From here, two beams of 400nm were made with a coated 50/50 ultrafast beam splitter. The two path lengths for each beam were equalized using a delay stage. The foci were then overlapped by sending each beam parallel through a 2in diameter

f=30cm lens. The center-to-center separation between the two beams incident on the lens was roughly 0.75". Near focus, the beams crossed at an angle of approximately $\arctan(0.75"/300mm) = 3.62°$.

Just the gas jet and one of the 3d-printed gas cells were tested with the noncollinear geometry. The gas cell used was different than all the ones tested for the scaling measurements. It had 250um orifices, compared to 500um. This orifice diameter was chosen because it could be driven at higher backing densities without shutting down the pumping system. The primary downside was that it required a much less forgivable alignment. However, even with the cross-beam geometry, both beams made it through the cell without apparent issue.

The measurements of the noncollinear HHG are shown in Figure ***48***. It depicts only optimized EUV signal from just the 3d-printed gas cell targets. The signal from the gas jet was not readily distinguishable from the background. It was no more than 10s of counts above the background even for backing pressures of >100PSI. The weak signal appeared to respond to pressure, but never reached an optimum. By comparison, there was a clear density optimum for the 250um cell with orifices at 18PSI. Optimal signal resulted when each 400nm beam with 0.4mj energy was apertured down to just 50uJ in each arm. The focus for this aperture size was roughly f60. The vertically binned harmonic flux contained an estimated number >10,000 interaction photons in the space of just one pixel (13 microns). The phase-matched channels would contain photon energies of 35 to 55eV. The absolute photon flux was estimated by assuming that one of the signal counts came from 45eV photons. The signal was produced with the smallest channel target (2.5mm). Conceivably, the flux would continue to improve with longer channel lengths as was observed for the one-

beam collinear harmonics. However, the noncollinear was not pursued further. These measurements were intended just to show results possible with 3d-printed cells.

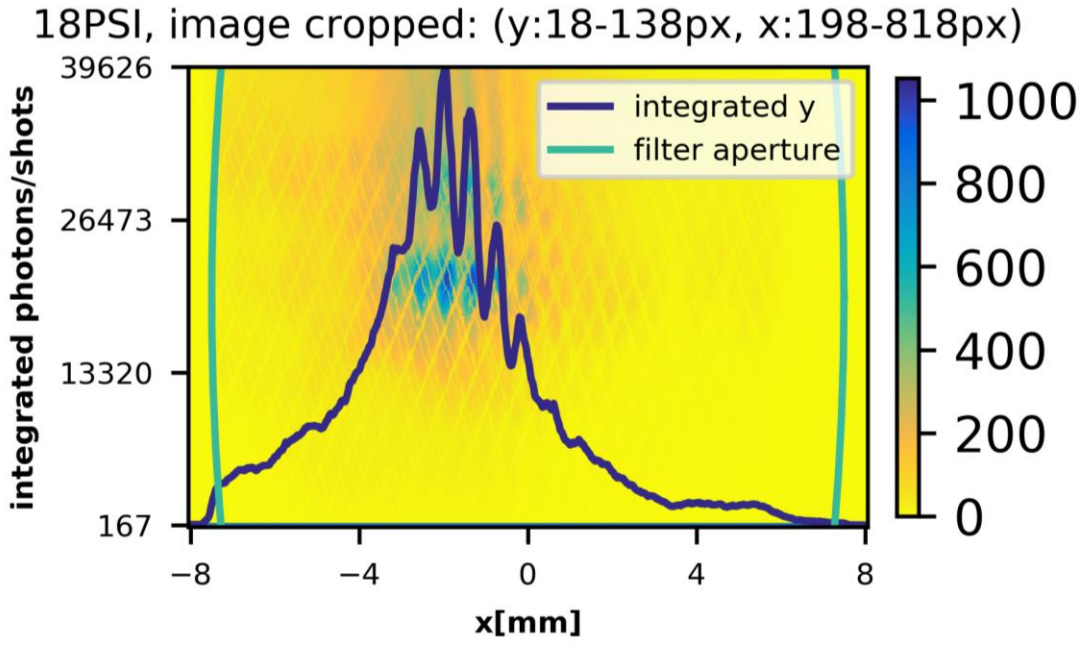

Figure 48 The raw image signal of the optimized noncollinear HHG. The color bar on the righthand side reports the counts reported by the detector. The overlaid lineout shows the total photon flux for the signal binned along the y-axis. The left hand scalebar estimates the absolute photon flux contained in the overlaid lineout.

4.4.4 Signal Stability

For the "reservoir" targets, it was interesting to assess the signal stability during a longer timescale acquisition. The experiment was left continually running without touching any of the optics or other target parameters. Presumably, the harmonic output signal should have also remained constant within some tolerance. The camera was made to automatically acquire few-shot measurements over a collection period of three hours.

Figure ***49*** shows the outcome of this testing. The local shot-to-shot variance was no more than 10 percent. However, over long timescales (like three hours), there was long downward drift in the EUV flux. This decreased flux was able to be restored by reoptimizing the output pressure of the regulator. It seems to be attributable to the pressure supplied by the regulator not remaining constant with time rather than a characteristic of the target itself. The pressure supplied by the regulator is a function of the inlet pressure. As the gas is left continually running, the inlet pressure will decrease as the tank empties.

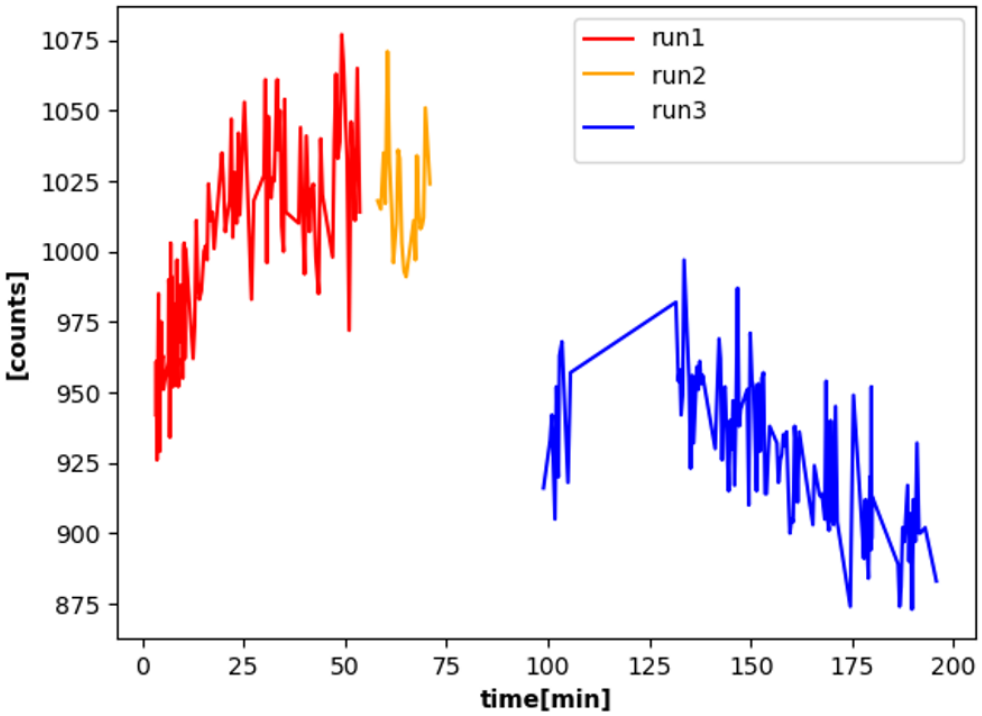

Figure 49 Measurements of the EUV signal output with time. The reported counts were the peak counts contained within the 29th harmonic. "Counts" are what the camera measures directly. As discussed in Chapter 3, these counts can be related to the absolute photon flux. The absolute flux was not calculated because the object of interest was the change in relative flux with time. After an initial increase in flux, the signal underwent a very slow decay. This was ultimately related to fluctuations and drifts in the backing pressure output.

4.5 Conclusion

The 3d-printed targets can achieve the parameters necessary for phase matching. This is confirmed both by the flux scaling with interaction length as well as the scaling with pressure. The 3d-printed "reservoir" target was able to achieve an integrated 29th harmonic flux of $10^7\ photons/shot$. This amount corresponds to a conversion efficiency of about 10^{-7}. Similar studies with hollow waveguide geometries quote absorption-limited efficiencies of about $10^{-5} - 10^{-6}$ [56]. They are close, but there is an appreciable difference. Modification of the design of the 3d-printed cells could possibly close this brightness gap. Compared to the gas jet and drilled capillaries, the difference is substantial, a night-and-day 3 to 4 orders of magnitude. This is the power of 3d-printed targets. They provide a high brightness comparable to the hollow waveguides while preserving the free focus geometry. The proof of concept was the successful detection of 2-beam noncollinear gas-harmonics.

3d-printing offers endless customizability. These cells could eventually be adapted to any other laser-gas-target based experiment. With modification, quasi-phase-matching and phase-matched three-beam HHG are at least feasible. With many of these geometries, the key limitation for studies of the phase-matching has been the required interaction densities. At the needed pressures, the gas flow from traditional targetry exceeds the capacity of the vacuum pumps. However, 3d-printed targets could extend the achievable interaction pressures through the shape of the target itself. For example, gas confinement could be enhanced using an integrated differential pumping system.

In the future, it is conceivable that 3d-printing will not just stop with the printing of single targets. Instead, entire optical setups might become printable. Experiments that formerly required lengthy set up can be easily and rapidly shared with others. They will be automatically aligned with resolution defined by the accuracy of the printer. The future is quite promising for 3d-printed technologies.

Chapter 5

Mid-Infrared Gas HHG Driven with Laguerre-Gaussian mode and Vector Polarization

5.1 Introduction

Unpolarized light is common in the environment. The sun and other thermal light sources involve light from electrons which have a random distribution of orientations and oscillation phases. These natural sources of lights can be made polarized via preferential scattering and reflection at interfaces. The Rayleigh scattering of sunlight is an example. However, modern human-produced light generated via lasers and

antennae sources have a uniform polarization. Many studies have utilized these beams with uniform polarization because they are what are readily available, rather than what might produce new laser-matter interactions.

Advancements in diffractive optical elements have enabled the creation of optics designed to finely adjust the phase and direction of every part of an incident wavefront. It can be used to take the standard TEM00 gaussian with uniform polarization and transform it to have an arbitrary phase and intensity profile. This technology has already been used to make spiral phase plates which can transform uniform polarization into "vector" polarizations. These are polarization states in which the polarization of the beam points inward, to the center of the beam, at every point ("radial" polarization). Also, the polarization can be made to point and wrap around some central point ("azimuthal" polarization). This polarization ("azimuthal") is depicted in the figure below.

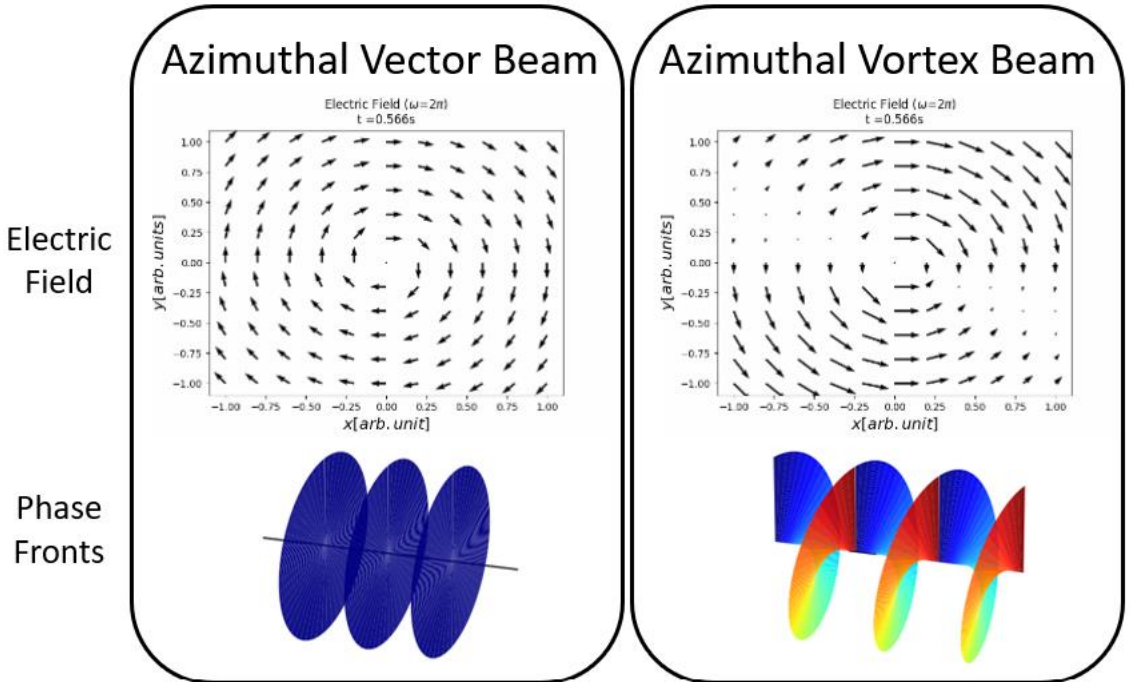

Figure ***50*** Azimuthal polarization states. The lefthand side shows vector polarization. Every point of the beam has the same phase, causing the pattern of intensity to appear uniform. The brightness of this uniform pattern would dim and brighten with a period equal to c_0/λ. The right-hand side shows vortex polarization. The hourglass-shaped intensity pattern would appear to rotate around a central point. The 3d images show the appearance of the phase fronts. For vector polarization, the fronts appear reminiscent of a series of pancakes. For vortex polarization, they appear like a spiral, spaghetti pasta noodle.

These nonstandard polarizations states have many potential applications. They can trap and precisely orient biological cells and microscopic particles[75]. The many polarization orientations and higher order spatial mode structures can increase the bandwidth of light-based communication in fibers[76]. In terms of imaging, it can be used to achieve feature resolutions smaller than the spot size of a diffraction limited focus: $1.22\,\lambda\,f\#$ [77]. Lastly, focused vector polarizations can be implemented to produce smaller etchable feature sizes[78].

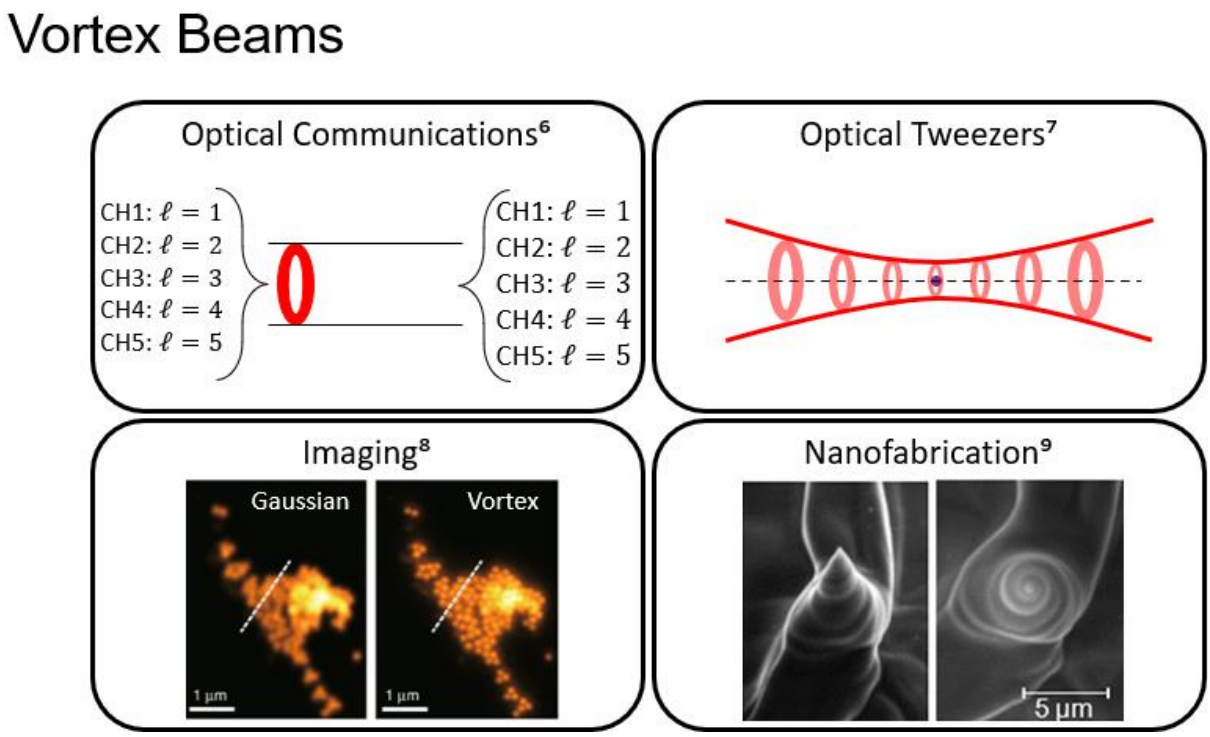

Figure 51 A graphical diagram of the various applications of vortex and vector beams.

This chapter intends to examine how drivers with complex polarization impact the phase-matching of the outgoing gas-harmonics. Terms in the phase-matching equation can relate intimately to the microscopic single atom interactions taking place between the laser and the valence electrons.

5.2 Methods

The experiment was performed on a Ti:Sapphire laser system (Spectra-Physics Solstice ACE). This system can deliver pulses with 7 mJ, 800 nm at a 1 kHz repetition rate and 35 fs pulse duration. For this experiment, measurements of linear-polarized and vector-polarized gas-harmonics were carried out at 1300nm.

The 1300nm light was produced via an optical parametric amplifier (OPA). The OPA was a commercially available "Topas Prime" from Spectra-Physics. 5mJ pulses of

800nm light from the Solstice ACE were directed into the OPA at a repetition rate of 1kHz. This took the input and output of 1mJ of 1300nm light with a pulse duration of about 40fs and a beam diameter of roughly 5mm.

This MIR (mid-infrared) beam was then used as a driver for gas harmonic generation (gas-HHG). The use of any aperture to reduce the beam diameter was explicitly avoided. An aperture is usually employed to improve the mode-matching of the interaction. However, here, it would have changed the desired Laguerre Gaussian and convolved it with a Bessel mode.

To achieve sufficient pressures, a three-stage differentially pumped geometry paired with a gas cell was employed. A schematic of this setup is depicted in Figure 52. The interaction chamber was a 3.5" side-length cube connected to a spectrometer and a forward window via KF40 full-nipple piping. The relatively small internal volume of this setup meant that there was less leak capacity. Compared to the setup utilized in Chapter 4, the internal volume V of the interaction chamber was decreased from about $3339 in^3$ to $0.72 in^3$. Since leak capacity is proportional to V^{α}, the floor pressure decreased proportionally. The floor pressure from the rough vacuum decreased from a few 100s of mTorr to 10s of mTorr.

To drive the interaction at higher pressures, two pinholes were used to strategically choke the flow a few inches and 10s of cm from the target. The first pinhole was a KF40 blank with a 5mm DIA hole drilled in it. The second "pinhole" was a pair of EUV filters. These were slotted into position after pump down and formed a loose seal that isolated the spectrometer from the rest of the system. Altogether, the pinholes increased the achievable target densities from just 100 torr to a few atmospheres.

This was more than enough to phase match 1300 gas harmonics which typically optimizes above 130 Torr.

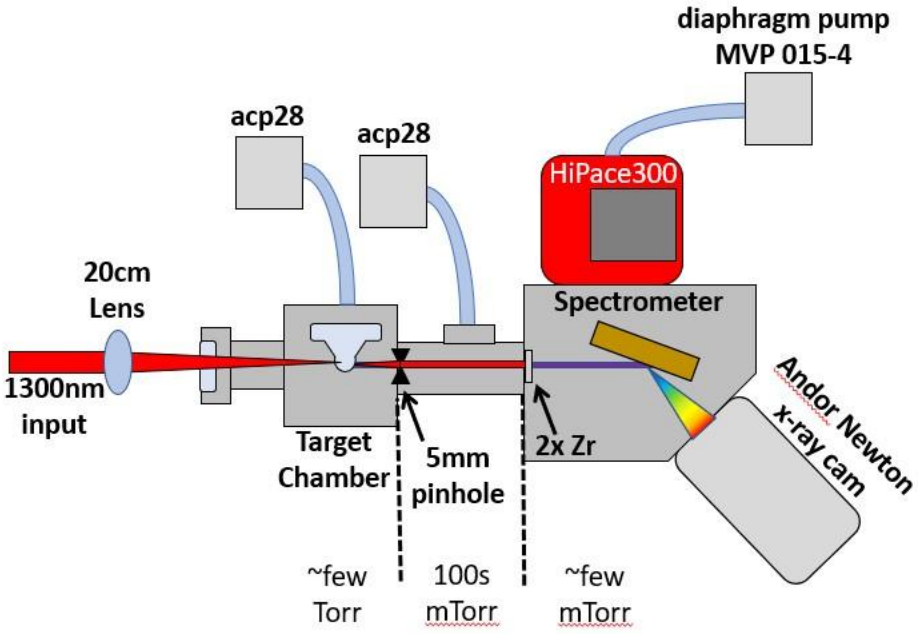

Figure 52 The refined gas harmonic setup. The laser is aligned to pass through two bottlenecks or pinholes which serve to impede the flow of the gas from the target. The dotted lines demarcate the different segments of the system. Each of these regions was observed to equilibrate at different pressures depending on the target backing pressure. Both the interaction chamber and the connective piping before the spectrometer were backed by acp28 roughing pumps. The spectrometer was pumped via a hipace 300.

The silicon-based chips commonly used to align and characterize the input beam were not sensitive for wavelengths at-and-near 1300nm. Alignment was carried out using a commercially available infrared viewer and infrared sensitive cards. The two pinholes paired with the orifices of the target defined the alignment of the system. The placement of the focusing lens and orientation of the spectrometer was intended to keep this beam-path fixed.

The polarization state of the beam was converted using an optic called an s-waveplate (SWP). Through this optic, the beam would be transformed from TEM00 Gaussian into either radial or azimuthal Laguerre Gaussian mode. The mode of the beam at focus was verified by frequency doubling the 1300 light into optical 650nm. This optical light was isolated from the 1300 using a low pass filter.

The appearance of the beam profile at focus was as expected. With no SWP, the beam focus had a linearly polarized gaussian intensity profile. After introduction of the SWP, the focal beam profile was dark in the middle with two bright clover shaped lobes on either side. These two clover-shaped lobes would rotate along with the orientation of the SHG crystal.

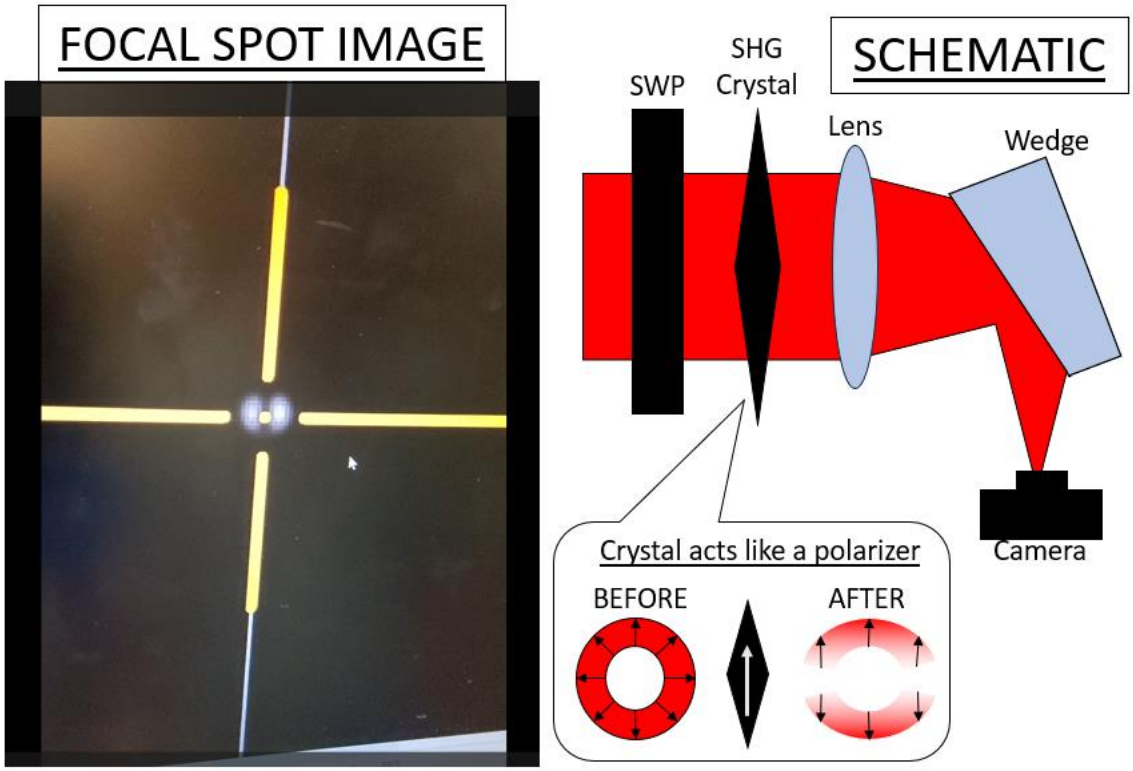

Figure 53 RIGHT Schematic of the setup for observing the focal beam profile of vector-polarized MIR. The action of the SHG crystal was like that of a linear polarizer. LEFT A raw

image of the CCD display feed. The double-lobed structure of the beam would rotate in tandem with the rotation of the nonlinear crystal.

The EUV spectrometer employed a 1200 line/mm grating manufactured by Hitachi. It was set to measure energies from 50 to 150eV. The signal diffracted off the grating acquired using an Andor-Newton x-ray CCD. This signal on the chip was fully binned in the vertical dimension.

5.3 Results

5.3.1 Baseline Measurements of 1300 and 800 Gas Harmonics

Pre-experiment characterization of the 1300nm observed The spatiotemporal properties comparable to the quality of the original 800nm. The focus of the 1300nm tended was bigger, but still diffraction limited. The pulse duration was longer, about 40fs. This was partly due to the finite phase-matching bandwidth of the nonlinear crystals in the "Topas Prime". The near field profile right out of the box was mostly homogeneous but with some scattered hots spots of 1mm or less DIA. This was due to the parametric amplification process having an efficiency related to beam intensity. Otherwise imperceptible noise and spikiness contained in the $800nm$ gets preferentially amplified in the nonlinear processes of the OPA. Subjectively, the near field of the $1300nm$ resembled a cookie with embedded chocolate chips. The "chocolate chips" apparently contain very little of the total energy. The $1300nm$ energy is unchanged when focused through a pinhole. This suggests that the beam only looks worse "by-eye". These are apparently leftover green and blue photons leftover from the "white light" generation process in the "Topas Prime". By comparison, the beam through the viewer also looks much more gaussian-like. Figure ***54*** is a camera photo

of the "by-eye" 1300nm. The signal saturates the camera too much to see the speckle details though.

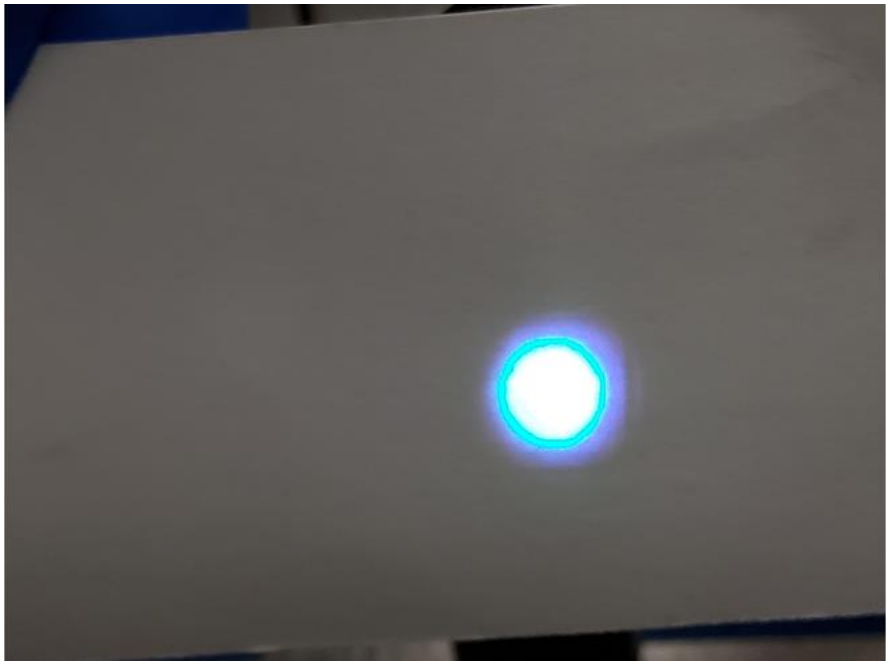

Figure 54 A camera photo of the near field of the 1300nm beam. Like the eye, the silicon chip of a phone camera should also not be able to see the 1300nm. Instead, it is likely seeing leftover "white light" from the "Topas Prime". Unlike a human eye or a scientific camera, the phone camera used here did not have the dynamic range to resolve the mottled-cookie-looking near field described in the paragraph above. Instead, the brightest part of the beam appear to be uniformly saturated. The picture does capture the relative size, color, and shape of the visible parts holdover inside of 1300nm.

The gas-harmonics produced are a secondary confirmation of the 1300nm beam's mode quality. The overall flux and signal quality is intimately tied to the properties of the driver. These measurements are shown in Figure ***55***. The 1300 could be seen to have a higher energy cutoffs which extended to about 72eV. It likely extends even higher, but the signal gets suppressed beyond this point by the known poor transmittivity of aluminum past the 72eV edge.

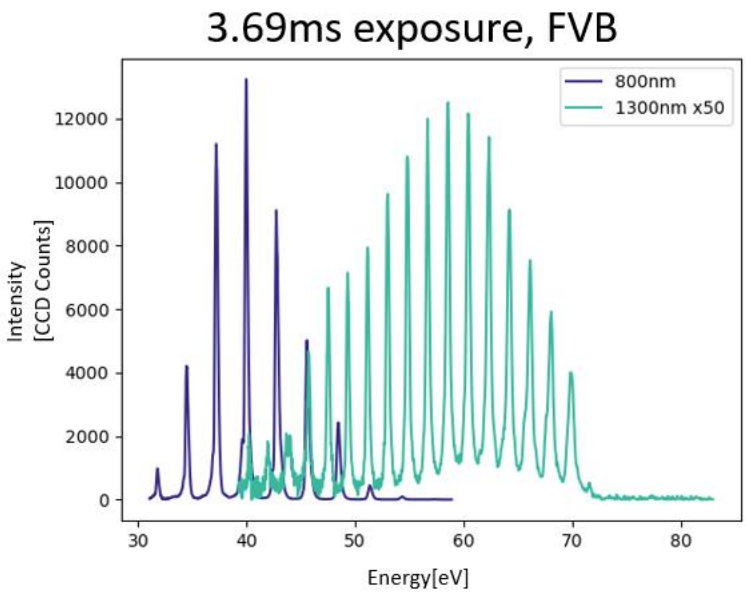

Figure 55 Gas-harmonics driven by 800nm (indigo-color) and 1300nm (teal-seafoam color) beams. These each represent a single shot with minimum exposure time and "FVB" acquisition mode. The signal for the 1300nm was orders of magnitude less than that of the 800nm. The 1300nm signal was multiplied by 50 to make its counts comparable to the 800nm.

5.3.2 Vector Harmonic Observations

he outgoing vector-beam harmonics were observed to have a donut/ring shape reminiscent of the input 1300nm (l=1, p=0) LG vector-beam. Two of these observations are depicted in Figure 56. These measurements bypassed the EUV grating and sent the signal directly onto the Andor-camera. Consistent with the input beam observations, the EUV vector beam was observed to be twice as big and 4x less intense than the linear-polarized Gaussian with same energy. To make the two beams comparable intensity-wise at-focus, the energy of the linearly polarized Gaussian was reduced to 0.37W from 1.07W. This was done by using a beam splitter to reflect most of the energy away, then taking the transmitted beam.

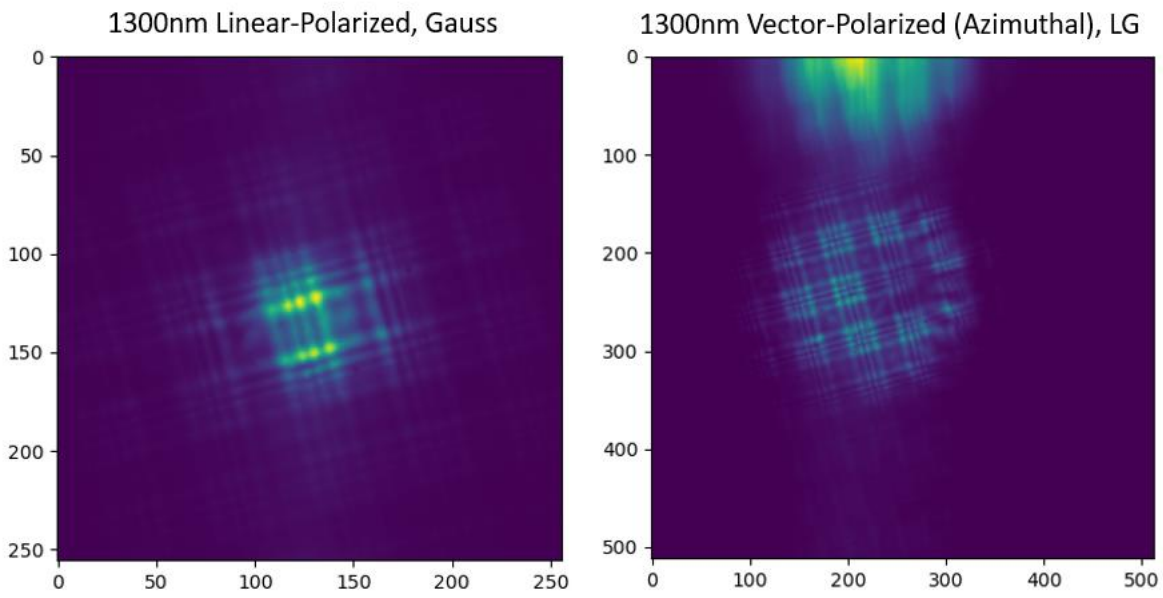

Figure 56 The straight through signal of the optimized EUV. These shots bypassed the diffraction grating. The x and y scales are marked in detectors pixels (each $13um \times 13um$). The colorbar is arbitrary, normalized to the max counts contained in each image. The plaid artifacting is due to transmission through meshed EUV filters. The key takeaway is the appearance of the beam profile. LEFT The linear polarized Gauss. RIGHT The ring/donut shaped vector beam.

The results of the phasematching measurements are depicted in Figure 57. Each horizontal slice represents the photon flux captured at a specific pressure. The pressure varied from 70 to 600 torr. At each step, the pressure was held constant within ± 2.5 torr. The Andor measurements for each of the pressure settings were stacked together to produce a pseudo image. During operation, the ambient pressure inside the interaction chamber could reach pressures as high as a few Torr. This ambient pressure was only about $100mTorr$ after the first pinhole, then only a few $mTorr$ after the second.

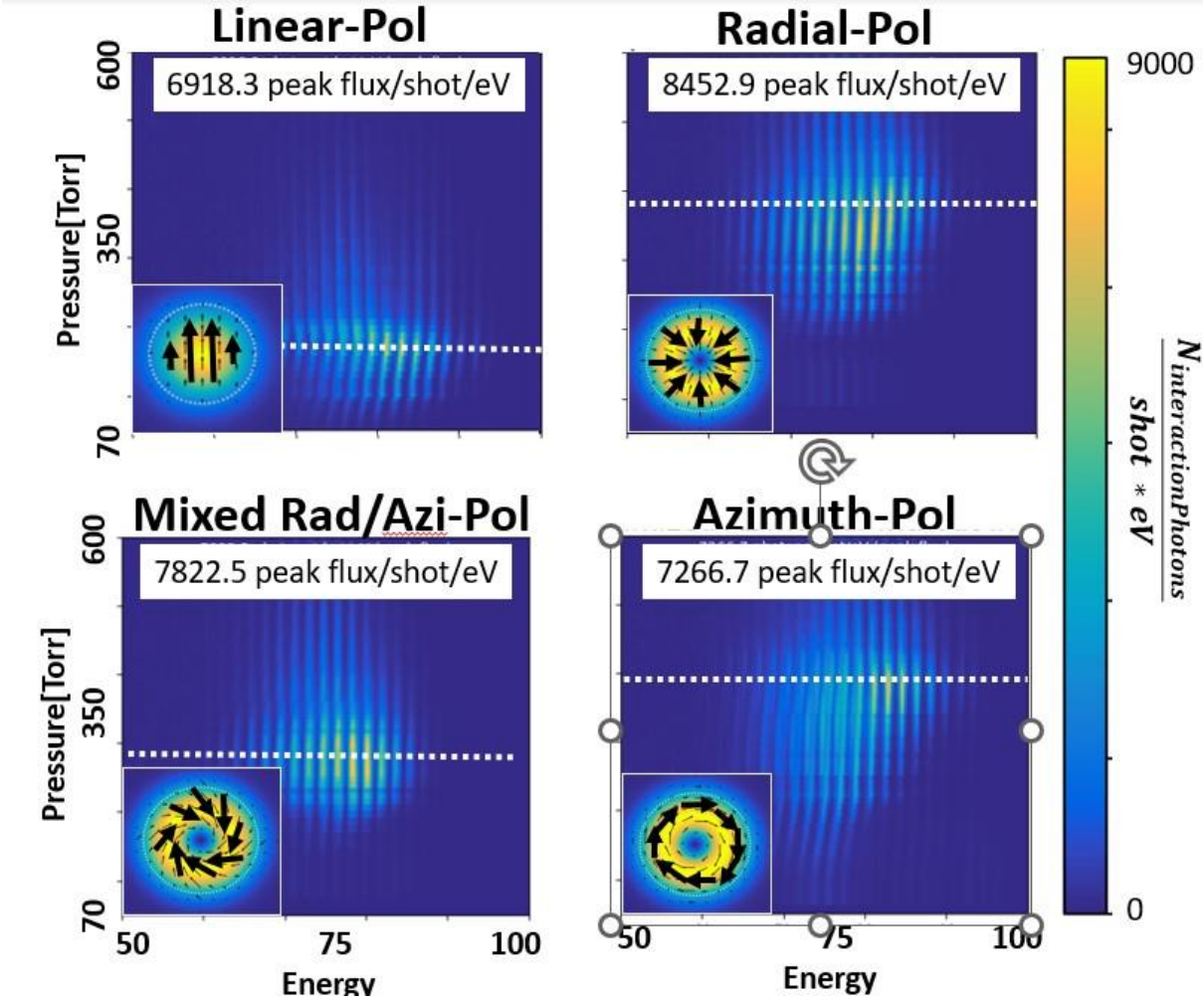

Figure 57 Comparison of the 1300nm Phasematching curves for four different situations. TOP-LEFT represents the control case: Linearly Polarized Gauss. The other three sectors contain various forms of vector-polarization. The photon flux is reported as $photons/(eV \cdot shot)$***. This number was transformed from the raw detector counts using the known efficiency of*** $0.3\mu m$ ***Zirconium as well as the response of the detector. Each horizontal row in the plots represents an image which has been fully binned in the vertical dimension.***

Figure 57 is a representation of the "phase-matching curves" for the different driving modes. The top-left shows linear-polarized Gaussian, while the other sectors show various vector-polarized Laguerre-Gaussian (LG) modes. These plot look like images, but they are not. Many harmonic measurements have been organized together as a

temperature plot whose color represents harmonic flux and xy axes represent harmonic energy and pressure respectively.

5.4 Discussion

5.4.1 1300 versus 800 flux

Compared to 800nm, the flux of the phase-matched 1300 was roughly 50 times less bright. The cause of this flux decrease can be isolated solely to the effect of the longer wavelength in the laser-gas interaction. The comparison measurements were carefully controlled. Both 800 and 1300 had comparable spatiotemporal characteristics. The settings for the spectrometer was kept fixed.

The theoretical basis for the flux decrease is well explained by gas harmonic theory. It is a convolution of both single-atom and many-atom effects summarized graphically in Figure ***58*** This figure graphically summarizes the impact of wavelength on gas harmonic flux. It is the convolution of the single-atom and many-atom effects. The longer wavelengths mean that the single atoms present a smaller target during recombination. The different wavelengths also affect the macroscopic propagation of the beam itself. The negative dispersion contribution from plasma is greater and the positive contribution from neutrals is weaker. This means that it takes even higher backing pressures to phase-match. . One of them is due to the reduced recombination efficiency. Additionally, the longer electron excursion length. The mean free path for a noninteracting gas is given by the expression:

$$\frac{kT}{\sqrt{2}\,\pi\,d^2\,p}$$

(k is the Boltzmann constant. T is the temperature of the gas. d is the atomic diameter. p is the pressure of the gas.) For argon at 300K and 80 Torr, the mean free path is $4.3\mu m$. Semiclassically, the highest energy gas harmonics travel about $\lambda/8$ or $1.3\mu m/8 = 0.1925\mu m$ from the parent atom before the field switches polarity. It is about 200 times smaller than the mean free path. However, statistically, there are billions of potential emitters. Additionally, the angle substended by the parent atom is 1.6 times as small for the highest energies for 1300 versus 800 (assuming $d_{argon} = 140pm$). The electron would not even have to hit another neutral argon atom, ion, or electron head-on. It just needs to enough of a kick or perturbation to miss the parent atom.

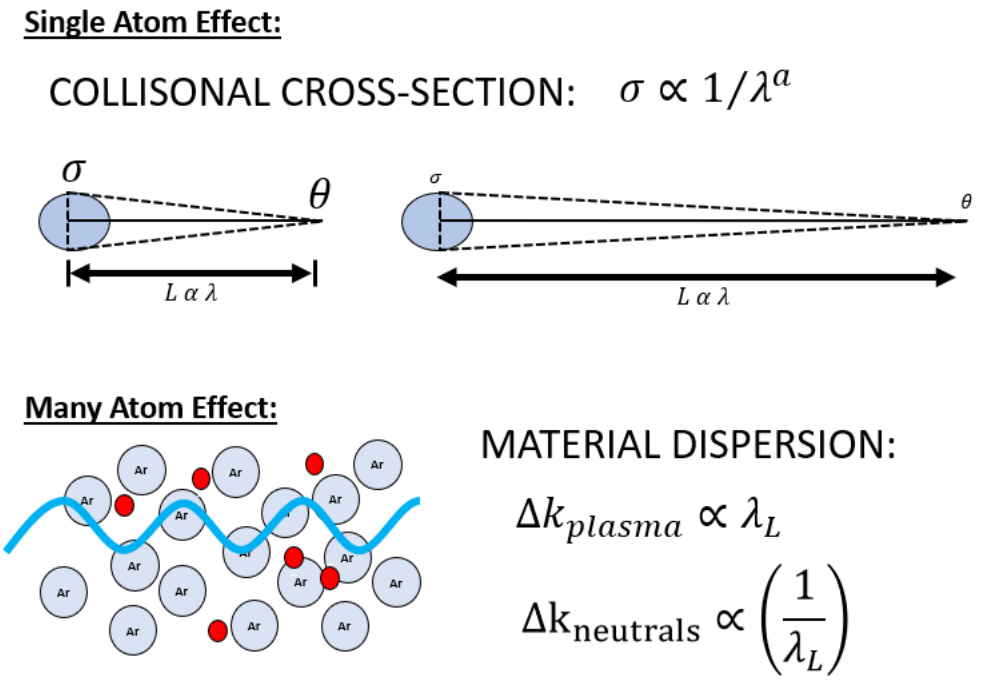

Figure 58 This figure graphically summarizes the impact of wavelength on gas harmonic flux. It is the convolution of the single-atom and many-atom effects. The longer wavelengths mean that the single atoms present a smaller target during recombination. The different wavelengths also affect the macroscopic propagation of the beam itself. The negative dispersion contribution from plasma is greater

and the positive contribution from neutrals is weaker. This means that it takes even higher backing pressures to phase-match.

5.4.2 *Vector Harmonic Phase-matching*

The phase-matching equation for gas harmonic generation can be stated as:

$$\Delta k = \Delta k_{plasma} + \Delta k_{neutrals} + \Delta k_{guoy} + \Delta k_{dipole}$$

The first term Δk_{plasma} is the dispersion due to plasma. It is a function of the intensity and density at focus. The second term $\Delta k_{neutrals}$ is the dispersion due to neutral atoms. It is purely a function of the density at focus. The third term Δk_{guoy} is the dispersion due to focusing and geometric effects. The last term Δk_{dipole} is related to the phase accrued due to the quantum trajectory of the recombining electrons.

In reference [79], the intrinsic phase of quantum paths given is estimated as $\alpha_q^j |U(\boldsymbol{r})|^2$. (Here, $U(\boldsymbol{r})$ represents the energy of the incident field as a function of intensity. α_q^j is a parameter that represents the action due to classical trajectories. The superscript j distinguishes the particular trajectory. The subscript q represents the harmonic order.) Numerical simulations shown in reference [79] demonstrate that the different intrinsic phases of various paths resulted in different optimal macroscopic phasematching parameters. The paper proposes this as a way to way to disentangle the contributions of different quantum paths for HHG driven by OAM-LG drivers.

Based on the data present in Figure 57, we make the argument that the quantum dispersion term Δk_{dipole} has been influenced by modifying the input mode of the driver. Consider just the Guoy term Δk_{guoy} in the phasematching equation, it should be identical for each of the situations presented in the data. The focusing f#, the on-

target intensity, and the z-position relative to the target are identical for all cases. The only parameter that is scanned is pressure. Compared to the Gaussian control, the vector-beams all focused at higher pressures and over a broader range of pressures. The azimuthal and radial cases could be seen to be quite comparable, whereas the mixed polarization (Radial/Azimuthal Combination) seemed to optimize at an intermediate pressure between Gaussian and pure vector. Additionally, even though the Gaussian reference was slightly more intense, the EUV flux of the vector beams seemed to have a peak flux about 1000 photons or so units higher.

Δk_{plasma} and $\Delta k_{neutrals}$ are under the influence of the experimenter. At a given intensity and pressure, the value of Δk_{plasma} and $\Delta k_{neutrals}$ should be the same regardless of whether the input beam is linear or vector polarized. They should not be a function of the spatial mode. If Δk_{guoy} and Δk_{dipole} were the same for each of the four cases, then the phasematching pressure should be unchanged. However, this is not what is observed. It is possible that the difference in phasematching pressure corresponds purely to the difference in Δk_{guoy} between Gaussian and LG modes. However, this would not explain the difference in phasematching pressure between the pure radial or azimuthal and the mixed polarization. There is indication of some influence on the Δk_{dipole} dispersion. If this were the case, then it suggests that the vector polarization compared to linear or mixed azimuthal/radial affects the quantum phase and trajectories.

5.5 Conclusion

The use of vector polarization has gained increasing interest due to already discovered applications. Vector beams may be a technique to more directly probe the

fundamental theory and understanding of gas harmonic generation. The data suggests that gas harmonics driven by Laguerre-Gaussian vector beams favor different quantum electron trajectories. Future work could examine how this intrinsic phase scales with wavelength. It would be interesting to see if the different intrinsic phases observed for 1300nm gaussian and Laguerre-Gaussian drivers remains consistent for other wavelengths. Furthermore, it would be fascinating if these beams could be used one day to precisely control the quantum motions of electrons.

Chapter 6 400nm Solid Harmonic Generation from High-Contrast Drivers

6.1 Intro

The frontier for observing short events is the attosecond-regime: the timescale upon which electrons ionize [80] and transfer in atomic orbitals. Light with this duration can be generated in laser-plasma interactions with femtosecond-duration drivers [81] [82]. The character of this harmonic radiation is a function of the laser and the target.

Up to this point, laser-gas harmonics have been discussed. This is coherent radiation generated from under dense ionized gas media at low intensities. Laser-solid harmonics on the other hand are typically generated with over dense media with relativistic intensities. The electron plasma density is typically on the order of $Z\,n_{solid}$. (In which Z is the atomic number and n_{solid} is a number density of the target material.) The distinction between under dense/over dense is defined by whether the light can propagate through the media. In an under dense media, it can. In over dense, it cannot. The transition between the two is known as the point of "critical density" given by n_{crit}.

The intensity threshold for observing solid HHG is $I > 10^{14}\, W/cm^2$. Above this intensity, the atomic Coulomb potential is fully suppressed. Bound electron states are no longer possible. The ordered solid-state matter dissolves into a soup of charged particles: nuclei and free electrons. Gas-harmonics are produced from the acceleration and recombination of single electrons, whereas solid-harmonics are generated from the bulk motion of the "electronic soup." Since the electrons are less massive, they are usually what responds quickly enough to be collectively and coherently excited by the laser. The anharmonic collective motion of electrons which can self-interact with the laser is what generates the solid-harmonics.

Harmonic generation from intense laser-solid interactions were first observed with CO_2-based lasers in the 1980s[83]. The expansion of a solid-density interface after initial ionization results in an exponential down ramp[84] (see Figure 59). The scale-length refers to the length L_{scale} over which the density of a medium decreases from n_0 to $(1/e)\, n_0$. It is typically stated in units of λ_0, the wavelength of the driver. The brightest and highest energy harmonics are typically produced when the scale length L_{scale} is sufficiently small (on the order of λ_0)[85] [86] [87]. This is due to difference in the stiffness of the media to either side of the critical density point. As the scale-length gets longer, the stiffness to either side approaches unity.

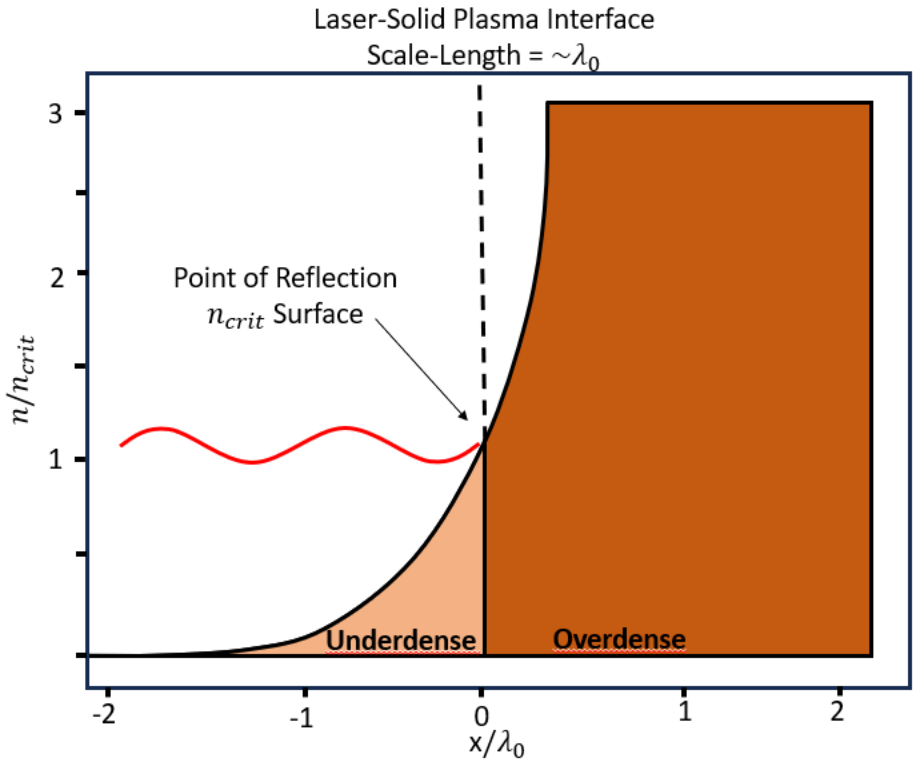

*Figure **59** This is a one-dimensional perspective of a laser-solid interface. The x-axis is in units of $\boldsymbol{\lambda_0}$, the driving wavelength. The y-axis is in units of $\boldsymbol{n_{crit}}$, the critical density. The red squiggly line is intended to represent a beam interacting with a solid-density plasma. The beam is shown propagating through the under dense plasma regions until reaching the critical density surface.*

The scale length of a medium is a function of the temporal contrast of the beam that generated it[88]. Modern lasers which employ femtosecond duration pulses can still contain enough energy "in the wings" to ionize matter well before the main interaction[89]. The expression "in the wings" refers to the parts of a beam which are outside the highest intensity region. Solid High harmonic Generation (Solid HHG) had been carried out with difficulty using femto- duration 800nm driving beams. It is difficult because of non-negligible intensity artifacts that can ionize matter before the highest intensity portions of a beam. These nonneglible artifacts are also called

“prepulse”. Too much “prepulse” impacts the efficiency of harmonics because it can lead to long plasma scale lengths.

However, frequency doubled 400nm can virtually eliminate "prepulse.” This is because the temporal profile of frequency doubled light goes like the original temporal profile squared. See Figure 60. Typically, the pulse duration of a beam is quoted as the either the FWHM or the $1/e^2$. The region outside of the quoted $1/e^2$ are the "wings". It can be observed these the "wings" of a beam can still be quite intense.

Figure 60 presents a hypothetical shape for a laser prepulse. It's been modelled as a perfect gaussian. However, typically, prepulse is not so "well-behaved". Observed prepulse can be jagged and difficult to characterize. It may even have secondary peaks that appear nanoseconds before the "main beam". Even with a perfect gaussian though, the wings of the beam can still be intense enough to ionize matter and form electron plasma. Solid HHG relies on the presence of steep density gradients with which the laser can interact. Ionization before the main beam increases the plasma scale length. It allows time for electron plasma formed nano- or picoseconds before the main interaction to expand out into the vacuum.

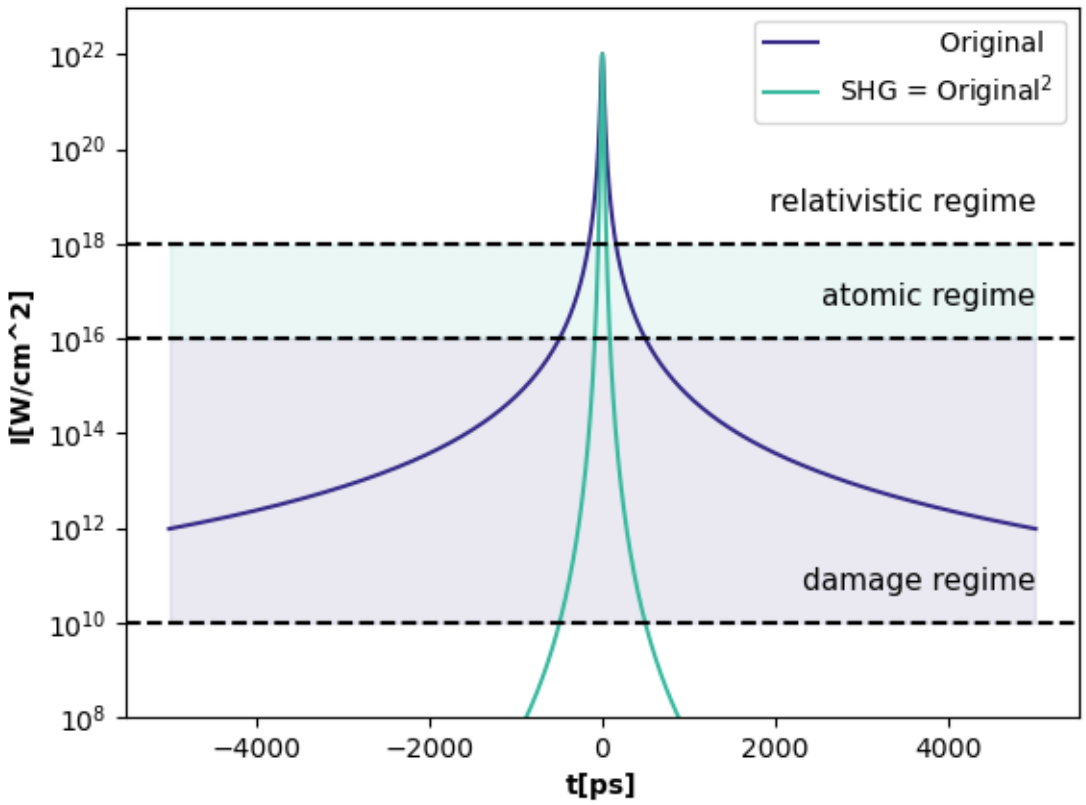

Figure ***60*** This graphic is not actual data or measurement of prepulse. It is generated via analytic equations. Actual prepulse is not typically this well-behaved. The key takeaway is the suppression of the wings. The "original" line shows a temporal profile which can ionize material about a picosecond before the main femtosecond interaction. Whereas, for the frequency doubled profile, the intensity temporal drops off much more quickly. It no longer causes optical damage 1 picosecond before the main interaction.

In this chapter, Solid High-Harmonic-Generation involving two different mechanisms was observed using an ultra-relativistic 400nm driver. The experimental results suggest the two solid harmonic mechanisms are simultaneously present. It can be observed how relevant physics turns on or off physical mechanisms, depending on the details of the interaction and the driving beam. One dimensional (1D) plasma

simulations explore this phenomena further with scans of laser intensity and plasma scale length.

6.2 Methods

The experiment was performed at ALEPH, a Pettawatt-Class Ti:Sapphire laser system located at Colorado State University (CSU). The wavelength accessed was $3-7J$ of 400nm produced from frequency doubled 800nm. The beam was focused to a $1.5um$ spot with an $f = 14in$ parabola at $22.5deg$. The targets were foils of copper with thicknesses of 1 to $15um$.

A diagram of the experimental setup is featured in Figure 61. The entire experiment was conducted in vacuum at sub-Torr pressures. The primary diagnostic was an EUV spectrometer. It was built and characterized at the University of California Irvine. The port leading to the diagnostic pointed in the specular direction from the target. The inside of the diagnostic had a fixed grating geometry.

The grating itself was a gold, nonlinear line-spaced, concave diffraction grating from Hitachi. This allows it to focus on a flat field. The central part of the grating has 1200 grooves per millimeter. The EUV light from a source 1m away impinged on the grating at about a $5deg$ input angle. The light was diffracted onto an Andor-iKon camera with a $0.5in\,x\,0.5in$ chip. The wavelength range on the chip was set to see $15nm$ to $25nm$. The spectral resolution was limited by the $13um$ size of the camera pixels, rather than the imaging.

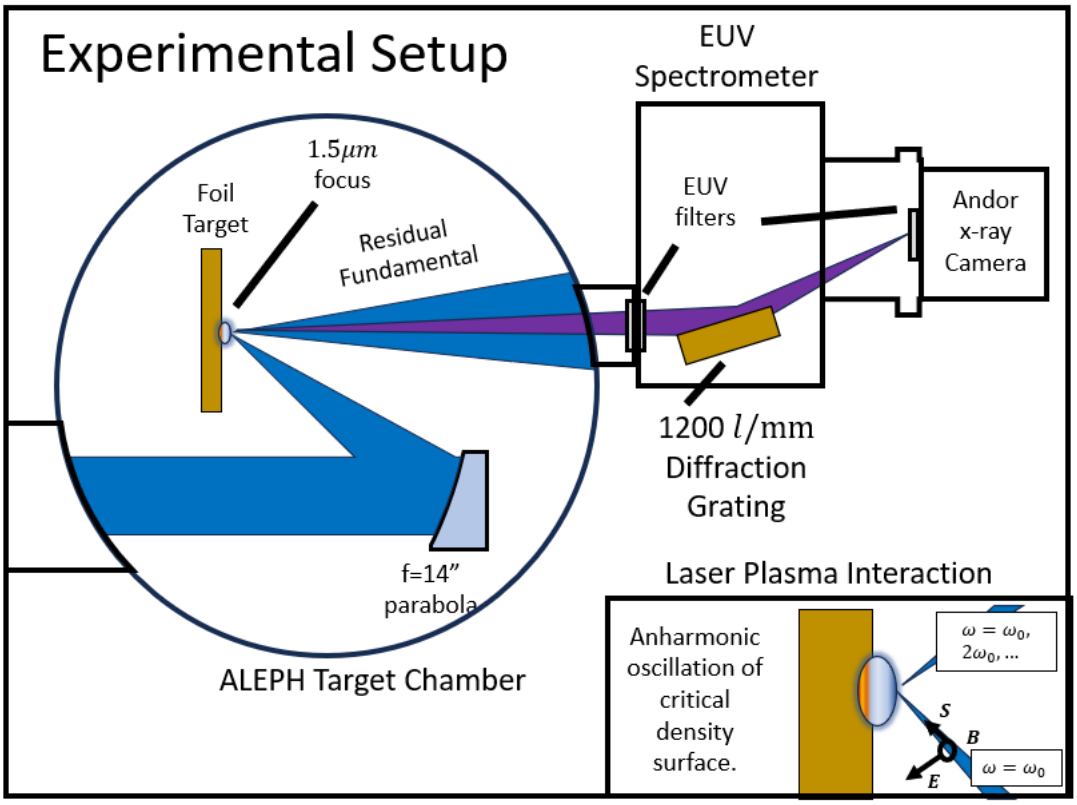

Figure ***61*** The is a schematic of CSU experimental setup. The high-contrast 400nm was delivered into the target chamber from a KF100 port. It is focused with an off-axis parabola onto a solid density target. The beam from this interaction was specularly reflected into a high-resolution spectrometer. The distance from target to grating was about 1m from target to grating.

6.3 Results

A total of a little more than 50 data-shots were taken over about two days of shooting. The waterfall plot shown in the waterfall plot figure is an aggregate image formed from those many shots. The so-called "low energy shots" delivered roughly $3J$ of energy to the target. This corresponds to an on-target intensity of $a_0 = 11$. On the other hand, the so-called "high energy shots" delivered approximately $7J$ and had an on-target intensity of $a_0 = 29$.

In Figure 62, golden arrows mark distinct regularly spaced line-features. For a given energy, these marked line features can be observed to be consistent across each of the many target types. The lower energy shots have just two line-features starting from the lefthand side, whereas the higher energy shots have about six distinct bright lines instead of two. Some shots produced no line features. These can be attributed to misfires which were recorded in the shot logs. The laser had not been properly reset on the target when those shots were taken. This would effectively translate to a much lower on-target intensity (far less than a_0 of 11 or 29).

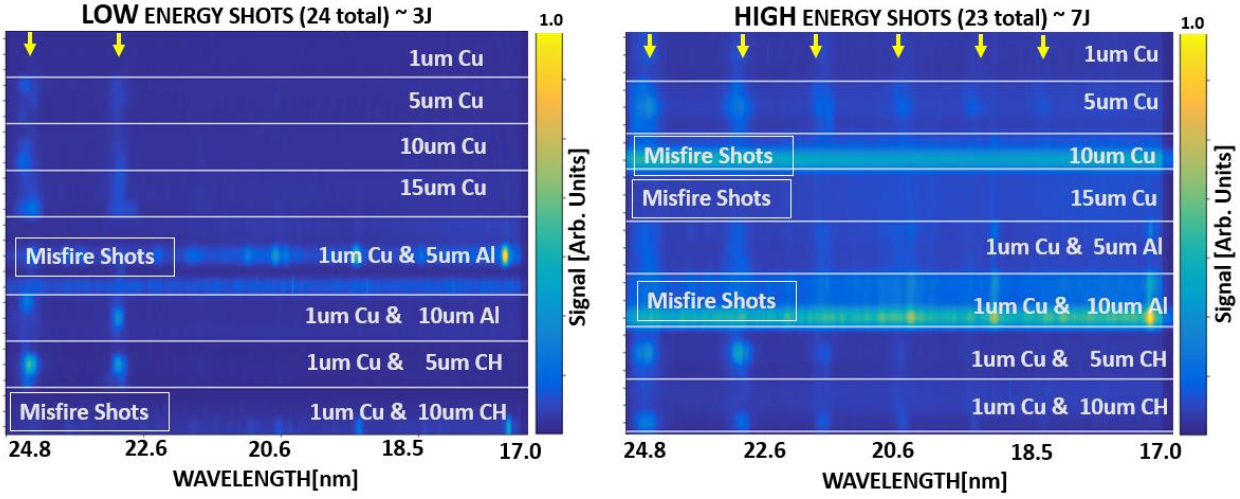

Figure ***62*** These are not images. They are pseudo-images formed by stacking the data from multiple shots together. Each horizontal row of pixels represents a data image that has been one-dimensionalized by binning in the vertical dimension. Rows of pixels have been grouped together by target type. The x-axis represents wavelength. The wavelength gets longer going from right to left. The color map depicts the relative intensity of signal measured at each wavelength position. The units for this color map are in arbitrary units. They have been scaled by the maximum signal in each pseudo-image.

Figure 63 shows two actual data images side-by-side. They are intended to be representative of the trends observed in the waterfall figure. The only difference

between these two shots is the energy. All other parameters are controlled within some margin of error. The target for each of these two shots was 5 micron thick copper foil. The image on the left shows the "low energy" case of 3J. The image on the right shows "high energy" of about 7J. Overlaid on top of each of the images is a lineout formed from binning all the counts in the vertical dimension.

In each image, the distinct line features also observed in Figure 62 are present. These were also seen in the waterfall figure. In the overlaid lineouts, they appear as smooth Gaussian-like peaks. It can be more easily seen here that these lines/peaks occur at integer multiples of the wavelength of the driving laser. This would suggest that the bright lines/peaks are in-fact "high-harmonics". Going from low to high energy, it can be seen that the number of harmonics increases. The two "low energy" harmonics present in both images can be seen to share a similar shape. An overlaid dashed line connecting the two peaks can be seen to have the roughly the same slope. Whereas, a dashed line connecting the higher energy harmonics has a different slope. There would appear to be a "scaling" that is separately obeyed by harmonics with low energy versus high. In the next section, this will be discussed further.

There are other features in the data that will be briefly discussed. The harmonics sit atop a roughly constant background that forms a kind of continuum. This background drops off sharply at 17nm. This is the characteristic wavelength of the aluminum k-edge. It is present because of the two aluminum filters used to filter the fundamental. The continuum light is likely due to thermal electron recombination. In addition to the continuum, there are many sharp lines. Some of these lines are just a pixel in width. These occur at very well-defined wavelengths. In the overlaid lineout, these features appear as jagged sometimes noise-like peaks. These lines are most likely

from ionization and electron energy transitions within the plasma. Both continuum and emission features are typical of plasmas. They tend to be produced well after the initial femtosecond laser-plasma interaction.

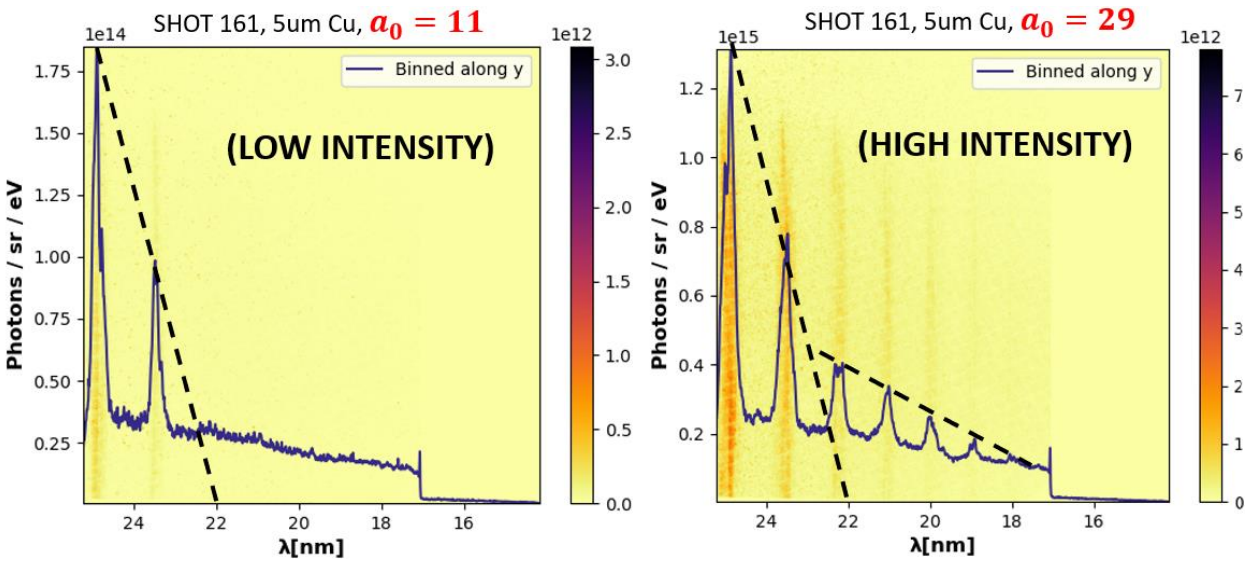

*Figure **63** This figure displays two actual data-images side-by-side. The x-axis represents wavelength in nanometers. The y-axis represent solid-angle in steradians. The spatial extent of the harmonics along the y-axis appears to go beyond the lower edge. Overlaid over each image is a lineout. The color map represents the intensity of the signal at each point on the detector. The raw counts have been converted to* $\boldsymbol{photons/eV \cdot sr}$ *using the known response of the detector. The displayed* $\boldsymbol{photons/eV \cdot sr}$ *also divides out the efficiencies from* $\boldsymbol{0.2\mu m}$ *aluminum filters and the grating.*

6.4 Discussion

There is a natural period of oscillation for electron acoustic waves called the plasma frequency. See equation **Error! Reference source not found.**, the CWE cutoff e quation. Electromagnetic waves can only penetrate and propagate if their frequency is at or above this plasma frequency. As a result, an incident electromagnetic wave typically interacts with the lower density regions at the plasma interface. Here, to

lowest order, the density at the interface can be modelled as an exponential. (See Figure 59).

The laser propagates through the so-called "under dense" regions. The size of this under dense region is a function of the plasma scale length. As the beam propagates through, the density increases until a point of "critical density" is reached. See equation

(6.1) $$n_{crit} = \frac{\epsilon_0 m_e}{e^2} \frac{2 \pi c}{\lambda} \quad (6.1)$$

. This density is a function dependent only on the incident laser wavelength. It is at the critical density surface that the laser is reflected and solid HHG occurs. The interaction of the laser at this critical density surface can excite anharmonic oscillations that produce outgoing harmonics.

$$n_{crit} = \frac{\epsilon_0 m_e}{e^2} \frac{2 \pi c}{\lambda} \quad (6.1)$$

Where n_{crit} is the critical number density. ϵ_0 is the permittivity of free space. m_e is the mass of the electron. e is the fundamental charge constant. λ is the wavelength of the incident electromagnetic wave.

There are two primary mechanisms that drive solid harmonic generation: Coherent Wake Emission (CWE) and Relativistic Oscillating Mirror (ROM)[90, 91, 92, 93, 81]. The mechanism which dominates depends on the value of a_0, the normalized vector potential.

For a_0 less than 1, the laser-plasma interaction is non-relativistic. This is the regime in which CWE dominates. The component of the electric field that points into the plasma oscillates electrons aharmonically at the interface. The oscillation is

anharmonic because of the density difference on either side of the critical density surface. For a sufficiently short plasma scale length, the density on one side of the interface is basically n_{solid} and zero on the other side. On the solid side, the restoring force is much stronger—whereas the opposite is true for the under-dense or vacuum side.

The motion that results can be visualized as being due to a spring that is stiffer moving in one direction than the other. (In other words, it does not obey Hooke's law.) A periodic driving force with frequency ω_0 (the laser) will excite electron motions with many frequencies $\omega = \omega_0, 2\,\omega_0, 3\,\omega_0 \ldots$ For the CWE mechanism, the frequencies are produced up to the plasma frequency. See the cutoff equation. Beyond the plasma frequency, the plasma media cannot respond physically fast enough.

$$\omega_{CWEcutoff} = \omega_{pe} = \sqrt{\frac{n_e e^2}{\epsilon_0 m_e}} \tag{6.2}$$

Where ω_{pe} is the electron plasma frequency, this is the frequency beyond which plasma waves do not propagate. n_e is the electron density in the plasma. e is the fundamental charge. ϵ_0 is the permittivity of free space. m_e is the mass of the electron.

The other solid HHG mechanism is the ROM model. It is relativistic and has a cutoff which directly scales with a quantity called a_0. This quantity is also known as the normalized vector potential. It is determined from the ratio of the laser ponderomotive force $I\lambda^2$ divided by the electron rest mass $m_e\,c^2$. An a_0 of one is typically cited as a threshold for exciting relativistic motions. The cutoff for ROM is represented below:

$$\omega_{ROMcutoff} = \omega_0 4\gamma^2 = \omega_0 4(1 + a_0^2) \quad 6.3$$

Unlike CWE, the ROM mechanism scales quadratically with a_0^2 and, by extension, intensity $I0$. At relativistic intensities, the magnitude of the magnetic field becomes comparable to the electric field. The $\boldsymbol{E} \times \boldsymbol{B}$ force from the laser interacts with the critical density surface. Now, rather than just oscillating individual electrons near the surface, the laser shakes the entire critical density surface directly. As with CWE though, the oscillation will be anharmonic due to the density differential. The interaction of the laser with the rapidly accelerating point of reflection doppler shifts the beam to higher frequencies.

In the previous section, it was observed that the lower and higher energy harmonics obey two different scalings. These trends can be related back to the cutoffs for the different harmonic generation mechanisms: CWE and ROM. As stated in the introduction section, the CWE cutoff is just the plasma frequency and is intensity independent. The plasma frequency ω_p for fully ionized copper can be determined from the density of solid copper n_{copper} and its atomic number Z. Setting $n_p = Z\, n_{copper}$, the plasma frequency and, by extension, CWE cutoff is found to be 22nm.

The value of 22nm for the cutoff would appear to cohere with data. The two "low-energy" harmonics in the shot comparison figure appear to drop off in the vicinity of 22nm. This suggests that they might be related to CWE. Whereas, the higher energy harmonics have a different scaling that doesn't drop off nearly as sharply. The cutoff for ROM is much higher. For the lower on-axis intensity of a0 = 11, the theoretical cutoff is as high as 1nm. Hence, the harmonics present in the "high-intensity" shot with energies higher than 22nm are likely have to be ROM.

From the data, two harmonics from two separate harmonic generation mechanisms can be present simultaneously. Simulations would also seem to agree with the identification of two separate harmonic mechanisms.

Figure ***64*** and Figure ***65*** shows how the target plasma evolves for different starting densities and intensities respectively. It was found that high cutoff harmonics can only be made with incident intensities with a sufficiently short plasma scale length. If the plasma scale length was too long relative to a given laser intensity, it would cause the target to deplete. The nonuniform shape of the depleted interface made it difficult to drive coherent electron motions.

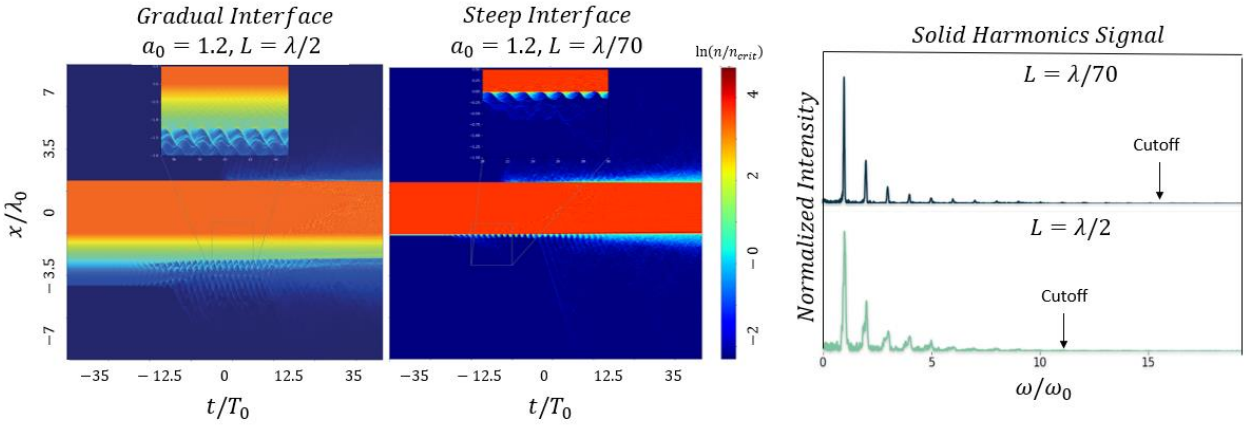

Figure 64 OSIRIS simulations which keep intensity fixed at $a_0 = 1.2$, but compare the effect of two different plasma scale lengths L. The Leftmost plot depicts a scale length of $L = \lambda/2$. The Middle plot depicts a scale length of $L = \lambda/70$. The rightmost plot shows the output harmonic (Simulation Credit [94])

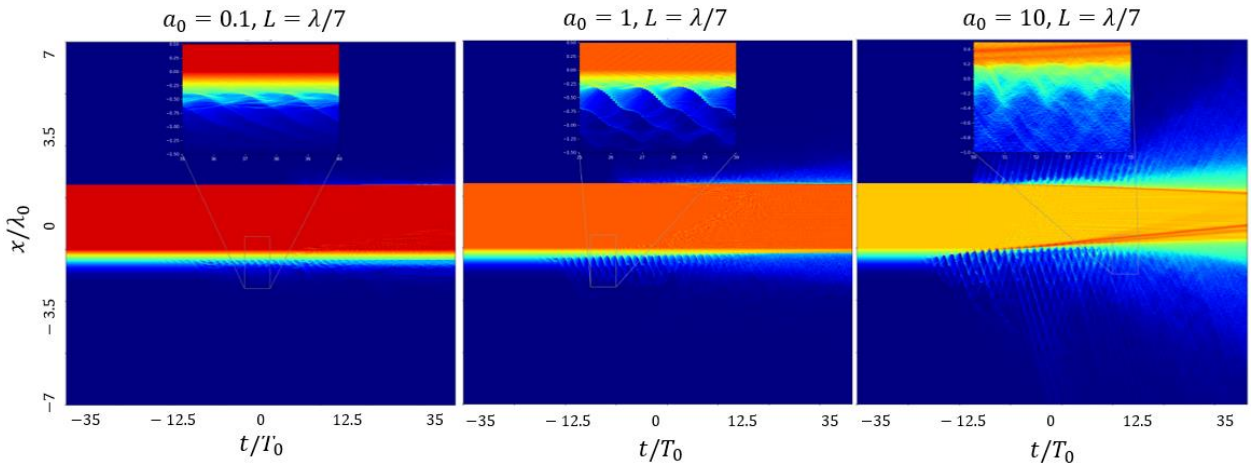

Figure 65 1d Simulations which keep the density fixed while scaling the density. From left to right the peak intensity is increased from $\boldsymbol{a_0 = 0.1}$ to $\boldsymbol{a_0 = 10}$. (Simulation Credit[94])

This simulation is carried out in 1d using an open-source Plasma Particle-in-Cell (PiC) program called Osiris. The laser is incident on a $5\mu m$ slab of material at $22.5deg$ angle of incidence by Lorentz boosting the laser-field into a frame moving parallel to the slab of material and the plane of incidence. This has the effect of eliminating the components of the field parallel to the surface. The simulations would run for 70 periods T of the laser. The outgoing laser beam would be modulated by coherent interactions at the critical density electron surface. The peak intensity and plasma scale length were varied to see how these affected the outgoing harmonic signal.

The simulations suggested that the ROM and CWE harmonics are temporally isolated. They are also produced in different parts of the material. The CWE harmonics are generated before and after the peak intensity of the laser from the lower intensity parts of the beam. The ROM harmonics are produced at and around the peak intensity. In the simulations, harmonics with different cutoffs could be observed by sampling the output radiation at two different separate time windows, one early and

one later. In the experimental data, the two types of harmonics always appear together because of the time-integrated detector.

To summarize, harmonics from two different solid HHG mechanisms were able to be observed simultaneously. They were produced with a high-contrast 400nm beam. Additionally, these are perhaps the brightest measured harmonics produced to date with a 400nm driver. The simulations suggest that the two mechanisms may actually dominate at different times. However, they end up getting convolved together by the time-integrated spectrometer signal. This result perhaps suggests that different spatial and temporal beam profiles can be used to favor one mechanism versus another. Future work could potentially further explore the influence of plasma scale length and laser contrast.

6.5 Conclusion

EUV light from solid-HHG is demonstrated. It was generated with a high contrast 400nm driver with intensities of $(1\,to\,5) \times 10^{21}\ W/cm^2$. Theory has suggested that beams with at least 10^{10} contrast on picosecond timescales would be necessary to resolve both mechanisms at once. The Advanced Laser for Extreme Photonics (ALEPH) has this necessary laser contrast. Comparisons of high and low intensities at the CWE cutoff reveal a kind of "crossover point". EUV spectroscopy data was taken near 22nm. This is the plasma frequency for fully ionized copper. Here, Solid HHG from the two primary physical mechanisms can be observed: The ROM mechanism begins to dominate as the intensity is increased.

In terms of future work, it would be interesting to carry out further simulations in 2d. It is conceivable that there are spatially isolated isolated CWE and ROM mechanisms.

Like how the early and late parts of the beam favored the creation of CWE harmonics. In terms of spatial effects, ROM harmonics might be produced at tightest focus and CWE away from tightest focus.

Chapter 7

Conclusion

Chapter 1 was a look into the past and the fundamental observational principles that undergird the work and art of science itself. Chapters 2 and 3 described the understood theory and experimental techniques required for the results presented.

In Chapter 4, the development of 3D printed gas targetry for HHG was presented. 3d-printed targets were shown to achieve parameters necessary for phase matching. This is shown by both the flux scaling with interaction length and the scaling with pressure. An integrated 29th harmonic flux of 10^7 photons/shot was demonstrated, corresponding to a conversion efficiency of about 10^{-7}. Future modifications of the design of the 3d-printed cells could possibly increase this value. Compared to the traditional targets, the difference is 3 to 4 orders of magnitude. The 3d-printed cells provide a high brightness comparable to the hollow waveguides while preserving the free focus geometry. The proof of concept was the successful detection of 2-beam noncollinear gas-harmonics.

These cells could eventually be adapted to any other laser-gas-target based experiment. With modification, quasi-phase-matching and phase-matched multi-beam HHG are feasible. With many of these geometries, the key limitation for studies of the phase-matching has been the required interaction densities. 3d-printed targets

could extend the achievable interaction pressures through the shape of the target itself.

In the future, it is conceivable that 3d-printing will enable entire optical setups to become printable. Experiments that formerly required lengthy set up can be easily and rapidly shared with others. The gas cells developed are already in use in another research laboratory, where designs were shared and the cells printed locally. They will be automatically aligned with resolution defined by the accuracy of the printer. The future is quite promising for 3d-printed technologies.

In Chapter 5, 3D printed gas targetry was used to measure the phase matching curves of high harmonic generation with vector beams. Vector beams may be a technique to directly probe the fundamental theory and understanding of gas harmonic generation. The results from the phase matching curves suggest that gas harmonics driven by Laguerre-Gaussian vector beams favor different quantum electron trajectories. Future work could examine how this intrinsic phase scales with wavelength. It would be interesting to see if the different intrinsic phases observed for gaussian and Laguerre-Gaussian drivers remains consistent for various wavelengths. Furthermore, it would be fascinating if these beams could be used one day to precisely control the quantum motions of electrons.

In Chapter 6, results from relativistic high harmonic generation with 400 nm wavelengths were shown. EUV light was measured from a high contrast 400nm driver with intensities of (1 to 5) $\times 10^{21}$ W/cm^2 interacting with solid density foils. Prior work has suggested that beams with at least 10^{-10} laser contrast on picosecond timescales would be necessary; the Advanced Laser for Extreme Photonics (ALEPH) has this necessary laser contrast. Comparisons of high and low intensities at the CWE

cutoff reveal a kind of "crossover point". EUV spectroscopy data was taken near 22nm, which is the plasma frequency for fully ionized copper. Solid HHG from the two primary physical mechanisms can be observed: CWE at lower intensities, while the ROM mechanism begins to dominate as the intensity is increased.

In terms of future work, further simulations could be performed in 2d. It is conceivable that there are spatially isolated CWE and ROM mechanisms. For instance, the early and late parts of the beam favored the creation of CWE harmonics. In terms of spatial effects, ROM harmonics might be produced at tightest focus and CWE away from tightest focus.

The energy of some state n in the Bohr atom is given by the Rydberg equation, $E(n) = h\,c\,R_H(1/n^2)$. When electron transitions from one state to another, its probability density oscillates from with a period $T = h/[E(n_1) - E(n_2)]$. For an inner shell transition from $n_1 = 1$ to $n_2 = 2$, the characteristic timescale T of motion would be about $405as$. As shown in Figure 21 and Figure 23, the FTL of the gas harmonic spectra indicates that the pulse duration of each EUV burst is on the order of hundreds of as.

The discovery of gas harmonic generation and isolated attosecond pulse was just awarded the Nobel prize in Physics (2023). An exciting application and future use of this radiation will be that of pump-probe spectroscopy. This light source would be able to directly test quantum models of atoms and molecules. Example systems of interest include:

- **Nanoplasmonics**: Collective free electron motions can be excited in nanowires by electromagnetic fields. The rise time of these collective motions are on the order of attoseconds.

- **Real time Molecular imaging**: A sufficiently intense pump pulse incident on a molecule can drive a "coulomb explosion" (CE) in which an atom's binding field becomes repulsive. This causes the atom to dissociate into two or more parts. An attosecond probe beam observes this dissociation in real time.
- **Electron correlations**: The Schrodinger equation for atoms with many electrons can be very difficult to solve. Electrons contained in such atoms can be correlated and share energy with one another. For example, the transition of one electron may excite motions in another electron. Attosecond probes can isolate these secondary electrons motion by observing in transitive states before these motions can take place.

The current obstacle is the brightness of these attosecond beams. The conversion efficiency tends to be poor with harmonic energies at least 10^{-6} times less than the driver. However, with continuing advancements in the understanding of phase matching (Chapters 4 and 5), this limitation may eventually be overcome. Additionally, Solid Harmonic Generation which does not rely on the recombination of electrons with bound states can be driven at the highest energies possible. The resulting EUV light comes out automatically phase-matched. The key limiter for solid-harmonics has been access to high-energy and contrast driving beams. The work in Chapter 6, however, is a promising step in the right direction. With access to attosecond light sources very close, there may be a coming revolution in the understanding of physics comparable to the one which occurred one hundred years ago when quantum mechanics was first formalized.

Bibliography

1. N. Bostrom, Journal of medical ethics **31** (5), 273-277 (2005).
2. N. Goodman, presented at the Uniformity and simplicity: A symposium on the principle of the uniformity of nature, 1967 (unpublished).
3. E. Meijering, Proceedings of the IEEE **90** (3), 319-342 (2002).
4. O. Velychko and T. Gordiyenko, in *Standards, Methods and Solutions of Metrology* (IntechOpen, 2019).
5. G. T. Smith, *Machine tool metrology: An industrial handbook*. (Springer, 2016).
6. G. Girard, Metrologia **31** (4), 317 (1994).
7. P. G. Roll, R. Krotkov and R. H. Dicke, Annals of Physics **26** (3), 442-517 (1964).
8. K. Kötter, C. Aulbert, S. Babak, R. Balasubramanian, S. Berukoff, S. Bose, D. Churches, C. N. Colacino, C. Cutler and K. Danzmann, Classical and Quantum Gravity **19** (7), 1399 (2002).
9. J. M. Jenkins, D. A. Caldwell, H. Chandrasekaran, J. D. Twicken, S. T. Bryson, E. V. Quintana, B. D. Clarke, J. Li, C. Allen and P. Tenenbaum, The Astrophysical Journal Letters **713** (2), L120 (2010).
10. I. M. Mills, P. J. Mohr, T. J. Quinn, B. N. Taylor and E. R. Williams, Metrologia **42** (2), 71 (2005).
11. P. François, F. Matteucci, R. Cayrel, M. Spite, F. Spite and C. Chiappini, Astronomy & Astrophysics **421** (2), 613-621 (2004).
12. N. Prantzos, in *Lectures in Astrobiology: Volume II* (Springer, 2007), pp. 1-43.
13. R. A. Alpher, American Scientist **61** (1), 52-58 (1973).
14. J.-P. Uzan, Comptes Rendus Physique **16** (5), 576-585 (2015).
15. J. Perina, *Coherence of light*. (Springer Science & Business Media, 1985).
16. M. F. Land and R. D. Fernald, Annual review of neuroscience **15** (1), 1-29 (1992).
17. O. Von Spaeth, Centaurus **42** (3), 159-179 (2000).
18. I. Nechytailo, O. Kovaliuk and O. Gorodyska, (2022).
19. N. Arikha, *Passions and tempers: A history of the humours*. (Noga Arikha, 2007).
20. I. P. Howard, *Perceiving in depth, volume 1: basic mechanisms*. (Oxford University Press, 2012).
21. A. M. Smith, Archive for history of exact sciences, 221-240 (1982).
22. J. Al-Khalili, (Nature Publishing Group UK London, 2015).
23. T. E. Huff, *Intellectual curiosity and the scientific revolution: a global perspective*. (Cambridge University Press, 2010).
24. I. Newton, *The Optical Papers of Isaac Newton: Volume 1, The Optical Lectures 1670-1672*. (Cambridge University Press, 1984).
25. A. Van Helden, Journal for the History of Astronomy **14** (2), 137-141 (1983).
26. H. Crew, JOSA **20** (1), 3-10 (1930).
27. S. D'Agostino, Centaurus **29** (3), 178-204 (1986).
28. J. C. Maxwell, *A dynamical theory of the electromagnetic field*. (Wipf and Stock Publishers, 1996).

29. L. Bragg and H. Lipson, Journal of Scientific Instruments **20** (7), 110 (1943).
30. M. W. Jackson, *Spectrum of belief: Joseph von Fraunhofer and the craft of precision optics*. (Mit Press, 2000).
31. J. P. McEvoy and O. Zarate, *Introducing quantum theory: A graphic guide*. (Icon Books Ltd, 2014).
32. H. Kragh, *Niels Bohr and the quantum atom: The Bohr model of atomic structure 1913-1925*. (OUP Oxford, 2012).
33. C. Davisson, Science **71** (1852), 651-654 (1930).
34. D. L. Aronstein and C. Stroud, Physical Review A **55** (6), 4526 (1997).
35. in *Chemistry LibreTexts* (July 17, 2020).
36. J. F. Ogilvie, arXiv preprint arXiv:1709.04759 (2017).
37. S. A. Holgate, *Understanding solid state physics*. (cRc Press, 2021).
38. A. Castleman and K. Bowen, The Journal of Physical Chemistry **100** (31), 12911-12944 (1996).
39. M. H. Penner, Food analysis, 79-88 (2017).
40. M. Fushitani, Annual Reports Section" C"(Physical Chemistry) **104**, 272-297 (2008).
41. H. R. Griem, *Principles of plasma spectroscopy*. (2005).
42. M. C. Potter, B. Wyble, C. E. Hagmann and E. S. McCourt, Attention, Perception, & Psychophysics **76**, 270-279 (2014).
43. M. Jogan and A. A. Stocker, Journal of Neuroscience **35** (25), 9381-9390 (2015).
44. F. Abbas, F. Vinberg and S. Becker, JoVE (Journal of Visualized Experiments) (184), e62763 (2022).
45. K. Lieto, R. Skopek, A. Lewicka, M. Stelmasiak, E. Klimaszewska, A. Zelent, Ł. Szymański and S. Lewicki, International Journal of Molecular Sciences **23** (16), 9158 (2022).
46. E. Muybridge, *Animal locomotion*. (Da Capo Press Cambridge, MA, 1887).
47. A. Daigle, Film History **29** (4), 112-130 (2017).
48. E. Muybridge, (Time Magazine, Photographs reproduced in Time's "100 Most Influential Images", 1878), Vol. 2019.
49. P. Papacosta, International Journal of Art and Art History **6** (1), 15-26 (2018).
50. B. Chisholm, (2016).
51. C. Smith, (Digital Photography School), Vol. 2019.
52. (Chicago Architecture Center).
53. H. D. Edgerton, in *The Edgerton Digital Collections (EDC) Project* (MIT Libraries and Institute Archive, 1964), Vol. 2023.
54. P. B. Corkum, Physical review letters **71** (13), 1994 (1993).
55. A. Rundquist, C. G. Durfee III, Z. Chang, C. Herne, S. Backus, M. M. Murnane and H. C. Kapteyn, Science **280** (5368), 1412-1415 (1998).
56. C. G. Durfee III, A. R. Rundquist, S. Backus, C. Herne, M. M. Murnane and H. C. Kapteyn, Physical Review Letters **83** (11), 2187 (1999).
57. R. Paschotta, in *RP Photonics Encyclopedia*.
58. A. L. Lytle, University of Colorado at Boulder, 2008.
59. M. Ferray, A. L'Huillier, X. Li, L. Lompre, G. Mainfray and C. Manus, Journal of Physics B: Atomic, Molecular and Optical Physics **21** (3), L31 (1988).
60. E. W. Weisstein, From MathWorldA Wolfram Web Resource (2011).

61. S. Tzortzakis, L. Bergé, A. Couairon, M. Franco, B. Prade and A. Mysyrowicz, Physical review letters **86** (24), 5470 (2001).
62. R. I. Miller and T. G. Roberts, Applied optics **26** (21), 4570-4575 (1987).
63. B. L. Henke, E. M. Gullikson and J. C. Davis, Atomic data and nuclear data tables **54** (2), 181-342 (1993).
64. J. H. Underwood, E. M. Gullikson, M. Koike and S. Mrowka, presented at the Gratings and Grating Monochromators for Synchrotron Radiation, 1997 (unpublished).
65. B. Blagojević, E.-O. Le Bigot, K. Fahy, A. Aguilar, K. Makonyi, E. Takács, J. Tan, J. Pomeroy, J. Burnett and J. Gillaspy, Review of scientific instruments **76** (8) (2005).
66. J. Rothhardt, M. Krebs, S. Hädrich, S. Demmler, J. Limpert and A. Tünnermann, New Journal of Physics **16** (3), 033022 (2014).
67. F. Lindner, W. Stremme, M. G. Schätzel, F. Grasbon, G. G. Paulus, H. Walther, R. Hartmann and L. Strüder, Physical Review A **68** (1), 013814 (2003).
68. C. Heyl, J. Güdde, A. L'Huillier and U. Höfer, Journal of Physics B: Atomic, Molecular and Optical Physics **45** (7), 074020 (2012).
69. M. Zepf, B. Dromey, M. Landreman, P. Foster and S. Hooker, Physical review letters **99** (14), 143901 (2007).
70. .
71. I. Ramlan and N. Darlis, Journal of Design for Sustainable and Environment **2** (2) (2020).
72. E. Bellos, Z. Said and C. Tzivanidis, Journal of Cleaner Production **196**, 84-99 (2018).
73. G. D. Buyalich, K. Buyalich and V. Voyevodin, presented at the IOP Conference Series: Materials Science and Engineering, 2015 (unpublished).
74. J. Bertrand, H. J. Wörner, H.-C. Bandulet, E. Bisson, M. Spanner, J.-C. Kieffer, D. Villeneuve and P. B. Corkum, Physical review letters **106** (2), 023001 (2011).
75. Y. Shen, X. Wang, Z. Xie, C. Min, X. Fu, Q. Liu, M. Gong and X. Yuan, Light: Science & Applications **8** (1), 90 (2019).
76. A. E. Willner, H. Huang, Y. Yan, Y. Ren, N. Ahmed, G. Xie, C. Bao, L. Li, Y. Cao and Z. Zhao, Advances in optics and photonics **7** (1), 66-106 (2015).
77. L. Li and F. Li, Physical Review E **88** (3), 033205 (2013).
78. S. Li and Z. Wang, Applied Physics Letters **103** (14) (2013).
79. C. Hernandez-Garcia, L. Rego, J. San Román, A. Picón and L. Plaja, High Power Laser Science and Engineering **5**, e3 (2017).
80. P. Corkum, presented at the Conference on Lasers and Electro-Optics, 2007 (unpublished).
81. C. Thaury and F. Quéré, Journal of Physics B: Atomic, Molecular and Optical Physics **43** (21), 213001 (2010).
82. T. Hammond, G. G. Brown, K. T. Kim, D. Villeneuve and P. Corkum, Nature Photonics **10** (3), 171-175 (2016).
83. N. Burnett, H. Baldis, M. Richardson and G. Enright, Applied Physics Letters **31** (3), 172-174 (1977).
84. P. Mora, Physical Review Letters **90** (18), 185002 (2003).
85. F. Dollar, P. Cummings, V. Chvykov, L. Willingale, M. Vargas, V. Yanovsky, C. Zulick, A. Maksimchuk, A. Thomas and K. Krushelnick, Physical Review Letters **110** (17), 175002 (2013).

86. C. Rödel, D. an der Brügge, J. Bierbach, M. Yeung, T. Hahn, B. Dromey, S. Herzer, S. Fuchs, A. G. Pour and E. Eckner, Physical review letters **109** (12), 125002 (2012).
87. S. Kahaly, S. Monchocé, H. Vincenti, T. Dzelzainis, B. Dromey, M. Zepf, P. Martin and F. Quéré, Physical review letters **110** (17), 175001 (2013).
88. A. Mackinnon, M. Borghesi, S. Hatchett, M. Key, P. Patel, H. Campbell, A. Schiavi, R. Snavely, S. Wilks and O. Willi, Physical Review Letters **86** (9), 1769 (2001).
89. K. Osvay, M. Csatári, I. Ross, A. Persson and C.-G. Wahlström, Laser and Particle Beams **23** (3), 327-332 (2005).
90. F. Quéré, C. Thaury, P. Monot, S. Dobosz, P. Martin, J.-P. Geindre and P. Audebert, Physical review letters **96** (12), 125004 (2006).
91. S. V. Bulanov, N. Naumova and F. Pegoraro, Physics of Plasmas **1** (3), 745-757 (1994).
92. R. Lichters, J. Meyer-ter-Vehn and A. Pukhov, Physics of Plasmas **3** (9), 3425-3437 (1996).
93. T. Baeva, S. Gordienko and A. Pukhov, Physical review E **74** (4), 046404 (2006).
94. V. Flores, in *OSIRIS* (Graduate Research Assistant, Ph.D Student, Shared Research Group SLACK channel, 2023), pp. 1D OSIRIS plasma simulation results. These were studies that intended to investigate the relationship between solid harmonic output and various starting parameters.